

Title

**Microbubble distribution and incorporation in an ex-vivo perfused porcine
liver model**

Thesis submitted for the degree of

Doctor of Medicine

at the University of Leicester

by

Mr Ahmed Alzaraa

Department of Cancer Studies and Molecular Medicine

University of Leicester

Declaration:

I declare that I have done all the work in this project and written the thesis myself. Any contribution from others has been mentioned in in the acknowledgement section. This thesis has not been submitted to any other university or institution for another degree. All the parts of this project that have been published or submitted for publication have been mentioned at the end of the thesis.

Preface:

This thesis describes the behaviour and distribution of microbubbles using ultrasound and the relevant histological changes that occur upon the application of microwave energy in an ex-vivo perfused porcine liver model.

The research was conducted in the laboratories of the Department of Molecular Medicine and Transplant Biology at Leicester General Hospital. The department has a long-standing interest in bio-artificial liver and basic investigation of tissue ablation techniques. To do this, the department runs an ex-vivo porcine liver model and has considerable experience in this field. This model is perfused with autologous blood. It accurately simulates the in-vivo situation, but removes some of the extraneous and confounding components associated with normal physiological and metabolic responses. This allows for extremely careful and reproducible adjustments of inflow and outflow parameters and is ideal for basic investigation of blood flow, and anything affected by this including substances infused into the liver.

Acknowledgement:

“It always seems impossible until it is done” -Nelson Mandela (1918-2013)

The formidable challenges I faced at the inception of this work made it all seem almost impossible even when it was almost done. First I was a novice to benchwork and had no skills in veterinary surgery or ultrasonography (US). I then needed to have a reliable, validated animal model that could answer the research question and help secure a Home Office Licence to do the work with the minimum number of animals. Then there were the usual funding issues and deadlines.

This work was therefore only possible because a large number of individuals, too many to mention, contributed in various ways. To them I owe a huge debt of thanks. Foremost I wish to thank my supervisors Prof. David Lloyd, Prof. Kevin West and Prof. Bruno Morgan for their invaluable support and guidance throughout. In addition, Prof. Morgan even contributed funds when I needed them.

For training me to do porcine liver dissection within the 15-20 minutes stipulated by protocol, I am grateful to Dr Wen Chung, a scientist in the laboratory as well as my team of research fellows. After attending an ultrasound basic skills course at Ipswich Hospital, I still relied on the superior skills and experience of some radiographers at Leicester General Hospital who patiently taught me how to work the machine and the settings for microbubble scanning. To them I am grateful. I thank Dr Keith Dunn of Queen’s Medical Centre, Nottingham who helped with reporting the radiological images and a representative from Braco Ltd the manufacturers of the microbubble I used for setting up the machine to the required mechanical index to visualise MBs.

Not least of all, at the end of the work, my surgical trainer Mr Kassim Zayyan, consultant surgeon at George Eliot Hospital critically read and extensively edited the draft thesis, helping to put it in its current form. To him I am very grateful.

Table of Contents

TITLE	1
MICROBUBBLE DISTRIBUTION AND INCORPORATION IN AN EX-VIVO PERFUSED PORCINE LIVER MODEL	1
DECLARATION:	2
PREFACE:	3
ACKNOWLEDGEMENT:	4
ABSTRACT	9
INTRODUCTION.....	11
Basics of Ultrasound:.....	13
US Imaging:	15
Image Enhancement Principles and Techniques:	16
Microwave ablation in clinical practice:	18
Understanding microwave physics.....	18
Ablative techniques for treating hepatic tumours:	23
Characterisation of liver tumours using CEUS:	24
Contrast-enhanced ultrasound in the preoperative, intraoperative and postoperative assessment of liver lesions:	25
Contrast agents for the study of liver lesions:	25
Types of microbubbles used in the assessment of liver lesion:	34
Contrast-enhanced intraoperative ultrasound during percutaneous radiofrequency ablation:	37
CHAPTER ONE.....	40
MBs and US Image Enhancement.....	40
Methods of producing microbubbles:.....	43
Generations of microbubbles:	44
Microbubble behaviour in US:.....	45
Mechanical index:	48
Microbubbles' response relative to mechanical index:	49
Image Enhancement:	50

Quantitative versus targeted imaging:	51
Utility of MBs in CEUS:	51
Current and potential clinical applications:	52
Biophysical effects of microbubbles:	56
Microbubble safety:	58
Diagnostic applications of MBs:	59
Therapeutic applications of MBs:	59
CHAPTER TWO	72
Contrast-enhanced ultrasound detects perfusion defects in an ex vivo porcine liver model: a useful tool for the study of hepatic reperfusion	72
Abstract:	72
Introduction:	72
Materials and methods:	77
<i>Ultrasound scanning:</i>	82
<i>Histological examination:</i>	84
<i>Statistical analysis:</i>	84
Results:	84
Physiological parameters:	84
Macroscopic appearance:	85
Tissue enhancement:	87
Histology:	89
Discussion:	93
Limitations of the study:	94
Conclusion:	94
CHAPTER THREE	96
Enhanced Role for Apoptosis in a hepatic ischaemia-reperfusion injury model	96
Abstract:	96
Introduction:	97
Method:	100
Tissue samples:	100
Immunohistochemistry assays:	102
Quantitative apoptotic index:	102
Microscopic examination:	104
Statistical Analysis:	106
Discussion:	108
Conclusion:	109
CHAPTER FOUR	110

Contrast-enhanced ultrasound provides better evaluation of microwave ablations in an ex vivo perfused porcine liver model	110
Abstract:	110
<i>Background:</i>	110
<i>Aims:</i>	110
<i>Material and methods:</i>	110
<i>Results:</i>	110
<i>Conclusion:</i>	110
Introduction:	110
Material and Methods:	111
<i>Liver Procurement:</i>	111
<i>Circuit preparation</i>	111
<i>Microwave ablation:</i>	111
<i>Liver scanning:</i>	114
<i>Quantification of MBs in the ablated zone:</i>	120
Results:	123
Grey-scale US:	123
CEUS:	125
<i>Histology:</i>	126
<i>Data comparison:</i>	133
<i>Quantification of the MBs in the ablated area:</i>	135
Discussion:	136
Limitations of the study:	138
Conclusion:	138
CHAPTER FIVE	139
Increasing Microwave ablative power enhances Apoptosis Expression in an ex-vivo liver perfusion model	139
Abstract:	139
Introduction:	139
Method:	140
<i>Specimens:</i>	140
<i>Antigen retrieval:</i>	142
<i>Immunohistochemistry assays:</i>	142
<i>Quantitative apoptotic index:</i>	142
Results:	142
<i>Microscopic examination:</i>	142
<i>Statistical analysis:</i>	147
Discussion:	151
Limitations of the study:	151
Conclusion:	152
CONCLUSIONS:	153
FUTURE DIRECTIONS OF THIS PROJECT:	156

REFERENCES:	158
PUBLISHED ARTICLES:	176
MEETINGS AND CONFERENCES.....	177

Abstract

Background:

Contrast-enhanced ultrasound (CEUS) using microbubbles (MBs) as contrast agents has improved ultrasound (US) imaging techniques over the past two decades. It has also been used to guide microwave ablation (MWA) in cancer treatment and in ischaemia-reperfusion injury (IRI) to better understand the associated pathological changes such as apoptosis. MWA itself is known to induce apoptosis but the extent has not been precisely quantified.

Aims:

In this four-part project, I used an ex vivo porcine liver perfusion model to evaluate:

- 1. The use of CEUS in the assessment of MWA injury and in the detection of IRI.*
- 2. The extent of apoptosis from the expression of Caspase-3 and M30 in a time-dependent manner in IRI.*
- 3. The relationship between ablation power employed and extent of apoptosis.*

Method:

For parts 1 & 2, ten porcine livers were scanned with US pre and post MBs administration. Biopsies from perfused and non-perfused areas were taken at different time points starting immediately before dissection of the livers and ending at 4 hours of perfusion, and were assessed for ischemia using Haematoxylin–Eosin (HE) staining and for apoptosis using Caspase-3 and M30 monoclonal antibodies.

For parts 3 & 4, multiple ablations at different power settings were created in five more livers. The lesions were then compared in size, morphology, grey-scale US and CEUS. Biopsies from the lesions were scored for apoptosis in each of three zones: a central necrotic zone (CNZ) in the path of the microwave, a transitional penumbra zone (TZ) around this and a surrounding zone of normal tissue (NZ). Statistical analysis was done using AVOVA and *t*-test with statistical significance set at the conventional $p < 0.05$.

Results:

There was enhancement of the entire parenchyma on both grey US and CEUS at 1h, but after 4h multiple perfusion defects that were not evident on grey US were detected on CEUS. Histology confirmed that the non-perfused areas at 4hr were ischaemic.

Caspase-3 expression gradually increased over time in all samples. There was a highly significant difference between Caspase-3 and M30 at 1h in non-perfused areas “NP” ($p=0.001$) which peaked at 4hr in both perfused “P” ($p=0.001$) and NP areas ($p=0.03$). A similar pattern was noted with M30 which peaked at 1hr P ($p =0.001$) and maintained a non-significant difference in expression at 4hr P ($p=0.07$) & 4hr NP ($p =0.1$).

CEUS showed better demarcation of the ablations when compared with Grey-scale US with a highly significant difference in lesion size between different powers ($p=0.0064$). No Caspase-3 expression was seen in CNZ but it was significantly increased in TZ between 50W and 90W ($p=0.009$), highly significantly in NZ ($p=0.003$) for the same powers and significantly between 50W and 70W ($p=0.01$). No M30 expression was noted in CNZ while in TZ, significant difference was noted between 50W and 90W ($p=0.02$). In NZ, the difference was not significant.

Conclusion:

In this model CEUS showed greater definition of perfusion defects and better demarcation of lesions created by microwave ablation. This provides a basis for further studies to determine if CEUS might facilitate better detection and characterization of perfusion defects in the in-vivo setting and in transplanted livers. In the clinical setting CEUS could provide a more precise tool for assessing the ablation zone for a given size of lesion during treatment.

The expression of Caspase-3 and M30 confirms that apoptosis plays an important role in MWA -induced tissue loss. The enhanced apoptotic response in the transition zone with increasing MWA power may help eradicate cancer cells that escape the heat in the ablated zone in the clinical setting. Inhibiting Caspase-3 and M30 might be a useful adjunct in alleviating hepatic reperfusion injury. Further research is required confirm these results.

Introduction

The central theme and tool of this project is enhancement of ultrasound (US), a safe and versatile area of increasing medical utility and interest. In this project, Microbubbles (MBs) were used as *contrast agents* to enhance US images in the investigation of the effects of microwave ablation (MWA) and in the assessment of ischaemia-reperfusion injury (IRI) using a perfused liver preparation. It is therefore pertinent to introduce the tools, namely US and MBs as they apply to the project, without delving into their fiendish physics with its intimidating equations.

A *contrast* is an exogenous substance that can be administered either into the blood stream or into a cavity to enhance an image signal (1). MBs meet this criterion. They are thin-shelled, encapsulated, composite microspheres 1-10 μ m in diameter (2, 3) made of a gas core and a complex chemical coating. Their small size enables them to permeate through microcirculation when injected into the blood stream but it is their *physical* interaction with US waves that makes them uniquely suitable as contrast agents thus offering a new investigative and diagnostic tool. Their complex *chemical* composition allows them to be used to be exploited to bind and carry different substances for remote, targeted drug and gene delivery, thus providing an exciting new therapeutic tool (4-6). This work relates to their use as an investigative tool in a well-established isolated liver perfusion model using warm autologous blood at a Leicester University Department's laboratory renowned for its interest in the field of artificial liver. Chapter two and four works were carried out between 2009 and 2011, and the supplementary chapter three and five were carried out in 2017

A suggested diagnostic application of MBs is the enhancement of tissues in IRI injury to differentiate between healthy and necrotic tissue. Necrosis is premature death of cells in living tissue by autolysis. This results in the loss of the plasma membrane permeability barrier and the formation of blebs that lead to the release of cellular enzymes and other contents (7). Recent reports have suggested that apoptosis is another mechanism of cell death in warm and cold hepatic IRI. Apoptosis is a more controlled process of programmed cell death and it plays a critical role in controlling cell number and proliferation during tissue growth (8, 9). A variety of stimuli may activate the process but the final objective is the cleavage and destruction of the DNA by the activation of a series of proteases called Caspases. On histology, apoptosis is manifested by nuclear chromatin condensation, fragmentation, membrane blebbing, and cell shrinkage (10, 11). Several studies have shown that apoptosis can be enhanced by using contrast-enhanced US (CEUS) (12-15).

An application of MBs is in the detection and management of liver lesions in many clinical specialties (16). In this setting, CEUS increases the sensitivity for lesion detection and the specificity in differentiating between benign and malignant diseases on the basis of enhanced visualization of the tumour microcirculation (17). Association with intraoperative ultrasound (IOUS) affected intra-operative management in 25% of cases (18), and helped achieve complete ablations in most patients (19). This potential use can be explored further by using MBs during ablative treatment of liver cancers.

Microwave thermal energy has been used to palliatively ablate liver tumours. Its advantages in terms of short duration of treatment and the completeness of ablation in the treated volume of liver make it increasingly attractive in the clinical setting (20). It works by raising tissue temperature to supra-physiological levels that cause coagulative necrosis with discernible changes at molecular, cellular and macro-histological levels in the immediate vicinity of the ablative energy. Further afield centrifugally, (away from the centre of ablation and adjacent to cell necrosis) occurs a zone of transition (between necrosis and intact cells) where a delayed and indirect apoptotic response of a variable degree takes place. This apoptotic response can potentially be of further therapeutic interest in the prevention of tumour recurrence. A complete ablation should include the entire tumour plus a safety margin of 5-10mm in a sphere of necrosis to cover this transition zone. A smaller area of coagulation than the size of the lesion may lead to local recurrences whilst a larger area of necrosis may cause unwarranted collateral damage (21). An accurate assessment of the ablation is of crucial importance, considering that complete tumour ablation significantly increases patient survival. MWA is therefore an apt method to create model lesions to assess.

The aim of this work was therefore to develop a method of assessing and quantifying the extent of microwave-created thermal lesions in an *ex-vivo* perfusion model. The ablations represent model lesions simplified by the absence of complex host physiological and metabolic responses. Although grey-scale and Doppler US modes were also run along with the MB-enhanced modes, it was not for the purposes of a head to head comparison. To my knowledge this work has not been done previously.

Previous work on MWA has focused on characterising its tumour ablation potential and its ability to cause cell necrosis in relation to different MWA variables such as wavelength of microwave used, energy application time and power in watts used. Apoptosis has also been explored in the ablated areas (22, 23). Whether its effect is protective against cancer or is procarcinogenic itself is debatable (24-26).

The hypothesis was that MB-enhanced US images could be used to assess areas of tissue necrosis and apoptosis in perfused liver ablated by microwave and to assess areas of IRI. The model used met the conditions for these assessments. For the IRI study, the 2-hour period between explantation of the liver and the start of perfusion of oxygenated autologous blood represented a period of cold ischaemia, akin to what obtains in organ transplantation. It is envisaged that this work could provide the basis for live *in vivo* animal work with the full gamut of host responses, the lack of which has limited the applicability of the current model.

Basics of Ultrasound:

Sound is a form of energy caused by vibration and propagated through a transmission medium as a pressure wave of alternating cycles of compression and rarefaction [Fig. 1]. The frequency of sound is the number of cycles per second and is expressed in Hertz, a Hertz being one cycle per second. Humans can only hear sound of a frequency range of between 20Hz and 20kHz. Sound of less than 20Hz frequency is termed *infrasound* while sound of more than 20 kHz frequency is classified as *ultrasound* and both are inaudible, even though they have the same characteristics as audible sound. US frequencies have a number of applications in medicine and research. Such applications rely on the generation of an image which can be manipulated.

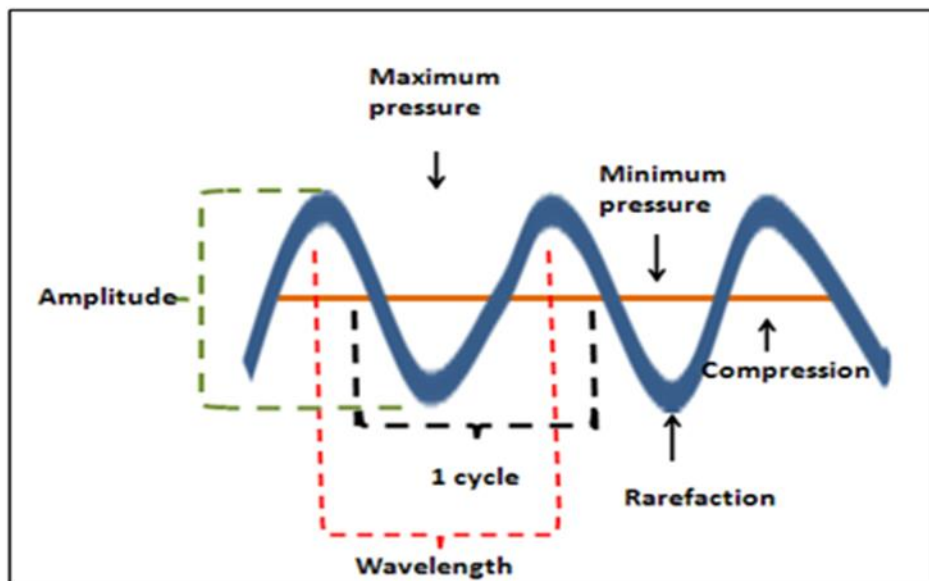


Figure 1. Components of a sound wave

To create an image, a transducer emits an ultrasound wave which is reflected as it passes through an object, such as tissues. It is these reflected echoes that form the image. A typical transducer [Fig. 2] houses ceramic or quartz crystals that possess the dual property of vibrating to produce sound waves upon application of an external voltage and converting the reflected waves into voltage, a process called piezo-electric effect (27, 28) This interconversion of electrical and ultrasound energy underpins the ability of the material to be used both to generate US waves of a chosen frequency to interrogate target tissue and to produce an image from the reflected waves. The natural resonant frequency of the transducer

responds to a wavelength that is double the transducer thickness. For medical imaging, the frequencies used typically range from 1MHz to 40MHz (27).

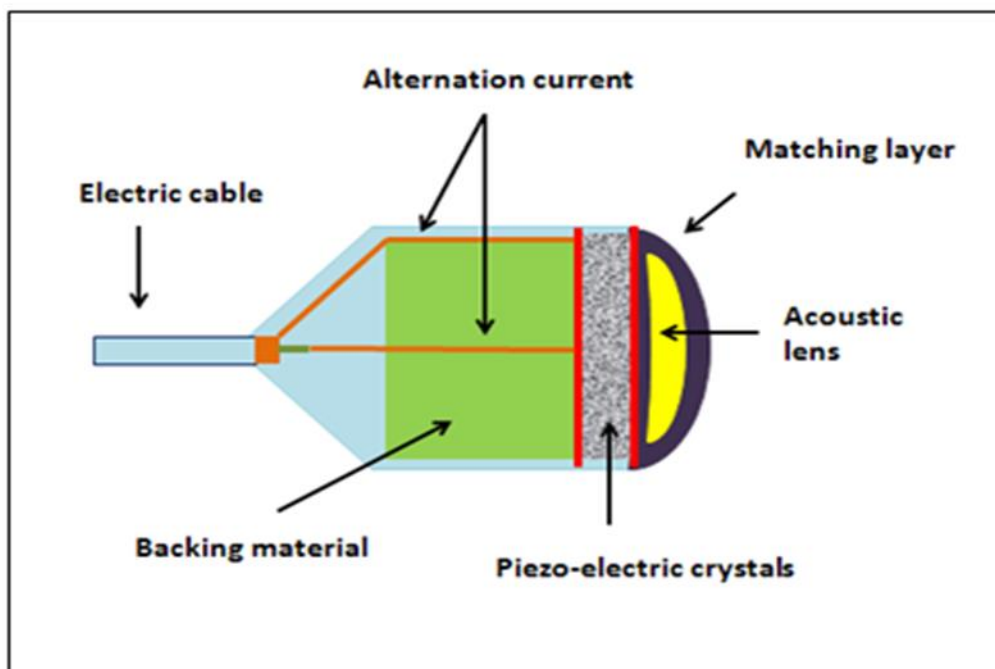


Figure 2. Ultrasound transducer

Tissue elements interact with the incident US beam in a number of ways that impact on the final wave returning to the transducer and therefore the resulting image. Not all the transmitted wave is reflected back to the transducer. Tissue constituents of different acoustic impedance can cause a *reflection* of the incident wave at the interphase and its *refraction* or bending as it is propagated. Tissue also *absorbs* and scatters some the transmitted wave (29). *Scattering* is the chaotic redirecting of the wave in multiple directions due to the irregularity between the wave and the medium it passes through [Fig. 3].

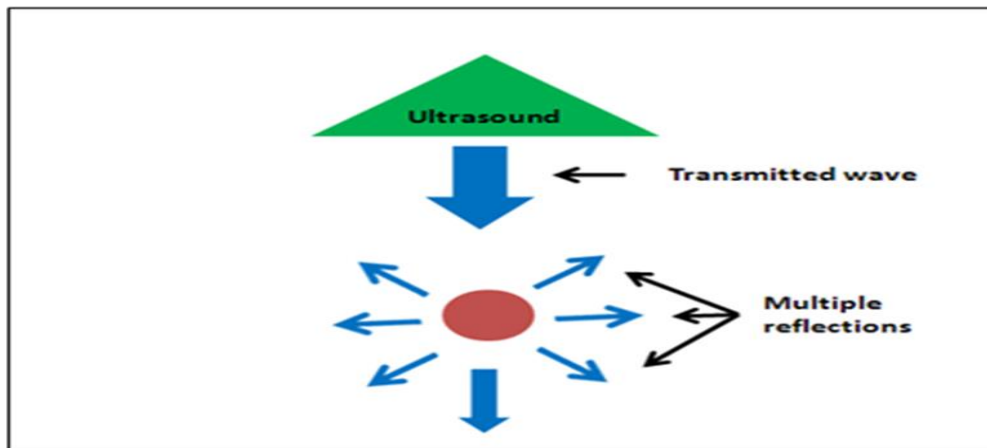


Figure 3: Scattering

US Imaging:

An US image can be generated in a variety of ways and its quality is influenced by several parameters. The *depth* is the distance from the transducer to the focal point of interest. A high frequency US wave has low penetration and therefore gives better resolution for superficial tissues, while a low frequency US penetrates deeper but with lower resolution (27, 30). *Resolution* refers to the ability to identify two objects or points as distinct and is divided into two types, temporal and spatial (30, 31). Temporal resolution is making that distinction at a particular instant in *time* and depends on frame rate. It can be reduced by reducing line density, depth or by narrowing the sector angle to the area of interest. Spatial resolution is the ability to distinguish two objects which are close to each other in *distance* and is divided into axial and lateral. Axial resolution is distinguishing objects at slightly different depths along the axis of the beam. This effect can be reduced by using high frequencies but at the expense of depth. Lateral resolution is when the two objects at a right angles to the beam line. It depends on the beam width and can be reduced by minimising gain, or using high frequencies.

Grey-scale ultrasound refers to the conventional black-and-white image display on the scanner when the Brightness “B” mode setting is selected (29). When a transmitted wave hits a boundary, the reflection back to the transducer is linear (31). The *brightness* of a point on the screen represents the strength of the reflected signal (27).

Real-time imaging ultrasound denotes the production of motion pictures when the frames are fast enough to allow movements to be followed. Frame is the rate at which an image is updated to produce unique consecutive images (31). Ten movements per seconds are usually required to appreciate movements (27) so real-time US is expressed in number of frames per second (FPS). In this type of imaging, when the transmitted wave hits a moving interface, the reflected frequency’s pitch width changes before it is reflected back to the transducer. This altered pitch is amplified through a microphone, and the changes are processed in the scanner

to produce images or graphs representing information about the velocity and the direction of flow. The scanner computer can convert velocity into colour to produce a colour Doppler image (27). In clinical practice this allows dynamic assessment of blood flow in larger vessels but has a low sensitivity in evaluating tissue microcirculation due to significant colour and motion artefacts (32). In grey-US imaging the signal is transmitted and received at the same frequency but in conventional *Harmonic imaging*, the transducer emits low-frequency 'fundamental' waves with a narrow range of frequencies (narrow *bandwidth*) and receives high frequency echoes (33) without fundamental and harmonic wave overlap. The image is formed from the harmonic component after filtering out the fundamental frequency, but at the expense of resolution (34) Enhancement is then needed to optimise quality and extend the utility of US.

Image Enhancement Principles and Techniques:

Enhancement is the improvement in image quality when the reflected waves are not reinforced (30) while *gain* is the amount of amplification of the returning echoes which determines the brightness of an image (35).

Harmonic US images can now be enhanced with contrast (H-CEUS) to address the limitation in image quality on the grey and Doppler scales. H-CEUS produces a clearer image by obliterating unwanted low-frequency signals from tissues surrounding the area of interest such as a hepatic lesion to increase its visualization (36, 37). Another Harmonic technique is *Pulse inversion* [Fig. 4]. In this, the fundamental wave followed by an inverted pulse of the same amplitude without the need to narrow the bandwidth as the scanner is able to separate fundamental echoes from harmonic ones as the two waves nullify each other due to linear scattering. This results in an image with improved resolution (34) without the use of a contrast agent. Pulse inversion can also be combined with power Doppler harmonic imaging to produce *Power pulse inversion* image. Several waves with alternating phases are emitted and the reflected signals are then combined to eliminate tissue motion artefacts (34).

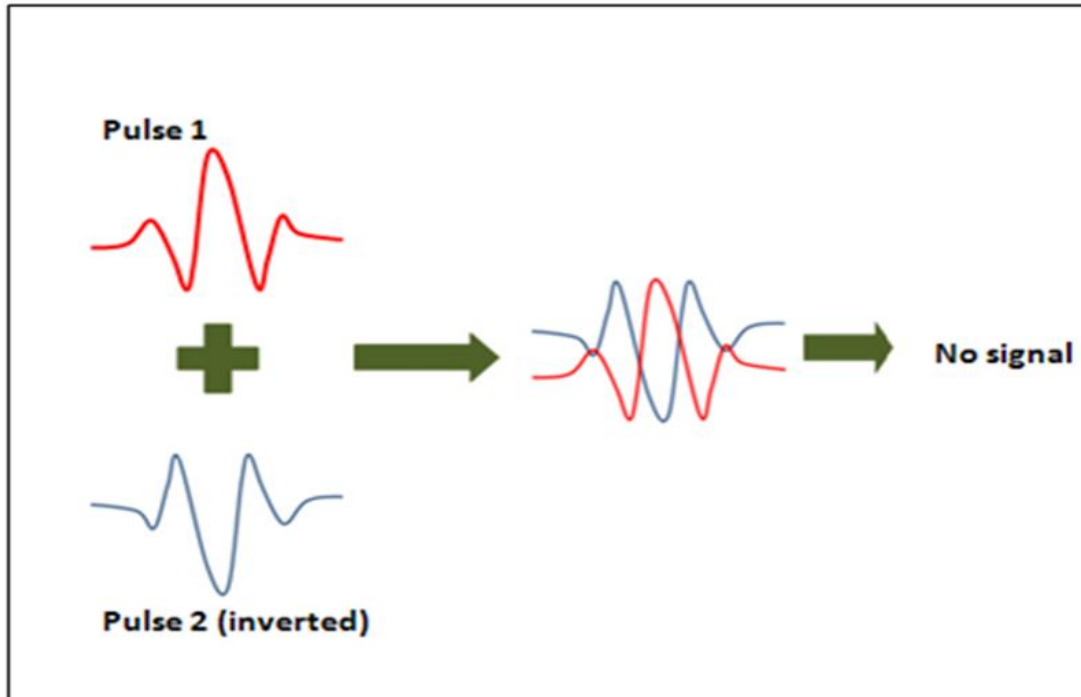


Figure 4. Pulse inversion technique

It is clear from this elementary account of US imaging that there is ample scope for further image enhancement and a permutation of options for its manipulation. It is here that contrast agents like MBs come in, opening up new and exciting diagnostic and therapeutic possibilities such as with MWA.

Microwave ablation in clinical practice:

MWA is one of the new developing trends for treating cancer. Its mechanism of action is based on heat generation by inserting an applicator “connected to a microwave generator” into tumours (38, 39). The emitted electromagnetic waves cause friction movements of water molecules which generate heat ranging from 900MHz to 2500 MHz (40, 41). The heat is evenly conducted throughout the surrounding tissues around the applicator resulting in a spherical thermocoagulation zone (40, 42). Like with other trends of thermal ablation, although to a lesser extent, the generated heat with MWA can cause charring of the central tissue around the probe, especially with high power and long duration (43). This carbonated layer acts as a barrier to heat conduction to the surrounding transitional zone (TZ) (41). This zone lies between the central necrotic zone (CNZ) and the peripheral unablated tissue. The TZ is where the highest rate of tumour recurrence occurs and is therefore of interest in further study. Although not directly afflicted by coagulative necrosis, the cells of the TZ may acquire membrane damage with a sufficient “cell stress” signal to induce apoptosis, thus serving to reduce the risk of recurrence whilst avoiding unnecessary application and duration of ablative energy.

After ablation, the reactive tissue inflammation is shown as a hyperaemic rim surrounding the ablated zone (44-47). This rim makes it difficult to differentiate between complete ablation and residual tumour (44, 46-48). The rim is not visible on grey-scale US, but with contrast (CT, MRI, CEUS), it is shown as uniform in thickness in benign lesions and irregular if residual tumour is still present in the ablated lesion (46, 48). Hence, immediate evaluation of the ablated zone is required to achieve complete lesion destruction in situ (39, 48).

Understanding microwave physics

Definition of microwave radiation:

It is the region of the electromagnetic spectrum with frequencies between 900 MHz and 2450 MHz (38).

Mechanism of action as a heating wave:

Electromagnetic microwaves produce heat by interaction with water molecules. When a radiation wave passes through water, it causes spinning of water molecules in different directions 2-5 billion (38). This happens because of the interaction between the radiation charge and the water molecules charges [Fig. 5]. The generated heat depends on the applied frequency and the speed of the water molecules rotation and their friction with the surrounding tissues (38).

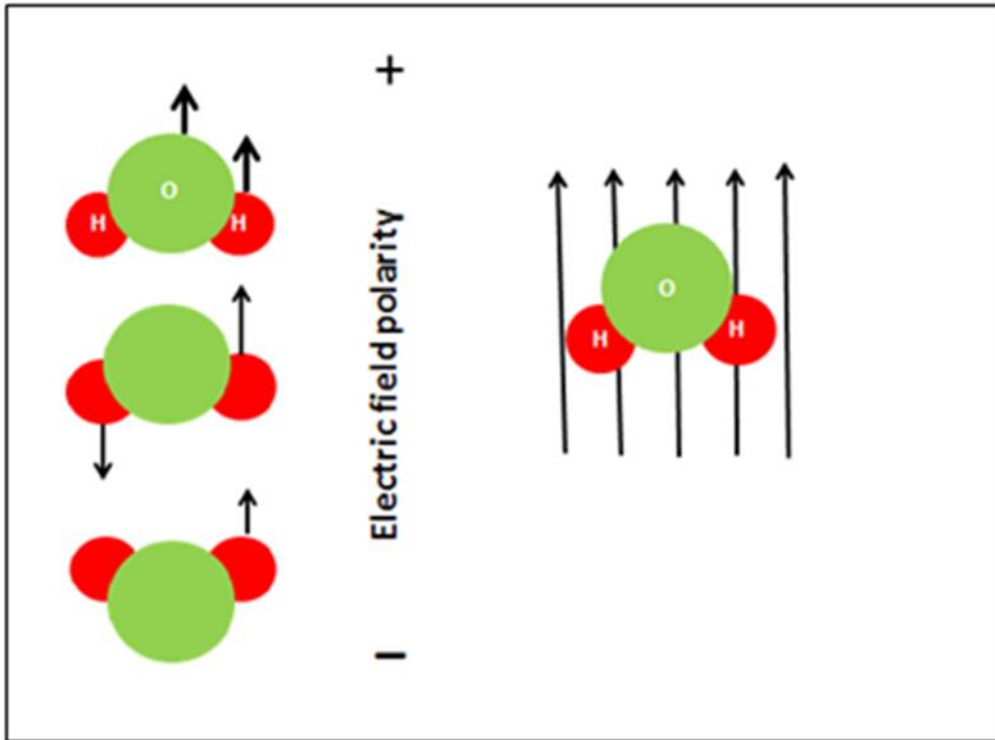


Figure 5. Microwave; mechanism of action as a heating wave

Components of a Microwave ablation System:

The basic microwave ablation system consists of three components:

Generator:

Two types of power sources are used to generate ablation power, a magnetron (accelerated electrons within a magnetic field inside a resonant cavity) [Fig. 6], and a solid-state amplifier (the power is in stages with each stage consisting of a transistor-based amplifier that increases the power of the previous stage [Fig. 7] (49). The generated frequencies range from 915 MHz to 2.45GHz. Each power source has its advantages and disadvantages [Table-1].

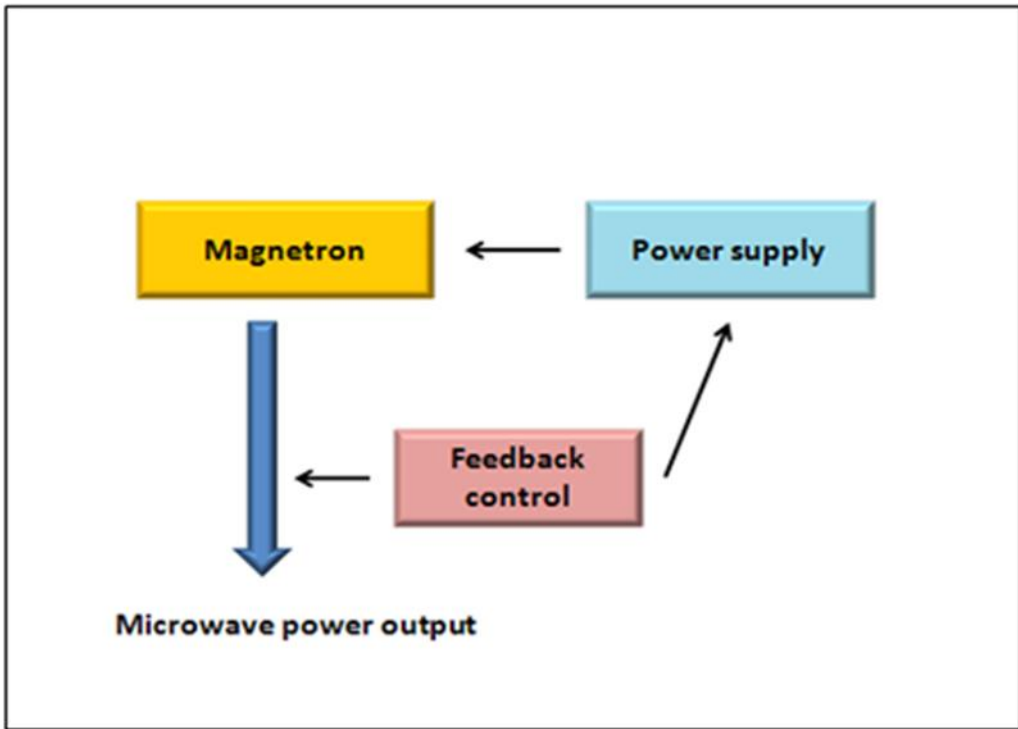


Figure 6. Magnetron generator

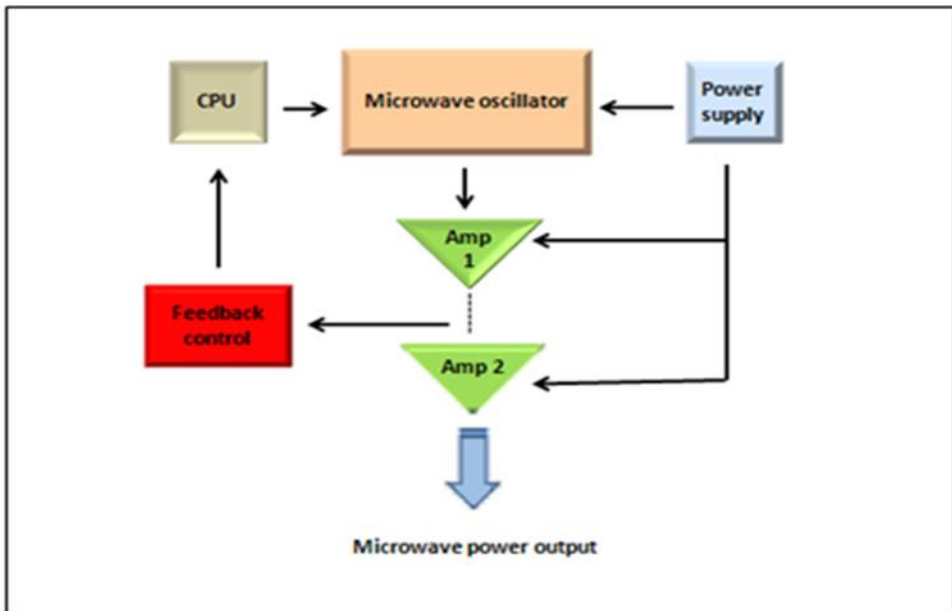


Figure 7. Solid-state amplifier

Characteristic	Magnetron generator	Solid-state generator
Efficiency	High (>70%)	Low (<30%)
Output power	High (>10kW)	Moderate (<150W)
Signal control	Difficult	Easy
Cost	Low	High
Size of the monitoring output system	Large	Small
Generated heat	Moderate	Large
Suitability for number of antennas	yes	No

Table 1. Comparison between magnetron and solid-state generators

Distribution system:

Coaxial transmission line:

This is a cable which distributes power from the generator to the antenna. It has excellent propagation characteristics and consists of an inner conductor, dielectric material, outer conductor and coating [Fig. 8] (40). The material chosen for making the distribution line and its thickness should have the efficiency to conduct power without being over-heated.

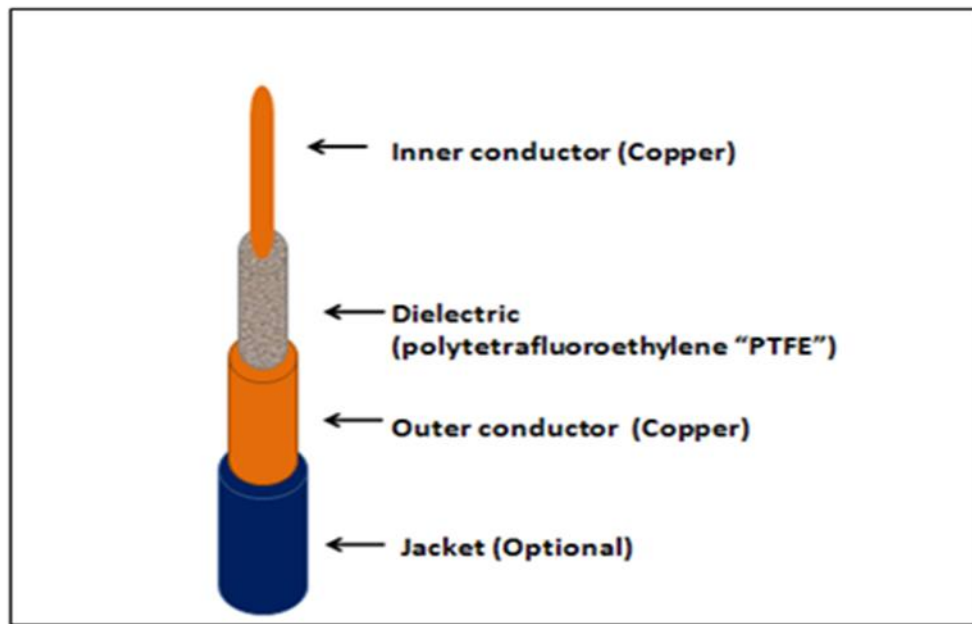


Figure 8. Coaxial transmission line

Power splitters:

The splitters use a geometry line to equally divide input power into output channels (maximum four channels for MWA).

Phase shifters:

These are used with the systems which provide phased-array operation of multiple antennas. The aim is to control heat conduction via overlapping electromagnetic waves (49).

Amplitude modulation:

Amplitude modulation changes the strength of the transmitted signal according to the information being sent. This function provides selective activation of antennas.

Antenna:

This is the final part of the system which conducts the distributed energy from the coaxial line to tissue targets [Fig. 9]. Most antennas are straight in shape and loop or deployable types are also available. Common designs include monopole, dipole, triaxial, choked, or slotted antennas. Specific criteria should be met for an antenna to be efficient, such as minimal invasiveness, the ability to evenly conduct heat into ablated tissue to achieve maximum results with a spherical pattern, and a low reflection coefficient to improve power transfer to tissue (40). Antennas are made in a way to achieve maximum effect by conducting efficient power via reasonable thickness and size without being over-heated

during treatment which can cause unwanted ablations along the shaft of the antenna and skin burns. This over-heating problem can be avoided by using circulated cooled saline or water, or a rapidly decompressed gas (Carbon dioxide) with a special type of antenna (sleeved antennas) (40, 50).

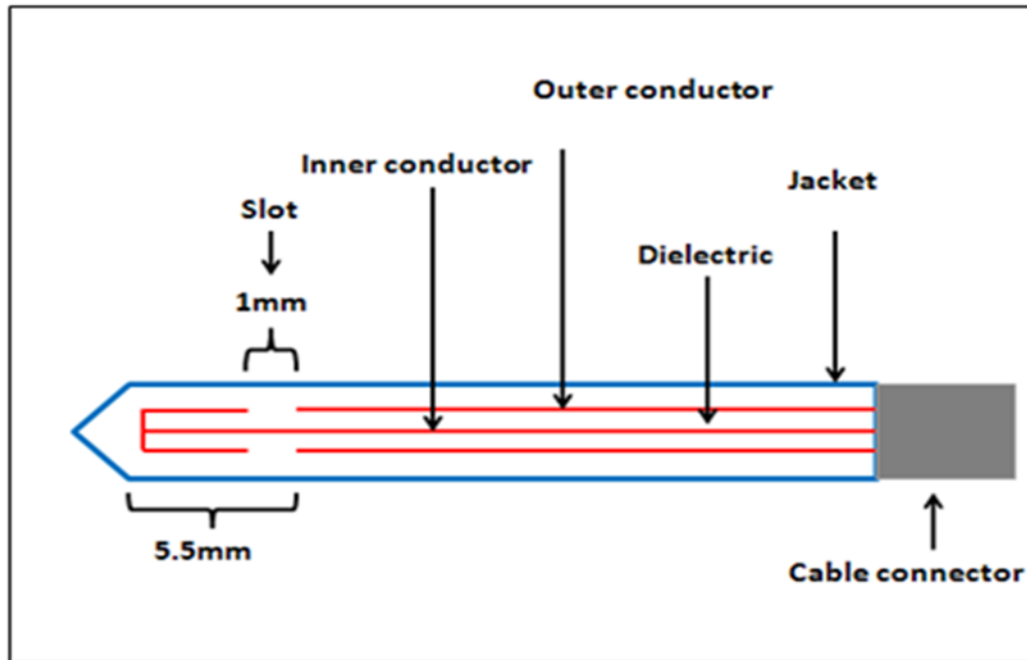


Figure 9. Antenna

Ablative techniques for treating hepatic tumours:

A number of different ablative techniques have been employed for the palliation of unresectable primary and secondary liver tumours. New techniques such as microwave MWA, radiofrequency ablation (RFA) and DC current electrolysis have even been used as alternatives to surgical resection with curative intent (51, 52). Some of the techniques have been largely abandoned due to dangerous adverse effects (cryotherapy), are plagued by high recurrence rates (RFA) or are still under proper investigation (electrolysis). MWA is now a well-established and popular palliative treatment for liver tumours and due to its technical advantages, particularly the short duration of required treatment and the completeness of the ablation process in the treated volume of liver, is being used increasingly in the clinical setting (51). A complete ablation should include the entire tumour plus a safety margin of 5mm-10mm in a sphere of necrosis. An area of coagulation smaller than expected may lead to a local recurrence, and a too large area of necrosis may cause unwarranted collateral damage (53). Following microwave ablation, the ablated region presents radiologically as a low-attenuation, non-enhancing zone (54) that histologically corresponds to two concentric

zones: a central area of coagulative necrosis and, a peripheral transitional area of inflammation, stasis, haemorrhage and thrombosis (55). While the coagulative zone is occupied entirely by dead cells and amorphous material, the transitional zone may still contain viable cells, causing recurrence (55). An accurate assessment of the ablation therapeutic response is of crucial importance, considering that complete tumour ablation significantly increases patient survival, and avoids additional treatment of the residual tumour in the incompletely ablated area.

In the medium term following microwave ablation (one to three months) a hyperaemic rim frequently appears on CT and MRI (54, 56). The result of this appearance is an important clinical dilemma because it may not be possible to differentiate healthy healing tissue (the normal physiological response to injury) from tumour recurrence (meaning a treatment failure that requires urgent intervention) (57, 58). Residual unablated tumour is defined as a portion of a treated lesion showing persistent hypervascularity in the arterial phase, usually appearing as an irregular peripheral-enhancing focus in the ablation zone, often at the deeper aspect of the nodule, in proximity to major perinodular vessels (21).

Characterisation of liver tumours using CEUS:

MBs have improved characterisation and detection of focal liver lesions as the enhancement criteria can be visualised in real time over a 5 minute period (59). With the second generation of MBs, real time imaging is performed through all vascular phases: the arterial (early) phase (15–35 seconds after injection), the portal (venous) phase (35–90 seconds), and the sinusoidal (parenchymal or late vascular) phase (90–240 seconds) (59). The ability of the MBs to detect still viable tumour during the RFA session after completion of the procedure may prompt immediate retreatment during the same session, thus dramatically reducing the rate of unsuccessful treatment, improving cost-effectiveness ratio and optimising patient management (21).

CEUS increases the sensitivity for lesion detection and the specificity to differentiate between benign and malignant diseases due to the enhanced visualization of the tumour microcirculation. Results achieved seem at least equivalent to those of spiral CT or MRI. The association of CA with intraoperative ultrasound has changed the surgical approach in 25% of patients and guaranteed complete ablations by a single session in most of them. CEUS provides detailed information about tumour vasculature, improves the preoperative characterization and therefore the therapeutic strategy, and can evaluate the intraoperative completeness of the ablation.

Contrast-enhanced ultrasound in the preoperative, intraoperative and postoperative assessment of liver lesions:

Although hepatic tumours require resections for definitive treatment (60), about 20%–30% of patients with liver-only metastases are potentially resectable (61) due to patient's poor clinical status, extensive involvement of the parenchyma or peculiar positioning of the lesions too close to major blood vessels (62). An accurate characterization of the hepatic involvement and of the relationship with major vascular structures is of paramount importance in the preoperative planning and intraoperatively to evaluate the completeness of treatment. Historically, grey-scale US has been the first tool for the detection and characterization of liver lesions (63) due to its availability, safety and low cost. However, the low sensitivity (40%–77%) and specificity progressively limited its applications, favouring over time cross-sectional imaging modalities such as CT and MRI (63). This is particularly true for small lesions where the US sensitivity is even lower than that for larger lesions or for those lesions with insufficient echogenic contrast compared to surrounding tissues (18, 64-66) However, the radiological evaluation of ablated tissues poses serious limitations to cross-sectional imaging, especially with regard to the postoperative differentiation of tumour recurrence from the normal scarring process. Recurrences are usually present as a rim of contrast uptake peripheral to the ablated area (54, 67) in the transitional ischemic zone that surrounds the core ablated zone (57, 58, 68, 69) and also where the scarring process normally takes place. In this view, CEUS could provide additional data in a non-invasive and readily available setting to not only detect and characterize the lesion preoperatively, but also during the procedure (intraoperative ultrasound: IOUS) to guarantee complete ablations, and postoperatively to evaluate eventual recurrences from benign periablational enhancement and fibrosis (69).

Contrast agents for the study of liver lesions:

According to the European Federation of Societies for Ultrasound in Medicine and Biology, CA for hepatic US imaging are useful to measure the hepatic transit time, study the hepatic vessels, characterize focal liver lesions, and guide and monitor local ablative treatments (70). Lesion echogenicity is defined with respect to the surrounding echogenic levels, therefore, lesions are classified as hyperechoic, isoechoic (undetectable) or hypoechoic compared to the adjacent hepatic parenchyma (70). The uptake of contrast depends on the amount of normal hepatic tissue and the vascularization of the lesion. Therefore, it is generally high in haemangiomas and hepatocellular carcinomas (HCC) (71, 72) which are highly vascularized lesions, and hypoechogenic in liver metastases [Table-2] (17).

Lesion	Conventional US/Doppler	CEUS		
		Arterial phase	Portal phase	Parenchymal phase
HCC	Hyperechogenic foci in 50%, basket pattern in 75%	Hyperechogenic	Homogeneous or heterogeneous hypoechogenic	Hypoechogenic, perfusion defect (73), according to histological grading (74)
Metastases	Hypoechogenic	Peripheral echogenic (rim-like, mosaic-like or diffuse)	Peripheral echogenic or hypoechogenic	Hypoechogenic perfusion defect (73)
Haemangioma	Hyperechogenic foci	Early peripheral nodular echogenic (clumpy filling)	Peripheral/homogeneous echogenic + centripetal fill-in.	Hypo- or isoechogenic + centripetal fill-in
CCC	Hyperechoic >3 cm, hypo- or isoechogenic <3 cm	Peripheral rim-like echogenic or heterogeneous echogenic	Hypoechogenic or isoechogenic	Hypoechogenic perfusion Defect (73)
Lymphoma	Multiple well-defined hypoechogenic masses	Homogeneous, peripheral rim-like echogenic	Heterogeneous, hypoechogenic	Heterogeneous, hypoechogenic perfusion defect
FNH	Isoechogenic, central	Pronounced arterial	Pronounced early portal	Isoechogenic with

	hypoechogetic scar in 45%, central feeding artery with spoke-wheel sign	enhancement, homogeneous with spoke-wheel sign in 89%: (75) centrifugal Progression of enhancement (76)	venous enhancement (75) consequently isoechogenicity in the late portal phase (76)	central scar (77)
Adenoma	Well-defined hyperechogenic mass	Homogeneous or heterogeneous echogenic	Iso- or hypoechogenic	Iso- or hypoechogenic
Focal fatty changes	Hyperechogenic Mass	round Isoechogenic	Isoechogenic	Isoechogenic
Cyst	Isoechogenic, thin-walled	Non-echogenic	Non-echogenic	Non-echogenic
Abscess	Early stage: irregular, variable echogenicity. Late stage: round, hypoechogenic + debris and thick-walled	Rim-like echogenic, honeycomb sign, diffuse heterogeneous echogenic	Rim-like echogenic, honeycomb sign, diffuse heterogeneous echogenic	Rim-like echogenic, honeycomb sign, diffuse heterogeneous echogenic
Hematoma	Hyperechogenic	Non-echogenic	Non-echogenic	Non-echogenic

Peliosis hepatitis	Hypo- or hyperechogenic	Fast surge, central echogenic	Iso- or hypoechogenic	Iso- or hypoechogenic
Skip area in fatty liver	Hypoechogenic pseudolesion	round	Isoechogenic	Isoechogenic
Intrahepatic extramedullary haematopoiesis	Hypoechogenic	Hyperechogenic	Hyperechogenic	Hyperechogenic

Table 2. Enhancement patterns of focal liver lesions (grey-scale vs CEUS). [CCC = cholangiocarcinoma], [CEUS = contrast-enhanced ultrasound], [E = echogenic], [HCC = hepatocellular carcinoma], [US = ultrasound] (48, 52, 59, 65, 78-83)

Liver tumours known to be hyperperfused in the arterial phase (e.g. HCC) (71) can be detected and characterized easily (56). Hypoperfused tumours in the portal venous phase (e.g. liver metastases of the gastrointestinal tract) can be recognized as less perfused “black spots” [Table-3] (56).

Ref.	Year	Study type	Comparison	Patients number	Lesion	Contrast agent
(84)	1999	Prospective	CEUS vs US	50	HCC, HEM, METS, CCC, FNH, others	Levovist
(71)	2000	Prospective	CEUS vs US	100	HCC, HEM, METS, FNH, CCC, other	Levovist
(85)	2003	Retrospective	–	90	HCC, METS, HEM	Levovist
(66)	2003	Prospective multicentre	CEUS vs CT	123	METS	Levovist
(86)	2005	Retrospective	–	59	HEM	Levovist
(87)	2006	Prospective	CEUS vs US	138	HEM, FNH, HCC, adenomas, METS, abscesses, cysts, others	SonoVue
(78)	2006	Prospective	–	586	HCC, HEM, METS	Levovist
(88)	2006	Prospective	CEUS vs US or CT	253	METS	SonoVue, non-ionic iodinated CA
(89)	2006	Prospective	CEUS vs CT	41	HCC	SonoVue
(90)	2007	Prospective	–	125 non- cirrhotic, 67 cirrhotic	HCC, HEM, METS, CCC, FNH, Focal fatty change, adenomas, dysplastic nodules	Gadovist, Ultravist & Sonovue

(91)	2007	Retrospective	–	68	Unspecified	SonoVue
(92)	2007	Prospective	CEUS vs US	456	HCC, HEM, METS, regenerative nodules, focal fatty change, inflammatory lesions, necrotic lesion, adenoma, others	SonoVue
(93)	2007	Prospective	–	17	Solitary necrotic nodule	SonoVue
(94)	2008	Prospective	CEUS vs US	52 (fatty liver)	HCC, HEM, METS, FNH, inflammatory pseudotumour, solitary necrotic nodule, focal fatty sparing area, CCC), lymphomas	SonoVue
(95)	2008	Prospective	CEUS vs US	128 cirrhotic	Benign, malignant	SonoVue
(96)	2008	Prospective	CEUS vs US	104	HCC, HEM, METS, regenerative nodule, focal fatty change, focal fatty sparing, FNH, abscess	SonoVue
(97)	2008	Prospective	CEUS vs CT	43	HCC	Sonazoid
(98)	2008	Prospective	–	20	Liver lesions	SonoVue
(99)	2009	Prospective	CEUS vs CT	191	HCC, HEM, METS, others	Sonazoid
(100)	2009	Prospective	CEUS vs MRI	–	HCC	Sonazoid
(101)	2009	Prospective	–	135	Cysts, HEM, FNH, HCC, focal fatty sparing, focal fatty areas, regenerative nodules, hydatid cysts, abscess, METS, CCC	SonoVue
(102)	2010	Prospective	–	29	HCC	Sonazoid

(19)	2010	Prospective	–	66	HCC, METS	Sonazoid
(103)	2010	Retrospective	CEUS vs CT or MRI	127	Malignant lesions	–
(104)	2010	Prospective	CEUS vs CT or MRI	159	Malignant lesions, benign	–
(105)	2010	Prospective	CEUS vs CT or MRI	73	Malignant lesions, benign	SonoVue
(106)	2010	Prospective	CEUS vs CT	132	Cysts, HEM, METS, focal steatosis, eosinophilic necrosis, granuloma, abscess, fistula	–
(72)	2011	Prospective	CEUS vs CT	22	Regenerative nodules, HCC	Sonazoid
(63)	2011	Prospective	CEUS vs US	99	Malignant lesions, benign	SonoVue
	2011			46	CCC	SonoVue

Table 3. Characteristics of contrast-enhanced ultrasound studies on the detection and characterization of hepatic lesions. [CCC = cholangiocarcinoma], [CEUS = contrast-enhanced ultrasound], [CT = computed tomography], [FNH = focal nodular hyperplasia], [HCC = hepatocellular carcinoma], [HEM = haemangioma; [METS = metastases], [MRI = magnetic resonance imaging], [RFA = radiofrequency ablation], [TACE = transarterial chemoembolization], [US = ultrasound].

The reason of this phenomenon derives from the nature of the vessels contained in the lesion, mostly arterial in liver metastases. In lesions such as adenomas and haemangiomas, the vascular structures appear isoechoic or hyperechoic due to a similar or superior retention of MBs to the adjacent parenchyma (86, 107), while those containing neoangiogenesis (HCC, cholangiocarcinoma, metastases) may release MBs in the adjacent parenchyma and therefore appear hypoechoic (107). Non-perfused lesions such as a sclerosed haemangioma or necrotic intrahepatic areas also appear as clear hypoechoic defects (93, 107).

The contribution of CEUS is also important for the study of lesions in livers with difficult backgrounds such as cirrhosis. Various enhancement patterns have been described in the cirrhotic liver due to the heterogeneous composition of the liver parenchyma (59). A high sensitivity of the arterial phase was present when CEUS was used for the diagnosis of hepatic malignancies in cirrhotic livers (90). Specific applications for the study of HCC lesions were also derived from the introduction of Sonazoid CA (108). Sonazoid CEUS allows clear observation of tumour vessels and tumour enhancement, permits scanning with 3-D US71 and can combine CEUS images with those from CT or MRI to detect typical or atypical HCC lesions (108). Sonazoid CEUS has been proved able to characterize the gross type of HCC (single nodular, single nodular with extranodular growth and confluent multinodular) (102) and the histological differentiation (109) correctly in most patients, guide radiofrequency ablation (RFA) and evaluate the efficacy of RFA or transcatheter arterial chemoembolization (TACE) (108).

Most studies on CEUS involved different types of hepatic lesions but they all focused on two important outcomes: lesion detection and characterization. The overall CEUS sensitivity for hepatic lesions was 86%–100%, specificity 80%–100%, accuracy 88%–98%, positive predictive value 90%–97% and negative predictive value 89%–96% (21, 32, 78, 85, 91, 102, 103, 105). When compared to non-contrast-enhanced US, CEUS increased the detection (71, 84, 87, 88, 98, 99) and characterization rates (32, 63, 71, 78, 85–87, 94, 96, 110) of hepatic lesions, leading to a more correct diagnosis about their nature (32, 91, 92, 94, 96, 99). The superiority over non-contrast enhanced US was also proved in difficult clinical situations, for example, after chemotherapy or for small metastases (111). CEUS also outlined specific characteristics for peculiar tumours such as cholangiocarcinoma (110). Compared to CT, the CEUS preoperative detection of hepatic lesions was similar (87, 109) or better (66, 88, 99, 112), the correct diagnosis rate was similar (21, 87) or better (99), and the postoperative detection of residual disease after RFA or TACE was generally improved (19, 89, 97). CEUS was also able to correctly diagnose a part of small lesions (<1 cm) that were detected but undetermined at CT (106, 113). In 35%, the addition of CA to US changed the surgical strategy (113). Compared to MRI, CEUS detected more lesions (112, 114) and achieved similar results for the prediction of the histological grading (superparamagnetic iron oxide MRI) (100).

Types of microbubbles used in the assessment of liver lesion:

Levovist:

This is an example of the first-generation of MBs which consisted of air, and was the first type of contrast agents used with US to enhance liver lesions. Air bubbles are generated by adsorption of galactose particles in an aqueous solution and stabilized by a palmitate layer (115). It has an arterial, portal and a parenchymal phase that accumulates up to 20 min within the liver. Only 47% of Levovist is phagocytized by the Kupffer cells (116). Therefore, the parenchyma-specific contrast is only transient, requires a high MI (destructive technique) and the visualization of the whole liver is limited to a single injection and scan (108).

SonoVue:

The second-generation CEUS, “SonoVue” consists of MBs stabilized by phospholipids [Fig. 10] and filled with Sulphur Hexafluoride, an innocuous gas [Fig. 11] (115, 117). It is mainly an intravascular agent (arterial and portal phase) with scarce extravascular distribution and minimal phagocytosis by the Kupffer cells (7.3% of the injected SonoVue) (116). The parenchyma-specific phase lasts for 3–5 min and therefore, a whole liver examination requires multiple injections and scans. SonoVue is used at low MI and is therefore a non-destructive contrast (108).

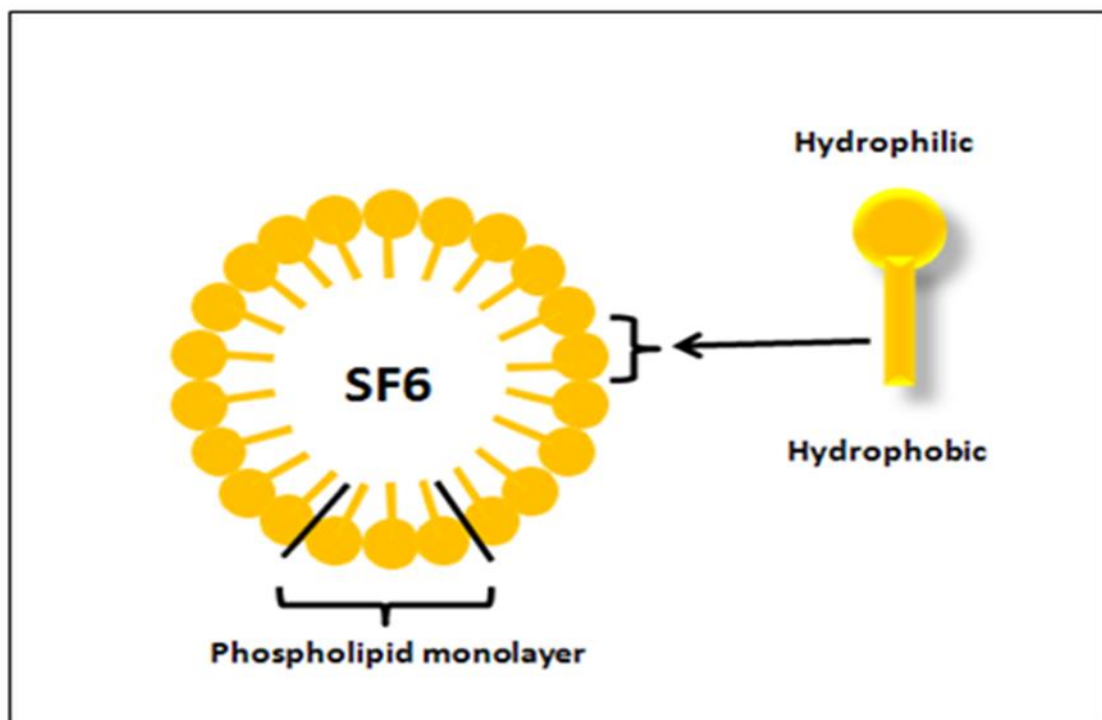


Figure 10. Sonovue microbubble

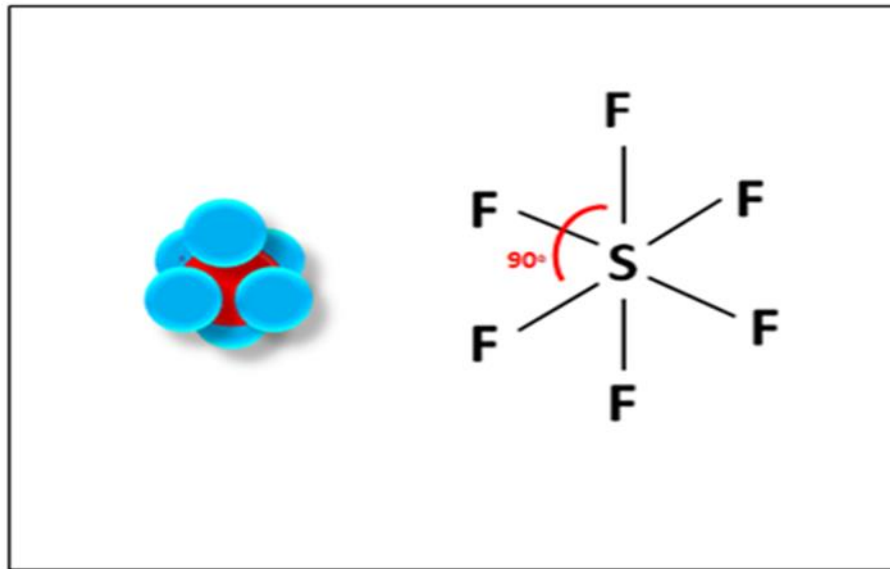


Figure 11. Sulphur Hexafluoride

Sonazoid:

The second-generation CEUS, “Sonazoid” consists of MBs containing perfluorobutane gas [Fig. 12]. It has an arterial, portal phase and is also retained within the hepatic reticuloendothelial cells for 10–30 min after injection due to phagocytosis by the Kupffer cells (99% of the injected Sonazoid) (116). The high stability of Sonazoid has overcome the deficiency of Levovist with the advantages of the long-lasting imaging and the strong contrast effects for more detailed observations. In the parenchymal-specific phase the whole liver can be scanned at a low MI without destroying Sonazoid MBs (102, 118). This method allowed the detection of small malignant lesions as perfusion defects (102, 108, 118). The limitations of using a low MI during the parenchyma-specific phase are in the imaging of hyperechoic lesions (for the background B-mode), or those located deep in the liver (due to the attenuation of the ultrasound beam). In these two settings, Sonazoid parenchymal-specific phase obtained with a high MI show the hyperechoic nodules located in deep portions of the liver as perfusion defect images

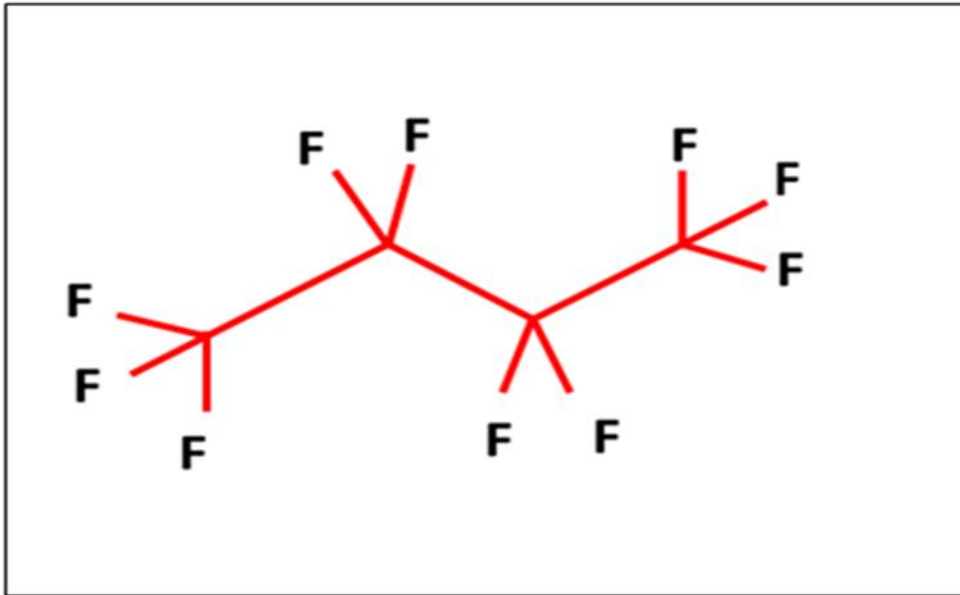


Figure 12. Perfluorobutane gas molecule

Harmonic contrast-enhanced ultrasound:

The harmonic effect can be implemented by the addition of CA to increase the visibility of the local microcirculation and provide additional details on the tissue perfusion compared to the grey-scale US (3). Harmonic CEUS can be conducted in two ways, destructive and non-destructive (119). In the former, the enhancement of liver tissue results from the destruction of Levovist after applying a high MI, thereby increasing the contrast of lesions (120). The latter depends on a low MI that allows continuous real-time imaging of the lesions during the arterial and portal phases over 3–5 min after SonoVue infusion (121, 122). Sonazoid can be used as both non-destructive and destructive CA. Compared to the non-destructive imaging, the destructive imaging of Levovist requires intermittent scanning and the contrast display is only transient (123). Therefore, multiple injections or continuous infusions are necessary with this modality. The high stability of Sonazoid has overcome the deficiency of Levovist with the advantages of long-lasting imaging and strong contrast effects that allow more detailed observations.

Contrast-enhanced intraoperative ultrasound during percutaneous radiofrequency ablation:

One of the main challenges that hepatobiliary surgeons face while performing liver resections and RFA regards the completeness of the oncological treatment in order to prevent any viable cancer cells from causing tumour recurrences. Ideally, the target is to produce a safety margin of 5mm–10mm in the normal parenchyma (55, 68). IOUS can change the preoperative treatment strategy in 20–44% patients due to the higher detection rate of hepatic lesions than preoperative CT or MRI (21, 98). However, it still lacks the ability to diagnose isoechogenic metastases or nodules less than 1cm, does not provide adequate information about lesion vascularization (98), and cannot differentiate between the necrotic tissue and the transitional zone due to the high echogenicity of the gas bubbles produced during the ablation (21). Postoperative CT and MRI could theoretically overcome these problems by detecting a rim of increased contrast in the ablated lesion suggestive of local recurrence. However, these techniques can be performed only after surgery, limiting the influence on the intraoperative decision-making process.

Researchers have been constantly trying new ways to perform a full assessment of the hepatic lesions intraoperatively and, in this setting, CE-IOUS showed promising results [Table-4]. CE-IOUS sensitivity, specificity and accuracy for differentiating HCC have been 65%, 94% and 87%, respectively (124). Its use improved the detection and characterization of hepatic lesions (18, 112, 125), changed the intraoperative management in 25% of cases (18), and decreased the rate of positive margins compared to controls treated without CE-IOUS (73). While pre- and postoperative CEUS helped with the characterization of liver lesions and their follow up, the lack of enhancement of a previously hypervascularised lesion during the arterial phase of CE-IOUS is generally regarded as complete treatment, similar to postoperative cross-sectional imaging (21). CE-IOUS is able to evaluate the various zones created during the ablation by increasing the contrast between the peripheral transitional zone from the central necrotic one thus furnishing important data about the completeness of the ablation (48). Furthermore, CE-IOUS can facilitate RFA electrode placement in hypervascular HCC, which is normally poorly depicted by B-mode US (36, 126), and achieve complete ablations by a single session in 94–95% of patients (19, 36, 127). Another advantage of CEIOUS over IOUS alone is the possibility of diagnosing intraoperative hepatic infarctions that occur during liver ablations (128).

Reference	Year	Study type	Modality	Patient number	Lesions	Contrast agent
(127)	2004	Retrospective	CEUS during percutaneous RFA	162	HCC (n = 192), metastases (n = 97)	Sonovue
(125)	2006	Prospective	CE-IOUS	87	HCC	Sonovue
(36)	2007	Prospective randomised trial (CEUS vs US)	CEUS during percutaneous RFA	40	HCC	Levovist
(18)	2010	Prospective	CE-IOUS	20	HCC (n = 3), metastases (n = 15), CCC (n = 2)	Definity
(73)	2010	Prospective	CE-IOUS	50	HCC (n = 25), metastases (n = 14), CCC (n = 3), gastrointestinal stromal tumour (n = 1), benign haematoma (n = 1)	Sonazoid
(19)	2010	Prospective	CEUS during percutaneous RFA	66	HCC (n = 68), metastases (n = 44)	Sonazoid
(112)	2010	Prospective	CE-IOUS	20	64	Sonovue
(124)	2011	Prospective	CE-IOUS	192	HCC vs other lesions	Sonazoid

Table 4. Clinical studies of contrast-enhanced ultrasound during resections and percutaneous radiofrequency ablation of liver lesions. [CCC = cholangiocarcinoma], [CE = contrast-enhanced], [CEUS = contrast-enhanced ultrasound], [HCC = hepatocellular carcinoma], [IOUS = intraoperative ultrasound]

In this thesis, chapter one explains MBs in details and how they enhance US imaging as contrast agents. Chapter two details the role of CEUS in detecting ischaemic changes in the porcine liver model. Chapter three describes the apoptotic response following ischaemic-reperfusion injury. Chapter four compares the use of CEUS with the grey US in the assessment of MWA. This is followed by chapter five which describes the apoptotic response in the ablated liver tissue in relation to the applied power.

Chapter One

MBs and US Image Enhancement:

Structurally, MBs generically comprise a gas core and a chemical coating [Fig. 13]. The coating may be surfactant, silver, lipids, protein, biopolymer, or galactose (54, 129) and the gas one of a variety of gases including air, Nitrogen, Perfluorocarbon, Perfluorobutane, Decafloropentane, etc. (129-131). This gives manufacturers a permutation of options to produce a number of different MBs combining different sizes with different chemistries and therefore desired properties [Table-5]. They are grouped into classes called ‘generations’.

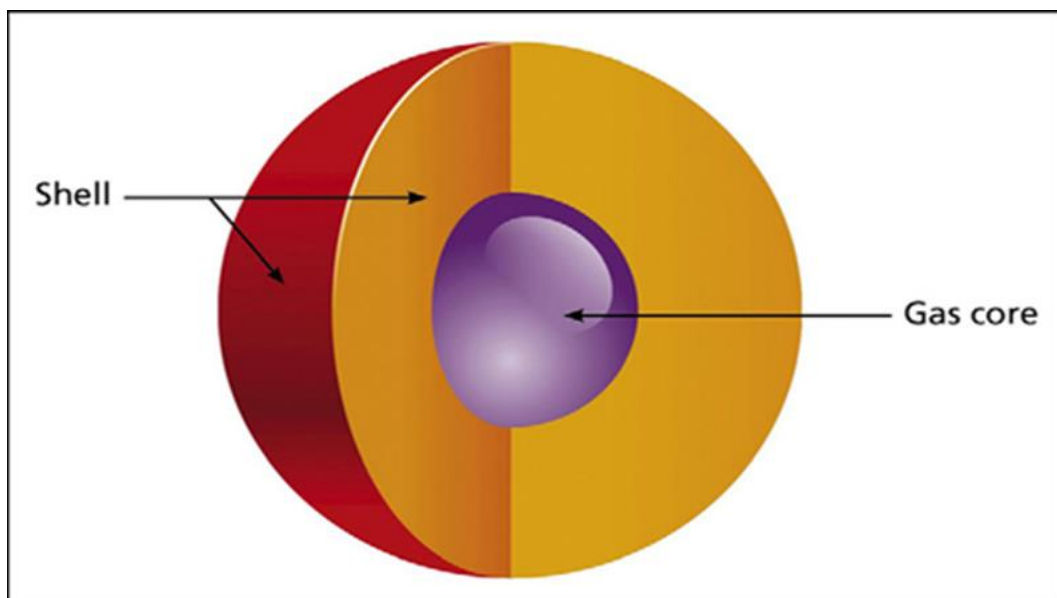


Figure 13. Generic structure of MBs

Microbubble	Company	Shell	Gas	Size (µm)	Net Charge	Storage	Preparation	Approval For Use
Albunex	<u>Mallinckrodt Inc.</u>	Albumin	Air	-	-	-	-	-
Cardiosphere e/ Bisphere	<u>Point Biomedical Corp.</u>	Poly lactide/ Albumin	Nitrogen	4.0	Slight negative	-	Reconstitute with 2ml H2O per vial and dilute with 150 ml DSW	No
AI-700	<u>Acusphere, Inc.</u>	Poly-L-lactide co glycolide	Perfluorocarbon	2	Negative	-	Reconstitute with water	No
Optison	<u>Molecular Biosystems Inc.</u>	Albumin/N-acetyltryptophan, Caprylic acid	Octafluoropropane	2-4.5	Slightly negative	Refrigerate 2-8°C	Hand agitate	USA / Europe
Definity	<u>Bristol-Myers Squibb Medical Imaging, Inc.</u>	Lipids:DPPA, DPPC, MPEG5000 DPPE/surfactant	Octafluoropropane	1.1-3.3	Negative	Refrigerate 2-8°C	Activate through Vialmix agitation	USA
Imagent/ Imavist	Imcor Pharmaceuticals , In	Lipid: DMPC/ surfactant	Perfluorohexane/ Nitrogen	6.0	Neutral	Room Temp 15-30°C	Reconstitute with 10 ml water	USA

Sonovue	Bracco Diagnostics	Lipids: Macrogol 4000, DSPC, DPPG, Palmitic acid	Sulfurhexafluoride	2-3	Negative	No special storage conditions required	Reconstitute with 5 ml saline	Europe
Levovist	Shering AG	Galactose/Palmitic acid	Air	2-4	Negative	Room Temp 15–30°C	Reconstitute with 5 to 17 ml water	Europe/ Japan
Sonazoid	GE Healthcare	Lipid	Perfluorobutane	2.4-3.6	Negative	-	Reconstitute with 2mL water	No
Sonovist	Shering AG	Cyanoacrylate (polymer shell)	Air	1-2	-	-	-	No
Echovist	Shering AG	D-galactose	Air	-	-	Below 30°C	Reconstitute with water	Europe
BR14	Bracco diagnostic	Lipid	Perfluorobutane	2.5-3.0	Negative	-	-	
EchoGen	Sonus pharmaceuticals	-	Dodecafluoropentane	-	Negative	Refrigerate 2–8°C	-	

Table-5. Types of Microbubbles (132-134)

Methods of producing microbubbles:

A variety of techniques have been used to produce MBs depending on their purpose.

Sonication:

Sonication is an example of amalgamation, the process of combining or uniting multiple entities into one form. US waves (>20 kHz) are applied to a medium to produce MBs [Fig. 14]. It enhances the structure of the surfactant monolayer and makes MBs extremely stable, but there is no control over MBs size distribution (135).

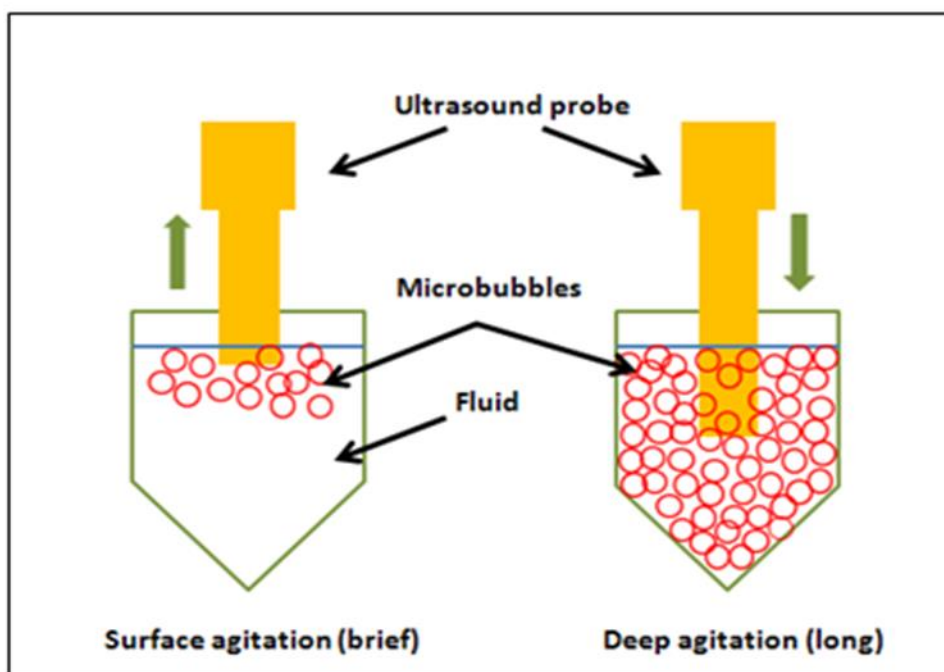


Figure 14. Sonication method for microbubble production

Mechanical agitation:

This is another example of amalgamation by which a gaseous core is entrained into the aqueous phase by mechanical agitation at the gas-liquid interface (136). Again, there is no control over size in this method.

Pressurized liquid-gas mixing:

In this method, MBs are produced by aerating a liquid at a high pressure and temperature [Fig. 15]. This technique is commonly used as it creates the smallest size of MBs when compared with the previous methods, but it has the disadvantage of destroying organic material during preparation (137).

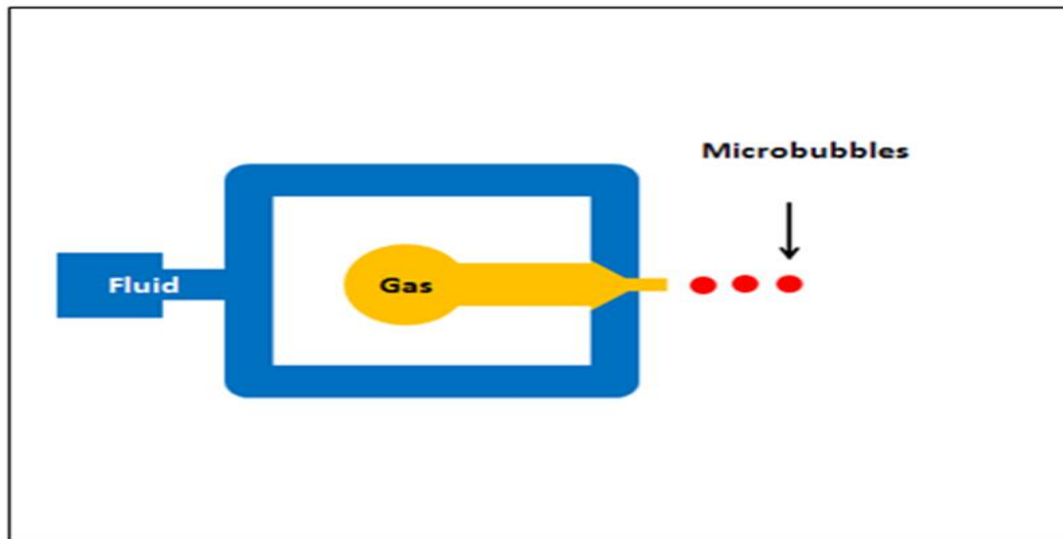


Figure 15. Pressurized liquid-gas mixing method for microbubble production

Generations of microbubbles:

According to the characteristics of the coating and the gas used, different generations of MBs have been created over the years that have led to significant technical improvements.

First generation:

The first generation of MBs (Levovist; Shering AG, Berlin, Germany; or Albunex; Mallinckrodt, Inc, Hazelwood, MO) were filled with air and coated with surfactant, galactose, or denatured albumin (138). Their main disadvantages were their short half-life (few seconds) as a result of the quick diffusion of the air into the blood and the high mechanical index (high acoustic pressure) required to destroy them (139). Their large diameter limited their stay to the venous system, therefore, they cannot cross the pulmonary vascular bed to reach the arterial side.

Second generation:

The second generation (Optison; Molecular Biosystems, Inc, San Diego, CA; or Sonovue; Bracco Diagnostics, Milan, Italy) has a stronger coating and a gas centre of perfluorocarbon, perfluoropropane, or sulphur. These characteristics confer them a longer half-life (about 5 min) and the ability to cross the pulmonary vascular bed, extending the imaging to the main arterial vessels.

Third generation:

The third generation of MBs (EchoGen; Sonus Pharmaceuticals, Bothell, WA; or BR14; Bracco Diagnostics) lasts in the bloodstream for more than 5 minutes. They are also more echogenic owing to the highly compressible gas core (allowing MBs to increase or decrease in size according to the changes in US pressure) and the lower solubility of the gas used compared with air (132, 140).

Microbubble behaviour in US:

MBs exhibit a variety of behaviours when exposed to US waves. They oscillate, scatter the waves, absorb and attenuate them.

Oscillation:

US generates high and low pressure waves at frequencies of 1.5–10 MHz. When US waves hit MBs, they respond with oscillatory movements due to their compression and expansion in tandem with the high and low pressures generated by the US waves hitting them [Fig. 16], The oscillation can be linear or non-linear [Fig. 17], depending on the intensity of the waves, MBs shell and the gas core (74, 75).

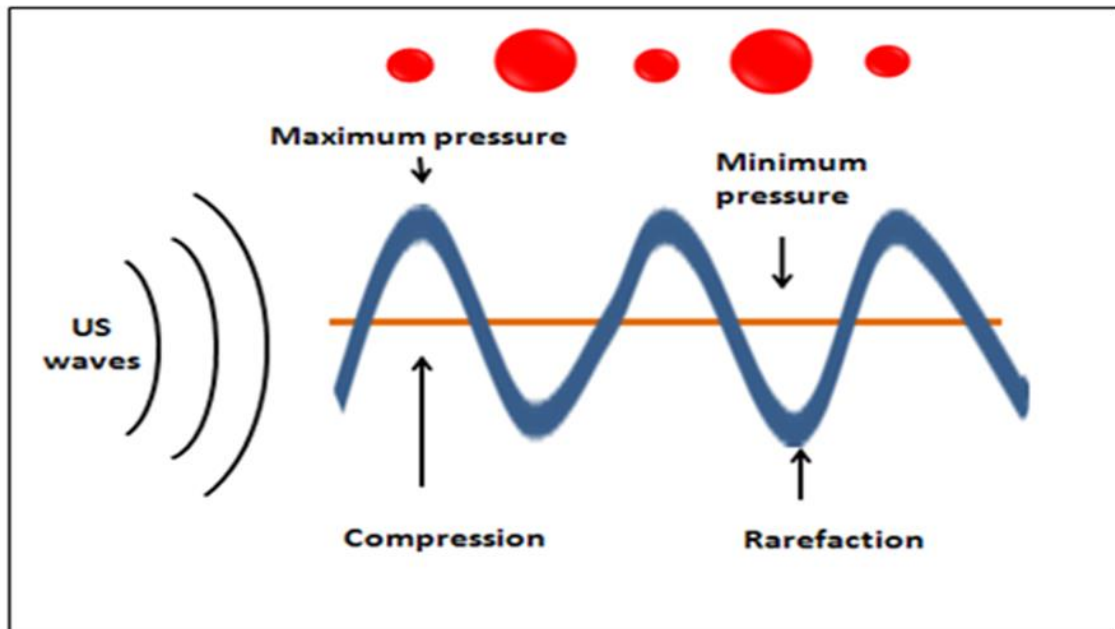


Figure 16. Microbubble compression and expansion on exposure to US waves

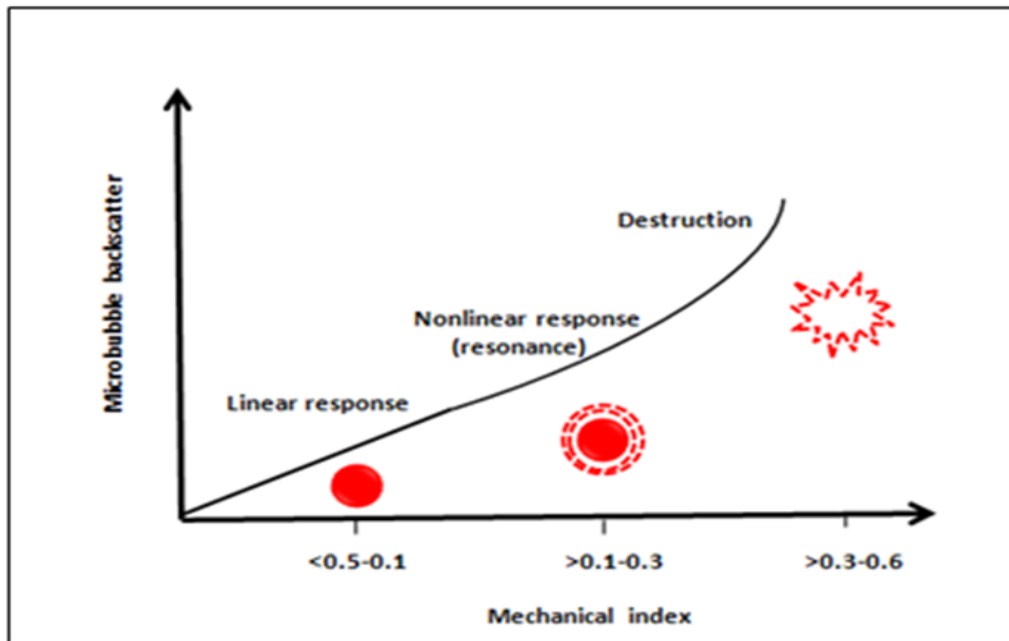


Figure 17. Microbubble behaviour with ultrasound. At low mechanical index; linear oscillation. At intermediate mechanical index; non-linear oscillation. At high mechanical index; microbubbles burst

Absorption:

This phenomenon occurs when the transmitted ultrasound waves are absorbed by the tissues they pass through and converted into heat which might cause thermal damage. This heat is dependent on MBs characteristics and the intensity of the US waves. The heat is also generated from the friction movements of the MBs and the conduction from the compression of the gas core (141).

Scattering:

MBs scattering occurs when a high acoustic pressure is directed upon a boundary. Acoustic pressure is the amount of acoustic energy generated per unit time. This results in compression and expansion of the gas core, causing reflection of signals in all directions (142, 143).

Attenuation:

Is the reduction in the amplitude of the US beam as a function of distance through the imaging medium, and is due to the absorption of the US energy in the form of heat, reflection, refraction and scattering [Fig. 18] (31, 35). Exposure to very low MI makes absorption dominate attenuation because MBs oscillation is still linear, while with low or high MI, scattering dominates this shadowing effect (136).

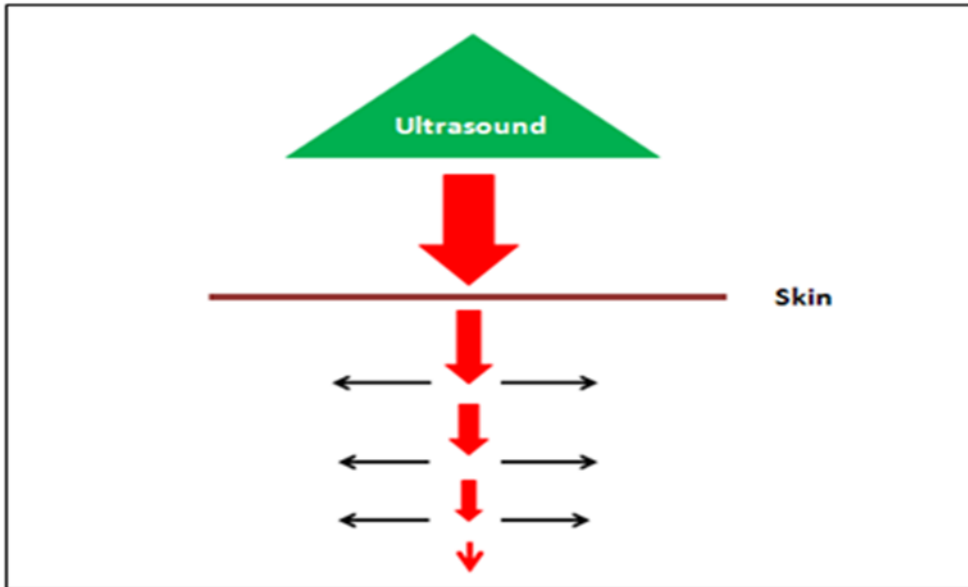


Figure 18. Attenuation

Dissolution:

This phenomenon happens when acoustic pressure is high enough to cause escape of some of the gaseous content from MBs. This behaviour is not strong enough to be used for measuring tissue reperfusion.

Mirror-image:

This effect is caused by reflection and it happens if a reflector at an angle to the US transducer makes any structures that lie in front or to the side of the transducer appear as if they are behind it (the paths to and from a reflector are different) [Fig. 19] (144). It is usually seen when a MB is attached to another MB surface due to the generated radiation force, reflecting energy from the MB (141). This effect can be reduced by changing the angle to the ultrasound probe or patient's position.

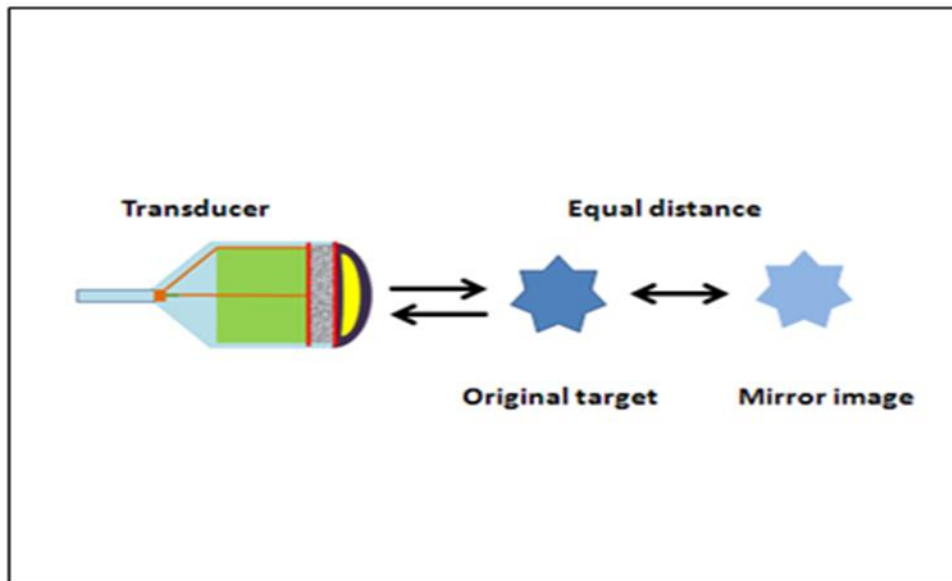


Figure 19. Mirror image

Mechanical index:

The features described above render MBs suitable for use in US imaging (130, 132, 145). For that, consideration is given to the mechanical index (MI) of the US, which is defined as the peak negative pressure (PNP) of the US wave (point of maximal rarefaction) measured in milliPascals divided by the square root of its centre frequency (F_c) [Fig. 20]. MI is a safety metric that must by law be displayed on US machines as it is an estimate of the maximum amplitude of the pressure pulse in tissue and is an indicator of the likelihood of adverse mechanical (i.e. non-thermal) bio-effects such as streaming and cavitation (146).

$$MI = \frac{PNP}{\sqrt{(F_c)}}$$

Figure-20. Mechanical index

Microbubbles' response relative to mechanical index:

On exposure to US waves, MBs respond in three different ways depending on the level of the MI.

Low MI (<0.1):

At this level, the MB response is linear oscillation. This is because the frequency of the reflection wave is equal to the frequency of the transmitted wave. This results in no generated signal as both frequencies nullify each other [Fig. 21A] (142).

Intermediate MI (0.2-0.5):

At this level, the response is non-linear oscillation. This is because the expansion of the MBs is greater than their compression [Fig. 21B]. The result is a harmonic signal at multiples of the transmitted frequency. This characteristic is the keystone for real time imaging (142).

High MI (>0.5):

At this level, the MBs burst [Fig. 21C].

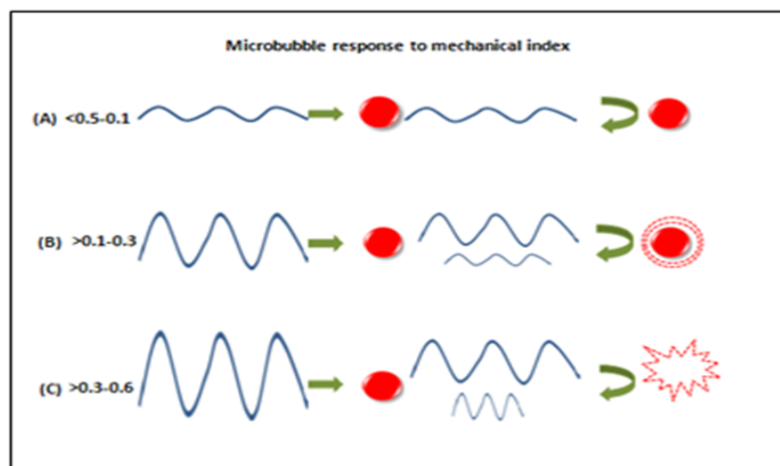


[Figure-21 A, B & C]. Microbubble response relative to mechanical index

Image Enhancement:

To enhance an area of interest, a contrast agent must generate distinctive signals. A variety of techniques are commonly used to achieve that.

Power Modulation:

If a wave is followed by another of the same *shape* but half the amplitude, and the US machine doubles the reflection from the second wave and subtracts it from the reflection of the first, the result is zero due to the *linear* reflection (34)28) if no contrast agent is given. Thus, no signal results. However, intravascular (IV) administration of MBs results in a signal from their characteristically *non-linear* oscillations [Fig-22] generating *backscatter signals* that are detectable as transient contrast enhancement (80). The nonlinear oscillations also nullify linear echoes from surrounding tissues, thereby increasing vascular prominence. The change in the size of MBs and therefore the degree of enhancement depends on the applied frequency (46) which is typically in the 1.5-10MHz range. This technique is called *Power modulation* and allows MBs to highlight areas of tissue perfusion.

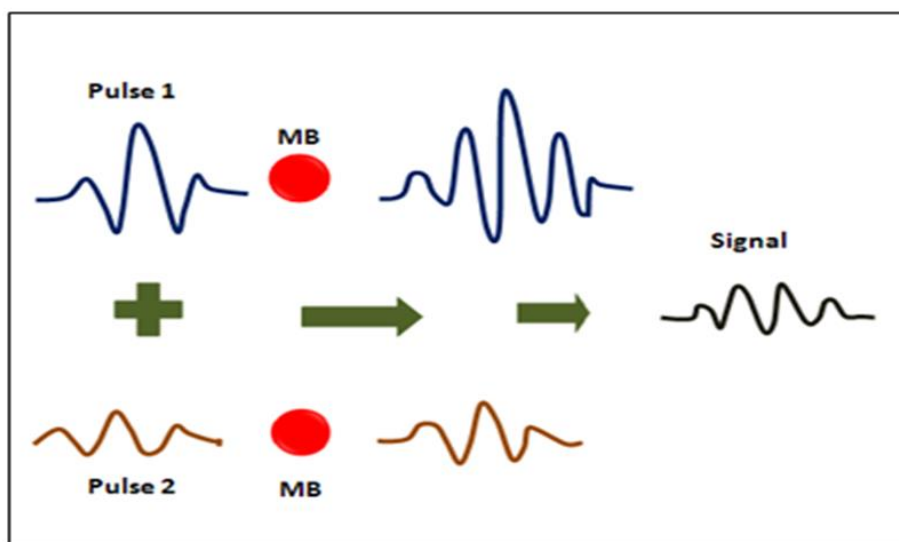


Figure 22. Power modulation technique

Coherent contrast imaging (CCI):

This method is based on the transmission of a single pulse, and the use of multiple beam frames to construct an image. It sums up the inverted echoes from non-linear oscillation of MBs and cancels the linear signals. The advantage of this method is minimal bubble destruction from multiple transmitted pulses.

Real time imaging:

Continuous imaging can be obtained by using a low MI wave to generate signals mainly from MBs with little signal from tissues. The MI can also be suddenly increased to destroy MBs creating a flash effect allowing qualitative and quantitative analysis of MBs and tissue perfusion (34).

Ultraharmonics:

This is the reflected signal by MBs when they are exposed to high MI due to maximum oscillation before they burst. This signal is a characteristic of MBs and not tissues.

Power Doppler Harmonic Imaging (PDHI):

This technique uses a harmonic frequency and displays it in the power mode. It works by sending US waves along a scan line to detect scattering of MBs before they burst, and then another pulse along the same line to detect the shift of scatter effect. The change between the waves is detected as colour and its saturation reflects the amplitude of the echo (147). These techniques offer versatility in the use of MBs in contrast enhanced US (CEUS)

Quantitative versus targeted imaging:

In this technique, MBs are injected into tissues and then quickly destroyed by applying high mechanical indexes. The most common technique used for quantitative imaging is the flash replenishment. The replenishment of MBs in the tissues is then monitored using low mechanical indices and the resulting imaging provides information about tissue perfusion, flow velocity, and vascular volume (148). Targeted imaging can be achieved by either attaching specific ligands to the surface of MBs (i.e., for inflammation, thrombosis, and angiogenesis, see later), or loading MBs with magnetic nanoparticles. In this way, MBs can be guided into the targeted region by applying an external magnetic field (149).

Utility of MBs in CEUS:

MBs as IV contrast agents was first introduced to boost the US signal received from poorly visualized vessels that had low blood flow and thus decreased Doppler signal. They remained in circulation for several minutes after the injection and enhanced the blood signal at a microvascular level (150).

MBs differ from CT or MRI contrast agents in their chemical composition, mechanism of action, and in being completely intravascular contrast agents. In parenchymal organs they provide real dynamic imaging that helps characterize masses according to the 3 phases of perfusion (arterial, parenchymal and venous). They can also be injected several times during an examination and can be cleared quickly from the scanned tissue plane by using high-frequency US waves (138, 151, 152).

Current and potential clinical applications:

Contrast agents have expanded the use of US in a wide spectrum of organs and clinical conditions. CEUS has already been established as a diagnostic modality and it holds promise for further clinical applications. They are neither nephro-, hepato- or cardio-toxic and do not require testing renal function prior to administration (153).

The European Federation of Societies for Ultrasound in Medicine and Biology (EFSUMB) recommend that any CEUS examination should be preceded by careful clinical assessment of the target with conventional B-mode US and, when appropriate, with Doppler and the expected benefits of the CEUS should be explained to patients as part of obtaining consent (154).

Pulmonary:

CEUS is can differentiate between inflammatory and embolic lung consolidation. Due to its dual arterial supply, CEUS can assess the timing and extent of enhancement (155). Lung abscesses within pneumonia may also be identified (154)

Joints:

The degree of vascularization of joints of patients with rheumatoid arthritis can be easily assessed with CEUS. Furthermore, contrast-enhanced Doppler can provide guidance for joint treatment (154)

Hepatic:

In the liver, CEUS imaging has increased the sensitivity of detecting colorectal metastases with reported accuracy as high as 90%, especially for metastases smaller than 10mm (156). This sensitivity is comparable to CT. When Piscala, *et al* (154) compared the US, CEUS and CT in detecting hepatic colorectal metastases, they found that CEUS had a sensitivity of 95.4% compared with 76.9% for US and 90.8% for CT. In a prospective study of 1349 patients with unclear liver lesions, CEUS was shown to be of equal rank to CT with regard to the assessment of tumour differentiation and specification (157). That study suggested that CEUS should be employed before CT to avoid radiation exposure and invasive procedures for biopsies.

Cardiovascular:

CEUS enhances the feasibility, accuracy, and reproducibility of echocardiography for the qualitative and quantitative assessment of the left ventricle structure and function at rest and during stress exercise (158, 159). Cardiac masses can be easily identified, visualization of the right ventricle and great vessels is improved, the evaluation of the valvular function using signals is enhanced and myocardial perfusion can also be assessed (158). Intracardiac thrombi can be assessed in patients with previous myocardial infarctions (159). In their study on 409 patients, Thanigaraj, *et al* (160) demonstrated that ECG failed to detect thrombi in 46% of patients who subsequently underwent CEUS which detected thrombi in 90% of them.

In the intensive care unit, CEUS can overcome some of the obstacles that are regularly faced with transthoracic ECG such as dynamic and complex patient profile, hyperinflated lungs due to mechanical ventilation, subcutaneous emphysema, surgical incisions and chest tubes (158). CEUS increases the visualization of myocardial segments which helps assess the global and regional ventricular functions (158).

Carotid:

In carotid atherosclerosis, CEUS can characterize atherosclerosis plaque, its surface, ulceration and intra-plaque vascularization (159, 161). The carotid lumen and the adventitia layer appear enhanced shortly after injecting contrast agents while the intima-media layers remain hypoechoic. This imaging technique helps depict smaller vessel wall irregularities and hypodense plaques (162). CEUS can also be used to detect hypoechogenic plaque in patients who are at high risk of subclinical atherosclerosis (163) and for analyzing restenosis after carotid stenting (164).

Aortic:

It is known that the diagnostic accuracy of US in ruptured abdominal aortic aneurysm is poor. Using CEUS significantly increases the modality's diagnostic accuracy post rupture and/or leak (161). It shows active extravasation depending pooling of microbubbles within the abdominal cavity or focal area of the aneurysmal wall showing no enhancement due to necrosis. Impending rupture can also be identified during surveillance as CEUS shows decreasing enhancement within the aneurysmal wall.

CEUS is useful in the detection of aorto-caval fistula as it accurately delineates aorto-caval communications with high spatial and temporal resolution in a real-time dynamic investigation (165, 166). An important complication of endovascular aneurysm repair (EVAR), is endoleak. CT angiogram is the gold standard for detecting endoleaks. However, its limitations include radiation, cost and potential contraindications for patients with chronic renal failure (161). CEUS has been shown to be superior to color Doppler US and equivalent or even superior to CT in detecting such complication, especially in type 1 and 2 endoleaks [Table-6] due to its dynamic and real-time pattern of scanning (167-170).

Type	Description
1	1A: blood flow originating from an incomplete proximal attachment of the stent graft to the aortic wall. 1B: blood flow originating from an incomplete distal attachment of the stent graft to the aortic wall.
2	Retrograde blood flow from an anastomotic aortic branch into the aneurysmal sac. 2A if one branch and 2B if multiple arteries are affected. Branches typically affected include the inferior mesenteric and lumbar arteries.
3	Blood flow through a structural discontinuity of the stent graft.
4	Blood flow through porosity of the stent graft.
5	Enlargement of the aneurysmal sac with no evidence of detectable endoleak (also known as endotension).

Table 6. Classification of endoleaks (161).

For the diagnosis of aortic dissection, CEUS is more sensitive than B-mode or Doppler US. After injecting microbubbles, the true and the false lumen are opacified and suspected intimal flaps are visualised, the presence of re-entry-or re-entry points of the false lumen are demonstrated and the true from the false lumen are differentiated based on timing. This is because the false lumen is enhanced later than the true lumen (171, 172). Neovascularization in the inflammatory aneurysm can be visualised by CEUS as it shows moving MB within the wall. This technique is useful in inflammatory conditions such as Takayasu arteritis or giant cell arteritis where initial CEUS shows circumferentially thickened common carotid artery wall containing multiple opacified vasa vasora and subsequent CEUS after treatment showing decreased enhancement of the wall and less vasa vasora (173).

Pancreatic:

CEUS can be used to characterise sonographically detected lesions and can improve the diagnostic accuracy of US in the study of pancreatic pathologies (154). In pancreatic ductal carcinoma, CEUS shows lesion size and margins as well as the relationship with peripancreatic vessels better than conventional US. It can also demonstrate changes in pancreatic tumour vascularization. The differential diagnosis between pseudocysts and cystic tumours is also improved with CEUS as it reveals vascularization of intralesional septa or nodules which characterize mucinous cystic tumour. On the other hand, CEUS does not detect pseudocysts as they are non-vascularized. For pancreatitis, CEUS may help identify and delineate necrotic areas and can also be used for follow up after staging with CT.

Intestinal:

By enhancing bowel wall vascularity, CEUS can be used in the estimation of disease activity in inflammatory bowel disease, differentiate between fibrous and inflammatory strictures in Crohn's disease, characterize abscesses and diagnose and follow the route of fistulae (154)

Splenic:

CEUS can characterise splenic parenchymal inhomogeneity or suspected tumours with 90% sensitivity and 100% specificity when compared with CT. Tumour response to successful chemotherapy can also be monitored due to the lack of enhancement with CEUS. In a retrospective study, Tafuto S, *et al* reported a 38% increase in the detection rate of splenic metastases using CEUS (174).

Renal:

CEUS can be utilized in suspected vascular disorders such as renal artery stenosis, renal infarction and cortical necrosis (154). It can also differentiate between renal tumours and pseudo-tumours, characterize complex cystic masses as benign, follow-up non-surgical complex masses and can also be used to guide renal tumour ablation. There is also a potential use of CEUS in kidney transplant to detect perfusion abnormalities (154).

Infiltration of the muscular layer of the bladder is easily identified with CEUS because it has delayed and less enhancement than mucosa and submucosa which stay enhanced for 1-2 minutes (175). Contrast agents can also be administered via a urinary catheter to evaluate vesico-ureteric reflux and in voiding urosonography. In the scrotum, CEUS can assess the vascularity and of scrotal lesions and cord vessels and may determine the development of an abscess such or increase the sensitivity of detecting epididymo-orchitis (176).

Abdominal trauma:

Solid organ injuries can be ruled out with CEUS in stable patients, especially in children, for the evaluation of uncertain CT findings and for the follow-up of trauma managed conservatively.

In children, CEUS has not been approved by the FDA because contrast agents safety and efficacy have not been established yet. However, the limited literature suggests that CEUS can be useful in children for several reasons. In patients with Kawasaki disease and tetralogy of Fallot, for instance, CEUS can assess endocardial definition (158). In abdominal trauma, CEUS can identify parenchymal injuries better when compared with traditional US. Its performance was also comparable to CT and MRI in detecting benign liver lesions (153).

Biophysical effects of microbubbles:

The addition of MBs into a sonicated medium results in different biophysical effects ranging from sonoporation to permanent cell permeabilization and necrosis, but it is still unknown which effect is dominant (177).

Radiation force:

The translation of MBs in liquids by US waves can create what is called a “bubble bullet” with speed ranging from 5-10cm/s. This is due to the pressure gradient produced by the waves (141).

Streaming:

When MBs oscillate, they create a streamline in the direction of the US waves. Near a vessel wall, these streamlines are asymmetrical and can cause shear stress on the adjacent cell membranes [Fig. 23]. This effect is useful in the local drug transport without creating too much damage to the surrounding tissues (142).

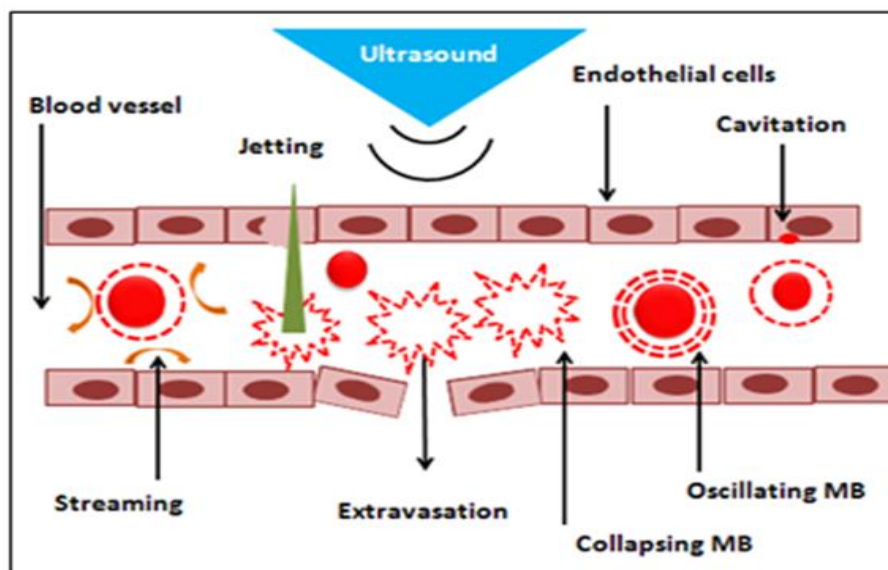


Figure 23. Biophysical effects of microbubbles

Inertial cavitation:

During compression of MBs after a prolonged expansion, a water inrush into the MB centre which results in an inward collapse (implosion) of the MB [Fig. 23]. This behaviour generates shock waves which can be detected as broadband signal on the US machine. The effect could be utilised for local drug or gene delivery to tissues.

Jetting:

At high acoustic pressure, collapsing MBs move in the direction of the US waves producing local mixing through connective processes and water jetting (hammer effect) which is powerful enough to cause damage to a cell membrane [Fig. 23]. This feature has the potential of local drug delivery to targeted tissues (136).

Sonoporation:

Sonoporation is defined as the interaction of ultrasound with MBs causing transient permeabilization of the cell membrane (178). When MBs reach the maximum level of oscillation, they burst causing shock waves. If it happens near a vessel wall, the generated force is strong enough to disrupt cell membrane [Fig. 23]. The addition of MBs reduces US powers to achieve cavitation compared with non-MB-induced cavitation (179). Consequently, MB-induced cavitation is unlikely to produce further damage to the normal tissues surrounding the target area compared with non-MB-induced cavitation unless the surrounding tissues already contain some gas (180). This effect paves the way for drug delivery to targeted tissues.

Fragmentation:

On exposure to high acoustic pressure just above dissolution, MB surface becomes unstable resulting in fragmentation of the bubble into smaller MBs (nuclei) [Fig. 23]. This characteristic has already been implemented in clinical practice to measure tissue reperfusion (142).

Heating:

Heat is generated from the absorbed US waves and the MBs when they collapse or due to the friction with each other or with the surrounding fluid. So far, this effect is thought to be negligible and has not been proven yet.

Free radicals:

The generated heat is thought to lead to the formation of free radicals such as Hydrogen peroxide (H_2O_2) which causes cell damage.

Microbubble safety:

Very few complications have been reported using MBs. These include minor microvascular injuries that might cause local bleeding, allergic reaction (1:10,000), rash or hypotension, mainly in cardiac patients.

Diagnostic applications of MBs:

Enhancement of tissues is determined by the characteristics of both MBs and US and the type of imaging required, whether quantitative or targeted. The best enhancement is achieved with stable outer layers and small diffusion of the gas into the surrounding tissues. This is best seen with lipid-coated MBs (Sonovue; or Definity; Bristol-Myers Squibb Medical Imaging, Inc, New York, NY). Alternatively, albumin-coated MBs (Optison; GE Healthcare, Inc, Princeton, NJ) with a heavy perfluoropropane gas core provide longer enhancements than those with an air centre (Albunex; Mallinckrodt, Inc) (181).

Therapeutic applications of MBs:

The use of MBs as potential therapeutic agents is based on different mechanisms of causing damage to cell wall. With heat enhancement MBs oscillate in a sonicated medium and generate heat as a result of their friction with the surrounding structures and their decompression. The release of heat to the surrounding tissues causes local damage (181). This heat is also useful when gene or drug delivery requires thermal activation. Another mechanism is microjetting. This happens when MBs collapse near blood vessel walls and create microjets travelling toward the cell wall, causing damage to it and enhancing the drug or gene uptake (181). The third mechanism is microstreaming in which MBs vibrate to create acoustic streams around them, again causing damage to cell membranes (182). Chemicals also play an important part. The collapse of MBs & the locally generated heat result in the formation of Oxygen free radicals. These chemicals cause further damage to the cell wall which enhances drug uptake by the cells (183). Finally, MBs can be used as direct vehicles for drug or gene delivery to specific areas through the combination of selective ligands on their surface (targeted MBs).

Targeted microbubbles:

Targeted MBs aim to extend the current indications of nonspecific MBs as US contrast agents (184) by increasing the sensitivity and the specificity for a particular target or deliver specific agents to tissues (i.e., genes or drugs) (185). The targeting process [Fig. 24] can be achieved by coupling antibodies, polysaccharides, and peptides on the MB surface to specific receptors (4, 186) that are expressed during various conditions (i.e., apoptosis active targeting) (96). The antibodies coupled during the active targeting can be directed against molecules specific to inflammation, angiogenesis, thrombi, and cancer (130). Important criteria for the selection of ligands coupled to MBs include reproducibility, minimum ligand waste, firm binding, ability of the ligand to find its target, and minimizing nonspecific binding (145, 187). Other methods of targeting involve the passive diffusion of MBs through abnormally permeable vessels and therefore increased accumulation in tissues according to the size and shell characteristics (i.e., during inflammation passive targeting) (188) or the recognition and phagocytosis of MBs by the reticuloendothelial system (185).

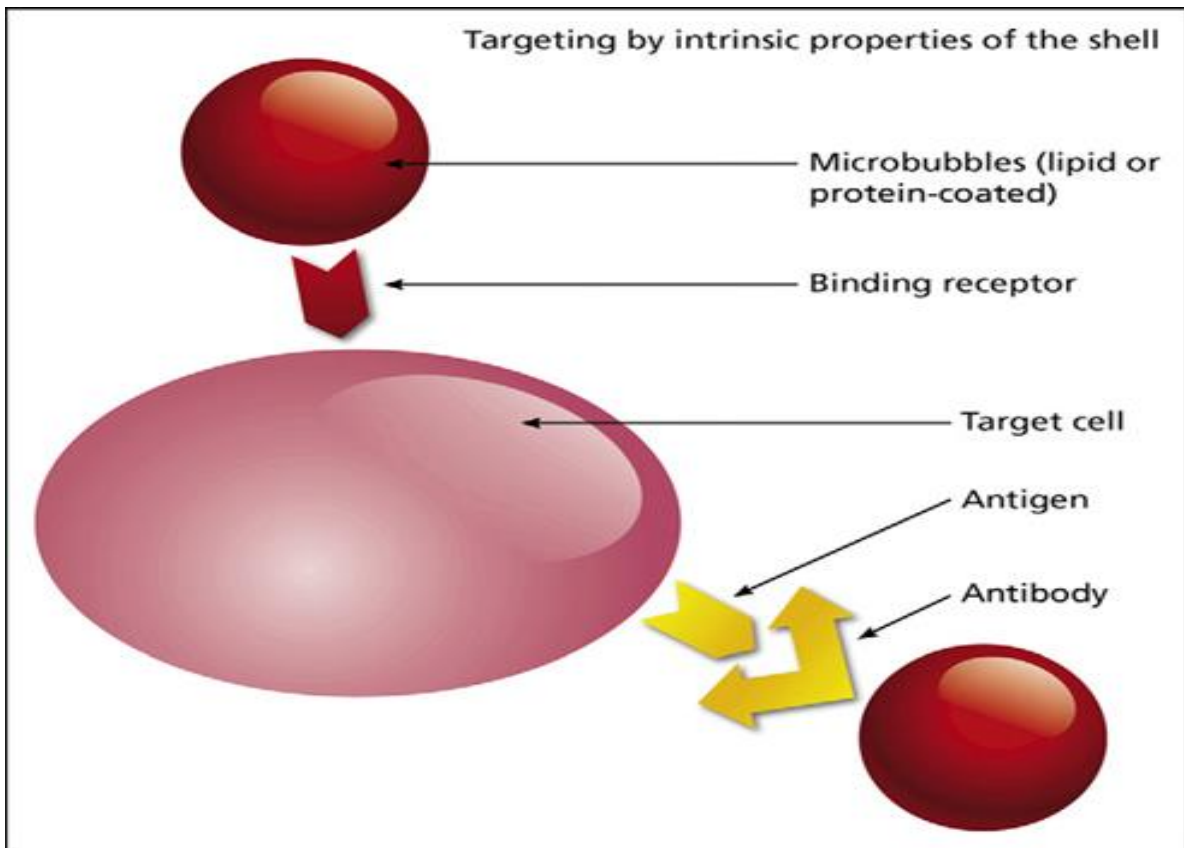


Figure 24. Mechanism of active targeting (lower part of the figure), or targeting by intrinsic properties of the shell (upper part of the figure)

After the injection targeted MBs accumulate at tissue sites and remain in situ for about an hour before they are cleared up from the vascular system (4). They also generate an acoustic response signal that is displayed as a video enhancement on the screen and provide higher sensitivity and specificity than the standard non-targeted MBs (4, 185).

Inflammation:

In inflamed areas leukocytes adhere to the venular endothelial cells in different steps, and specific mediators such as P-selectin trigger this mechanism (99, 100). P-selectin (CD62P) is a 140-kDa protein that is expressed on platelets, endothelial cells, and megakaryocytes. It mediates the adhesion of neutrophils and monocytes to activated platelets and endothelial cells, enhances leukocyte rolling, and is involved in the migration of leukocytes into inflamed tissues. Retained targeted MBs behave similar to leukocytes in inflammation and adhere directly to the endothelium or to the leukocytes to form microbubble–leukocyte complexes (189, 190). Their targeting capability is increased at the venular side owing to the slow flow state present during inflammation (189). This behaviour holds the potential to provide more information about inflammation with targeted CEUS without the need for biopsies or MRI.

Various studies have used targeted MBs to evaluate inflamed tissues [Table-7]. Some have demonstrated an improved US signal as a result of the adhesion of targeted MBs to

leukocytes (5). Others have used different methods to increase MB retention at the inflammatory sites by using wrinkled MBs (52), high acoustic radiation (55), or by targeting P-selectin (186, 191) with RB40.34 antibody. This antibody can block mouse P-selectin binding to its ligands (CD24 and CD162) *in vitro* and *in vivo* (192).

Author	Year	Target	Antigen targeted	Targeting agent	Experimental setting	Microbubbles	Results
Linder (5)	2000	Inflammation	Leukocytes	Phosphatidylserine (PS)	15 mice (cremasteric muscle)	Targeted vs. non-targeted	Greater attachment of PS-MBs to leukocytes, higher US signal after ischemia-reperfusion injury in the kidney
Linder (191)	2001	Inflammation	P-selectin	RB40.34	15 mice (cremasteric muscle)	Targeted vs. non-targeted	Increased MBs retention at venular endothelium
Takalkar (186)	2004	Inflammation	P-selectin	RB40.34	Murine cell line	Targeted vs. non-targeted	Increased MBs retention at higher P-selectin site density
Rychak (4)	2006	Inflammation	P-selectin	RB40.34	4 mice (cremasteric muscle)	Targeted vs. non-targeted	Positive pressure resulted in the formation of wrinkled MBs that had a greater adhesion at venular endothelium vs. spherical MBs
Rychak (193)	2007	Inflammation	P-selectin	RB40.34	14 mice (cremasteric muscle)	Targeted vs. non-targeted	Increased MBs retention in femoral vessels after acoustic radiation
Ellegada (194)	2003	Angiogenesis	$\alpha\beta 3$ Integrin	Echistatin	14 rats (malignant glioma)	Targeted vs. non-targeted	Preferential retention within the tumour microcirculation, higher US signal at the periphery of the tumour
Leong-P	2003	Angiogenesis	αv Integrins	Echistatin	or 10 mice	Targeted vs.	Direct attachment to

(150)				murine anti αv antibody (mAB)	(cremasteric muscle)	non-targeted	vs.	the vascular endothelium
Dayton (130)	2004	Angiogenesis	$\alpha v \beta 3$ Integrin	Biotinylated MAB1979	Endothelial human cell line	Targeted non-targeted	vs.	Targeted MBs adhere to substrate
Korpanty (195)	2007	Angiogenesis	VEGFR2, CD105, VEGF-VEGFR complex	Anti VEGF antibody	15 mice (pancreatic adenocarcinoma)	Targeted non-targeted	vs.	Preferential retention within the tumour microcirculation
Willmann (196)	2008	Angiogenesis	VEGFR2 or $\alpha v \beta 3$ integrin	Anti VEGFR2 antibody and anti $\alpha v \beta 3$ antibody	49 mice (ovarian carcinoma)	Targeted non-targeted	vs.	Direct attachment to the vascular endothelium
Schumann (129)	2002	Thrombosis	GPIIb-IIIa receptors (platelets)	Bioconjugate	6 mice (cremasteric muscle)	Targeted non-targeted	vs.	Higher affinity for platelets in both arteries and veins
Culp (197)	2004	Thrombosis	GPIIb-IIIa receptors (platelets)	Eptifibatide	15 pigs	Targeted alone	vs.	Rapid opening of intracranial thrombosis with targeted MBs. Good safety profile
Alonso (198)	2007	Thrombosis	GPIIb-IIIa receptors (platelets)	Abciximab	Cell line & 19 rats	Targeted non-targeted	vs.	Higher detection of the clots with targeted MBs
Martin (199)	2007	Thrombosis	GPIIb-IIIa receptors (platelets)	Abcimixab	Thrombi generated by a Chandler loop	Targeted non-targeted	vs.	Retention of the targeted MBs on the thrombi
Xie (200)	2009	Thrombosis	G PIIb-IIIa receptors (platelets)		45 pigs/ thrombotic occlusion of the left descending coronary artery	Targeted non-targeted	vs.	Rapid replenishment of the central risk area with targeted MBs Higher recanalization rate with targeted MBs Higher rate of ST

								segment resolution with targeted MBs
Birnbaum (201)	1998	Thrombosis	GPIIb-IIIa receptors (platelets)			13 rabbits thrombosed iliofemoral artery	MBs + US vs MBs alone or US alone	Recanalization of all arteries with MB + US vs MB alone or US alone
Tachibana (202)	1995	Thrombosis	GPIIb-IIIa receptors (platelets)			Thrombi generated by a Chandler loop	Urokinase (UK) vs UK + US vs UK + US + MBs	More fibrinolysis with UK + US + MBs
Feril (14)	2003	Apoptosis	Phosphatidylserine	Annexin V		Human myelomonocytic leukemia cell line	US + MBs vs. US alone	Increased apoptosis and cell lysis with MBs + US
Yu T (15)	2006	Necrosis	-	-		47 rabbits (liver)	MBs + HIFU Vs. HIFU alone	Increased tissue necrosis with MBs
Luo (13)	2007	Apoptosis	Proliferating cell nuclear antigen (PCNA)	Clone PC10 (anti PCNA antibody)		50 rabbits (liver)	MBs + HIFU vs. HIFU alone	Increased apoptosis and proliferation in the MBs group
Furusawa (12)	2009	Apoptosis	-	-		Human myelomonocytic leukaemia cell line	U937 Sonazoid MBs vs. US alone	MBs enhanced Growth Factor withdrawal, DNA damage, unfolding stresses in the Endoplasmic reticulum and Death Receptor stimulation increasing apoptosis
Shohet (203)	2000	Gene delivery	-	Recombinant adenovirus containing β -		36 rats (myocardial cells)	Targeted vs. non-targeted	Expression of β -galactosidase transgene higher with

Ogawa (204)	2002	Gene delivery	-	galactosidase gene Plasmid containing luciferase gene	HeLa cell line	MBs reporter plasmid pGL3	vs.	targeted MBs Increased gene transfer with MBs
Wang (205)	2005	Gene delivery	-	Plasmid containing GFP gene	10 mice (skeletal muscle)	Targeted non-targeted	vs.	Improved gene transfection efficiency
Manome (206)	2005	Gene delivery	-	pCAG-Luc plasmid	Cell line mice brain	MBs + US US alone	vs.	High gene transfection with MBs + US
Tsunoda (207)	2005	Gene delivery	-	Plasmid containing luciferase, β -galactosidase or GFP gene	6 mice (left ventricular cavity)	MBs + US	vs.	High expression of luciferase, β -galactosidase or GFP
Kodama (208)	2006	Gene delivery	-	Plasmid containing luciferase or β -galactosidase gene	Chinese hamster ovary cells expressing human E-selectin	MBs + US crushed heat-treated MBs + US	vs.	High gene transfection with MBs + US
Yamashita (209)	2007	Gene delivery	-	Plasmid containing GFP gene	Rabbit corneal epithelial cells and subconjunctiva	Targeted non-targeted	vs.	In rat eyes, strong GFP staining was seen in conjunctiva with targeted MBs
Wang (210)	2008	Gene delivery	-	Plasmid containing GFP gene	Pancreatic carcinoma cell line	Targeted non-targeted	vs.	Significant enhancement of the receptor gene expression with targeted MBs
Christiansen (211)	2003	Gene delivery	-	Plasmid containing luciferase gene	10 mice & 33 rats (skeletal muscle)	Targeted MBs + US alone	vs. US alone	Greater gene transfection with MBs + US compared to US alone (via intra-arterial injection>intravenous

Bekeredjian (212)	2007	Gene Delivery	-	Plasmid containing luciferase gene	30 (hepatoma)	rates	Targeted MBs + US alone	vs US	injection) Greater gene transfection with MBs + US compared to US alone
Watanabe (213)	2008	Gene delivery	-	Plasmid containing luciferase gene	Prostate cells	cancer	Lipid-coated MBs	vs. non-coated MBs	Higher gene transfer with lipid-coated MBs
Iwanaga (214)	2007	Drug delivery	-	Plasmid containing cdtB	14 mice and tumour cell line (gingival squamous cell carcinoma)		Bleomycin-loaded MBs	vs. non-loaded	Tumour growth inhibition
Chapuis (215)	2009	Drug delivery	-	Biotinylated bleomycin A (5) & non-biotinylated bleomycin	MCF-7 cell line (breast cancer)		Biotinylated bleomycin A (5)-targeted MBs	vs. non-biotinylated targeted MBs	More conjugation of biotinylated bleomycin to cell line with targeted MBs vs non-targeted. No conjugation of the non-biotinylated bleomycin to cell line
Maeda (216)	2009	Drug delivery	EGFR (epidermal growth factor receptor)	Anti EGFR antibody & bleomycin	Ca9-22 cell line (gingival squamous cell carcinoma)		Bleomycin + anti EGFR antibody targeted MBs	vs non-targeted	Tumour growth inhibition with targeted vs non-targeted Surface deformation of Ca9-22 cell line in the presence of antibody
Xing (217)	2008	Drug delivery		VEGF and P53	20 mice (ovarian carcinoma)		Paclitaxel-loaded MBs		Tumour growth inhibition

Liu (218)	2010	Heat shock protein	-	-	25 rabbit livers with ablations. Control group, US group, RF group, CEUS group and CEUS+RF group	vs. non-loaded	Expression of HSP70 in the CEUS, RF and CEUS+RF groups with ablation vs no expression in the control and US group in the tissues with no ablation. Expression of HSP70 in normal liver tissue in the RF and CEUS+RF group
------------------	------	--------------------	---	---	--	----------------	--

Table-7. Experiments with microbubbles. [cdtB = cytolethal distending toxin B]; [EGFR = endothelial growth factor receptor]; [GFP = green fluorescent protein]; [HIFU =high-intensity US-focused ablation]; [PCNA = proliferating cell nuclear antigen]; [UK, urokinase]

Angiogenesis:

Angiogenesis is the formation of new capillaries from pre-existing blood vessels. It may be physiological as part of the normal development of the vascular system e.g. in foetal development, and the menstrual cycle or pathological, e.g. in tumours (219). Angiogenesis plays a major role in tumour growth and metastasis where newly formed vessels express primary stimulant receptors such as $\alpha v\beta 3$ -integrin and vascular endothelial growth factor (VEGF). These receptors interact with the extracellular matrix to help sprout additional vessels from the endothelial cells (220). Targeting these receptors with MBs might help map angiogenesis with CEUS to provide more information about malignancies and their response to treatment.

Different researchers have already shown that the injection of targeted MBs to $\alpha v\beta 3$ and VEGF receptor 2 (VEGFR2) into malignant tissues increased the attachment of the MBs to the vascular endothelium and improved US signals of the tumour's periphery (130, 150, 194, 195) [Table-7]. VEGF is a glycoprotein that serves as a key factor in the homeostasis of vascular endothelial cells (106). Ellegala, *et al* (194) and Leong-Poi *et al* (150) attached an echistatin antibody to MBs to target $\alpha v\beta 3$ and VEGF2. Echistatin is the smallest member of the disintegrin family of snake venom proteins that inhibit cell-cell adhesion (221). Company, *et al* (195) and Willmann, *et al* (196) used anti-VEGF2 antibody (R84). R84 is a selective, fully human monoclonal antibody that blocks the cancer-promoting agent (VEGF) from binding only to VEGF receptor 2 (VEGFR2).

Thrombosis:

Because MBs are mainly intravascular, they require the blood flow to be visualized. This characteristic might contraindicate their use in the absence of blood motion (i.e., a thrombosed vessel) (59). However, enhancement and even lysis of the thrombi can be achieved by using targeted MBs specifically to the clotting site (129, 197, 199-202, 222) [Table-7]. Normally, during vascular damage the platelets aggregate locally followed by the activation of glycoprotein (GP) receptors, such as GPIIb and GPIIIa. These receptors attract more platelet and fibrinogen, resulting in the formation of blood clots (129) Targeting GPIIb and GPIIIa by coupling specific ligands to MBs might increase their avidity for the clotting site, rendering the thrombus visible on US imaging and increasing its fragmentation when applying high frequency US waves as the local MBs would act as wave accumulators (200). Eptifibatide is a cyclic heptapeptide with six amino acids and one mercaptopropionyl (des-amino cysteinyl) residue that has been used for this purpose. It binds to the platelet receptor GPIIb/IIIa of human platelets and inhibits platelet aggregation (223).

Gene delivery:

The currently used methods for gene delivery include viral vectors, non-viral vectors, and electroporation. Their disadvantages are their ability to stimulate the immune system and sometimes the creation of DNA mutations (205). A newly emerging and promising method of gene delivery is the use of MBs with US. This method is based on the sonoporation and cavitation effects of the MBs in a sonicated medium (see earlier) (209, 210). The holes

created in the cell membrane increase its permeability and allow a more efficient delivery of genes into the cell (205, 211). Once the genes are delivered the holes reseal so that cells recover and the transfected genetic material is trapped inside them (224). For gene delivery MBs are not targeted to a specific cell or tissue antigen but carry a peculiar experimental gene that, once transfected, allows the easy detection of the transcribed protein proving that MBs effectively work for this purpose. Other positive benefits derived from the use of US and targeted MBs include an increased membrane fluidity as a result of the changes in the local temperature from the application of US, the generation of intracellular oxygen species, the endocytosis and phagocytosis of targeted MBs, and the fusion of lipid-coated MBs with the phospholipids layer of the cell membrane (225). All these factors positively increase the number of transfected cells. The transfection also might be facilitated by repeated US applications without compromising cell viability (226).

Different experimental studies on animals (203, 205, 207, 211) and on cell lines (204, 206, 208-210, 213) have already shown the promising potential of using MBs and US as a means of gene transfer [Table-7]. In all those studies, the expression of the transfected gene was higher using targeted than non-targeted MBs.

Drug delivery:

There are different ways by which MBs can be used as drug carriers [Table-7]. These possibilities involve attaching the drug to the membrane surrounding the MB with a covalent or non-covalent bonding, embedding the drug within the membrane, loading the bubble with the drug, or attaching pharmaceutical carrier particles (liposomes) to the bubble surface [Fig. 25].

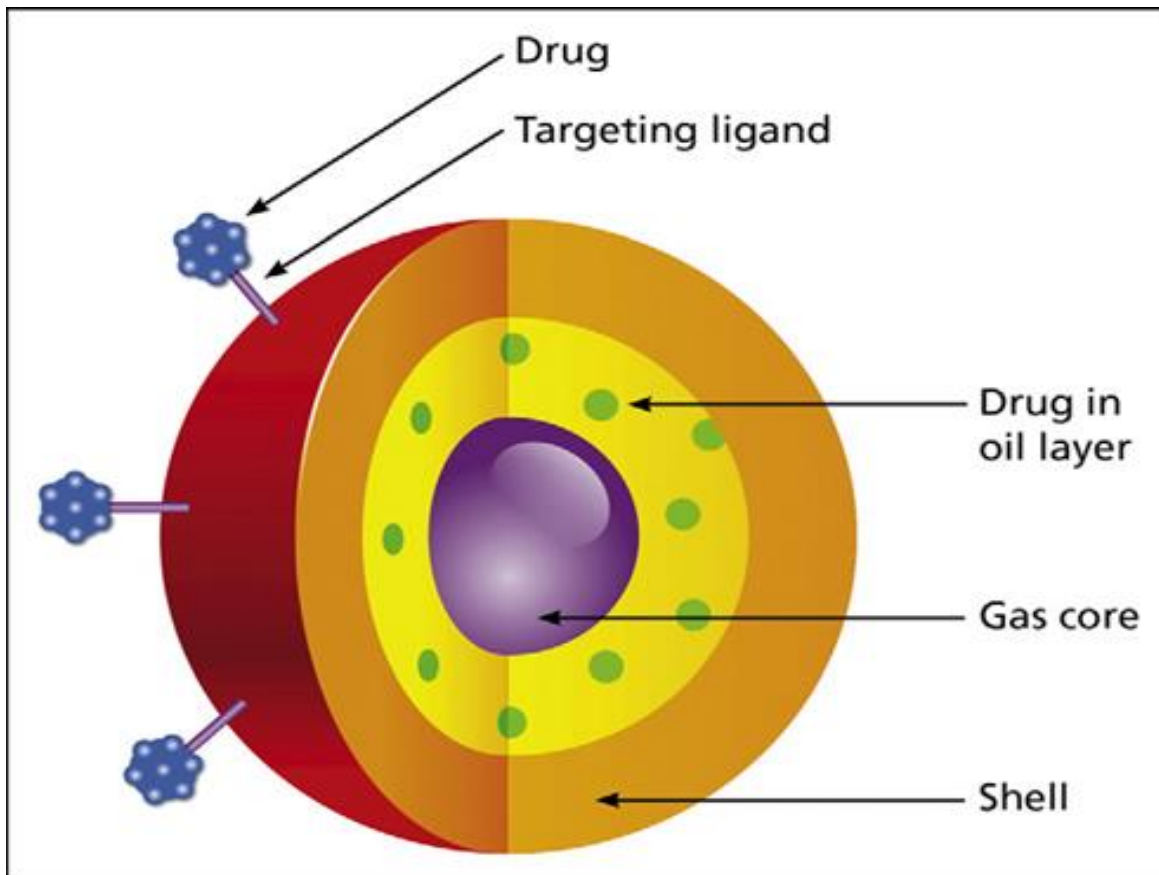


Figure 25. Most common mechanisms of drug delivery using microbubbles

This last method is particularly useful when using large amounts of water-soluble pharmaceutical material (215, 227). Even for drug delivery MBs are not targeted to a particular cell or tissue antigen but carry a peculiar drug. On applying US waves, drug-loaded MBs oscillate, creating shock waves and microjets around them and allowing the drug transport through the cell membrane (228). The efficiency of the drug delivery mechanism with US contrast agents depends on the density of the contrast agent, the acoustic window of the transducer to the target site, and the composition of the interstitial space in the organ (229). Drug delivery via MBs has several advantages. First; it protects the inactivation of the therapeutic agent or its removal from the circulation. Second; it reduces systemic side effects of the agent. Third; it facilitates the transvascular or intracellular deposition of the agent. Fourth; it provides a method to further improve the site-specific delivery of the agent to the diseased area only (216, 230). Furthermore, MB-loaded drug delivery is superior to radioimmunoconjugates (antibodies attached to radionuclides). With the former the drug is released at the selected disease site after applying US waves, whereas with the latter the long serum half-life of the antibodies prolongs radiation exposure to normal organs, which limits the radiation dose that can be administered safely (231). Examples of conditions in which sustained release of local therapeutic concentrations of a drug would be useful include restenosis of blood vessels, angiogenesis (i.e., tumour microcirculation), solid tumours (i.e.,

specific release of chemotherapeutic agents), and inflammation. Tumour growth inhibition has already been shown in a few experiments (214-217) [Table-7].

Heat shock proteins:

Heat shock proteins (HSPs) are present in all cells but their production is increased, especially when tissues are exposed to stressful conditions such as heat, cold, ischemia and reperfusion, heavy metals, infection, high calcium level, cancer, inflammation, and tissue damage (218, 232-234). The main functions of HSPs include chaperoning protein transport by folding damaged or newly synthesized protein into shape, prevention of protein aggregation under physical stress, and triggering the immune response (234). Because HSPs are mainly intracellular proteins, they bind with other intracellular proteins to form peptide complexes that are released on the cell surface. The high expression of HSPs in the transitional zone after radiofrequency ablation of liver cancers makes the partially damaged cells in that zone more susceptible to cytotoxic cellular killing (232). Preventing HSP expression in the ablated tumours would aid killing viable cancer cells in the transitional zone. In their study, Liu *et al*, (218) showed an increased expression of HSP70 in the livers of 25 rabbits after ablation using targeted MBs and US compared with US alone [Table-7].

Apoptosis:

Apoptosis is the process of programmed cell death that plays a critical role in controlling cell numbers and proliferation during tissue growth (8, 9). It may be activated by different stimuli but the final target is the cleavage and destruction of the DNA by the activation of a series of proteases called Caspases. On histology, apoptosis is manifested by nuclear chromatin condensation, fragmentation, membrane blebbing, and cell shrinkage (10, 11).

Recent experimental studies have shown that apoptosis can be enhanced by applying US waves and MBs [Table-7] (12-15). This is based on the suggested mechanism of the inertial collapse of MBs after applying US waves, in which the resultant MB fragments act as cavitation nuclei, thereby creating holes in the adjacent cell membranes and causing cell death (235). Also in this way, MBs can target intracellular antigens and deliver selective antibodies against nuclear antigens (i.e., proliferating cell nuclear antigen) (13). MBs have been shown to improve physiological regeneration in the areas surrounding damaged tissues. In an experimental animal study on rabbits, Luo *et al* (13) showed an increase of liver apoptosis and cell proliferation in zones surrounding necrotic areas when high frequency US was combined with MBs. This dual action could be used as a means of enhancing the damage in a targeted area (i.e., liver ablation therapy) and to encourage regeneration of healthy tissue around it.

Chapter Two

Contrast-enhanced ultrasound detects perfusion defects in an ex vivo porcine liver model: a useful tool for the study of hepatic reperfusion

Abstract:

Background:

Following transplantation, areas of hypoperfusion can be associated with metabolic changes and poor organ recovery. In recent years, the HPB department has gained considerable experience with the use of hepatic ex vivo organ perfusions. This study evaluated the use of contrast-enhanced ultrasound (CEUS) in the detection of such areas.

Method:

Livers were collected from ten pigs, connected to extracorporeal circuits and perfused using autologous blood. After 1h and 4h, livers were scanned with an ultrasound machine following the administration of contrast agents. Biopsies from perfused and non-perfused areas were collected.

Results:

The entire parenchyma enhanced strongly on non-contrast ultrasound at 1h with no perfusion defects. Four hours later, multiple perfusion defects manifested not evident with non-contrast ultrasound. Histology confirmed that the non-perfused areas corresponded to ischemic zones.

Conclusion:

In this model, the addition of CEUS revealed perfusion defects after 4h. This might facilitate detection and characterization of perfusion defects in transplanted livers.

Introduction:

Ischaemia-reperfusion injury:

Ischemia-reperfusion injury (IRI) is an important pathological process in acute vascular syndromes including myocardial infarction, stroke, cardiac surgery, and organ transplantation, such as kidney and liver (236). It results from interruption of blood flow to an organ and then subsequently restored (237). This process can trigger an acute inflammatory response leading to significant tissue damage and organ dysfunction locally and remotely (237, 238)).

Cellular changes in hypoxia:

The initial developments during hypoxia include formation of cell membrane protrusions, known as blebs, swelling of mitochondria and cisternae dilatation of the endoplasmic reticulum (ER). These changes are reversible and once oxygenation to the cell is restored, full recovery is possible. However, if the membrane protrusions burst, the hypoxia has reached an irreversible stage. The subsequent stages are characteristic of necrotic cell death. There is dysfunction of plasma membrane permeability, loss of ionic gradients and release of intracellular structures (239).

Hepatic ischaemia-reperfusion injury:

IRI of the liver can be categorised into either warm or cold. Warm IRI involves transplantation, liver surgery, trauma and shock. Cold IRI takes place during organ preservation prior to transplantation (240). It represents a big challenge in surgery after liver resection, trauma and transplant as it is the major cause of morbidity and mortality. Hepatic IRI occurs in two phases: the acute (early) injury phase occurring within 1-6 hours after reperfusion, and the subacute (late) phase that peaks at 9-24 hours after reperfusion (237, 238). The hepatic damage is usually measured by serum parameters of hepatocellular integrity, such as: liver enzymes, e.g., Alanine transaminase (ALT), liver synthesis capacity (e.g., by determination of the international normalized ratio of prothrombin time), and liver secretory functions (glucuronated bilirubin) (241). The problem with this method is that liver enzymes decrease over time while necrotic volume increases. Furthermore, these parameters lack the 3-D information provided by the CT on the spatial distribution of liver injury which, together with results of laboratory tests, may provide an important basis for decision making on subsequent surgical interventions (241).

During the reperfusion of ischaemic tissue, formation of reactive oxygen species (ROS) contributes to tissue injury. These include hydrogen peroxide, superoxide and hydroxyl radicals. During hepatic ischaemia reperfusion injury, Kupffer cell activation generates ROS, pro-inflammatory cytokines, chemokines and other mediators, all contributing to ischaemic tissue injury. Mediators, including endothelin-1, enable small vessel constriction, prolonging some parts of hepatic tissue to further ischaemia even once re-perfused (192, 193). In the post-ischaemic liver, these mediators enable infiltration of neutrophils, which in turn produce more ROS, thus creating a vicious cycle of hepatic injury (20, 54, 59, 60). The inflammatory response and microcirculatory dysfunction (132, 242, 243) are the initial steps of the process leading to systemic inflammatory response syndrome and multi-organ failure (61).

Radiological quantification:

Different imaging techniques have been used to detect ischaemic areas post-transplant or resection, such as: CT, contrast-enhanced dynamic magnetic resonance imaging (dMRI), laser Doppler flowmetry (LDF; hepatic artery/portal vein) and thermal diffusion (TD), and Doppler US (97). Radiological quantification of tissue perfusion in transplanted livers is usually done preoperatively by CT, LDF and postoperatively by color-coded duplex US or TD. The disadvantages of some of these techniques include exposure to radiation, side

effects to the injected contrasts, costs, time, and complications of invasive techniques [Table-8] (81). Compared to classic methods of evaluating liver perfusion, CEUS has the advantages of being non- invasive, portable and economical technique that involves no radiation. The possibility of measuring flows of the hepatic artery, portal vein and branches also add to the data already provided.

Method	Morphology of perfusion defect	Advantages	Disadvantages
Plain CT	Triangular or wedge-shaped areas of low attenuation (240)	-	Radiation
Contrast-enhanced CT	Triangular, wedge-shaped or irregular appearance, homogeneous attenuation (240)	Differentiate among arterial, portal and parenchymal phases (parenchymal enhancement is resolved into arterial and portal venous components) (241), high-spatial-resolution and high temporal-resolution whole-liver perfusion imaging (241)	Radiation
Plain MRI	Iso-intensity on T1- and T2-weighted images (240)	No radiation	Need for faster and higher-resolution of whole-liver imaging (241)
Contrast-enhanced MRI	Homogeneous attenuation of signal (240)	No radiation	Need for faster and higher-resolution of whole-liver imaging and improvement in quantification of tissue contrast concentrations (241)
Angiography	Non-opacification of portal vein or wedge-shaped segmental staining in arterial and parenchymal phases on hepatic angiograms (240)	Clear visualization of vessels	Invasive, radiation
US Doppler	Absence of Doppler signal	Non-invasive, portable, economic, no radiation, flow measurements in the hepatic artery and portal vein may be readily obtained (241)	Intra- and interobserver variability, inability to gain regional parenchymal flow measurements (241)
CEUS	Hypoechoic areas	Non-invasive, portable, no radiation. Enhanced visualization of perfusion	Intra and interobserver variability

Table 8. Comparison of contrast-enhanced ultrasound (CEUS) with other methods to evaluate liver perfusion defects. [CT = computed tomography, MRI = magnetic resonance imaging, US = ultrasound]

Porcine livers:

Ten white Landrace Cross pigs (45–60 kg) were used for this part. They were humanely sacrificed in accordance with Home Office regulations and the autologous blood was collected into a container with 5,000 units of heparin. The livers were retrieved according to the technique previously described (244), and 2L of cold Soltran solution (Baxter Healthcare, Thetford, UK) were perfused, 1L into the portal vein (PV) and 1L into the hepatic artery (HA). After the cold perfusion, the livers were transported on ice to the laboratory.

Circuit preparation:

The autologous heparinised blood was used to prime the circuit during the backbench preparation. Cannulation of the portal vein (PV), hepatic artery (HA), bile duct, supra- and infra-hepatic inferior vena cava (IVC) was carried out during the priming. Before connecting the liver to the circuit, 1liter of 0.9 % normal saline solution (Baxter Healthcare, Thetford, UK) was perfused through the PV and HA to flush out the Soltran solution and remove air from the organ and cannulae.

Perfusion:

The extracorporeal circuit [Fig. 27] consists of an automatic centrifugal pump which provided the hepatic arterial flow and pressure, an oxygenator, a heat exchanger unit and a blood reservoir to simulate the venous flow and pressure. The venous blood was collected from the supra and infra-hepatic IVC and returned to the centrifugal pump. Parenteral nutrition, vasodilating prostacyclins, sodium bicarbonate, sodium taurocholate and insulin were added to the circulation to optimise the physiological condition of the system with dosages and rates of infusions similar to the previous protocols (68). Perfusion was carried out for 6h and haemodynamic parameters (HA and PV pressures and flows) were recorded hourly.



Figure 27. Perfusion during an experiment

Blood samples:

Arterial and venous blood samples for gas analysis were collected immediately after the reperfusion and hourly until the sixth hour [Table-9]. Liver viability was measured using the hourly bile production rate, the arteriovenous (AV) oxygen and carbon dioxide differences, and the hepatic metabolic rate for oxygen values (HMRO). The AV oxygen and carbon dioxide differences were calculated from the arterial blood gases. HMRO was calculated by adapting the formula for the cerebral metabolic rate for oxygen: $HMRO = (AV \text{ difference for oxygen} \times \text{hepatic blood flow}) / \text{liver weight}$ (245).

Hour of perfusion	HA pressure (mmHg)	HA flow (l/min)	PV pressure (mmHg)	PV flow (l/min)	Bile production (ml/h)	AV O2 difference (mmHg)	AV CO2 difference (mmHg)	HMRO (mmHg 9 ml/g/min)
0	89 ± 5	0.21 ± 0.11	28 ± 13	0.73 ± 0.42	0	263 (222–412)	8 (5–14)	41 (24–106)
1	87 ± 4	0.34 ± 0.18	27 ± 6	0.73 ± 0.49	8 (2–16)	285 (203–334)	7 (3–16)	44 (35–141)
2	86 ± 4	0.34 ± 0.17	31 ± 13	0.86 ± 0.28	15 (7–34)	281 (144–386)	8 (2–10)	43 (34–109)
3	82 ± 13	0.30 ± 0.16	29 ± 14	0.95 ± 0.27	11 (9–17)	260 (222–409)	7 (1–10)	44 (23–88)
4	87 ± 4	0.26 ± 0.11	27 ± 12	0.94 ± 0.23	13 (7–17)	276 (193–318)	7 (4–12)	46 (28–83)
5	85 ± 3	0.29 ± 0.09	22 ± 10	1.10 ± 0.13	14 (9–22)	241 (208–288)	8 (6–9)	39 (26–62)
6	83 ± 4	0.30 ± 0.10	22 ± 11	1.10 ± 0.09	12 (7–22)	274 (154–280)	8 (5–12)	39 (29–48)

Table 9. Physiological parameters of perfusion and liver viability overtime. [HA = Hepatic artery], [PV = portal vein], [AV = arteriovenous], [O2 = oxygen] , [CO2 = carbon dioxide], [HMRO = hepatic metabolic rate of oxygen]

Ultrasound scanning:

Ultrasound baseline images were saved immediately after reperfusion [Fig. 28].

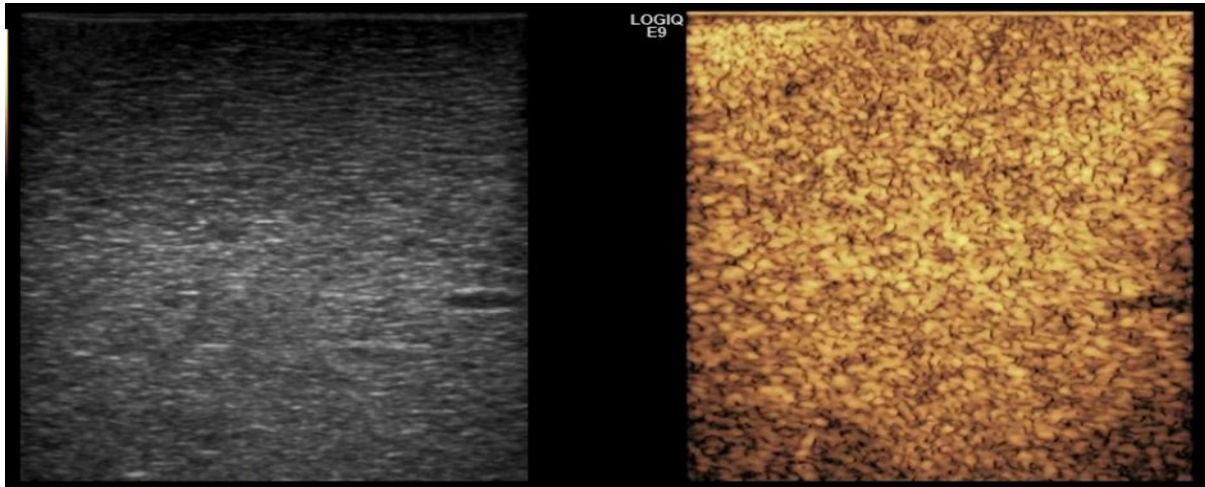


Figure 28. Baseline ultrasound image immediately after reperfusion, without microbubbles (RT panel) and with microbubbles (LT panel). CEUS shows relatively uniform echogenicity through the whole specimen

After 1h from reperfusion, 2.2ml of contrast solution were injected into the valve connected to the portal vein. This was selected due to its higher flow compared to the hepatic artery. The CA (Sonovue, Bracco, Milano, Italy) consisted of phospholipid-stabilized MBs containing Sulphur hexafluoride gas with a diameter of less than 8 μm (mean 2.5 μm) reconstituted with 5ml of a 0.9 % normal saline solution. The whole liver was then scanned again [Fig.29] with a LOGIQ 7 US machine (GE Healthcare, Chalfont St Giles, UK).

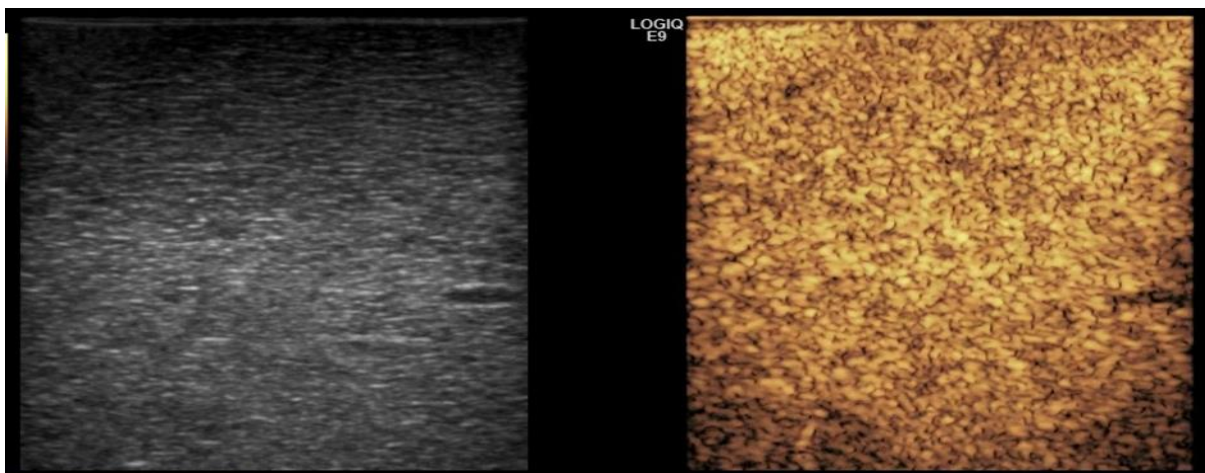


Figure 29. An example of the liver tissue one hour after reperfusion without microbubbles (LT) and with microbubbles (RT). CEUS shows relatively uniform echogenicity through the whole specimen

A specific contrast software was incorporated to create “wash-in”/“wash-out” curves, a measure of the contrast acquisition and removal in a particular scanned area, evidenced during the imaging acquisition and processing. The software provided real-time images with and without the presence of contrast, and the intensity of the acoustic signal was assessed on the video recording extracted every 5s following injection. Standardized 12mm-18-mm regions of interest were chosen for analysis from hyperechoic, hypoechoic, and anechoic areas [Fig. 30].

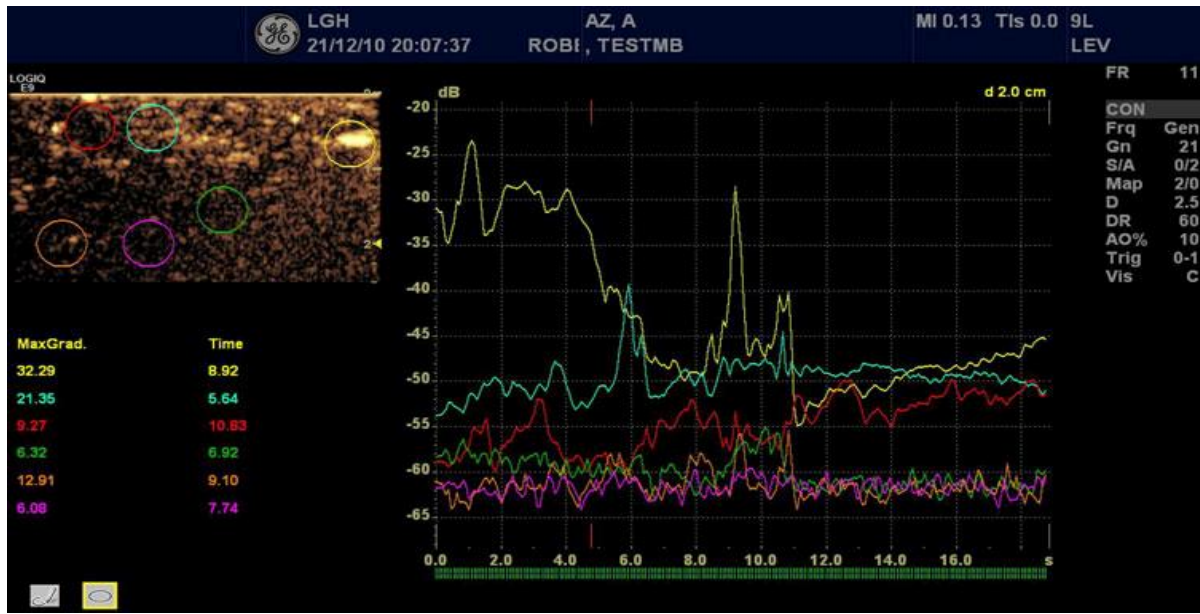


Figure 30. An example of data gathering during one experiment including different time–intensity curves. “Wash out” curves (yellow) correspond to areas of normal perfusion and contrast acquisition (yellow circle), delayed “wash-in” curves with small gradients (red, blue) correspond to ischemic areas and flat curves (purple, orange) to non-perfused areas. The coloured circles in the left upper panel represent the regions of interest (12–18 mm) where data were sampled during the contrast administration (colour figure online)

The following settings were used: integrated mode and gain controls, coded phase inversion (ICC 3, 4), low mechanical index (MI: 0.1) using true agent detection in dual view (contrast-specific sonographic mode) and dynamic range of 72dB. A convex transducer with a 2–5 MHz frequency was used. With every contrast injection, cine loops were recorded for 220 s. No artificial destruction of the MBs was performed but they were let to burst automatically (half-life = 7 min). The whole sequence of contrast and non-contrast-enhanced images was also repeated at 4h post-reperfusion.

Parameters evaluated from the time–intensity curves were common to perfusion imaging techniques (i.e. CT and MRI) and are all indirect measures of the perfusion in a selected region. These were the “time to peak” (time elapsed from the start of the scan to the

maximum intensity of the medium contrast in a defined region, evaluating how quickly the medium contrast peaks in that region), “maximum gradient” (maximum difference between the lowest and highest values recorded of the medium contrast intensity from the start to the end of the scan, evaluating the net increase of contrast reaching that region), and the “area under the curve” (the area under the actual time– intensity curve of the medium contrast, a measure of the total amount of contrast reaching the area over the scan).

Histological examination:

Control random liver samples were taken immediately after slaughtering the pigs, after dissection of the liver, and after connecting the liver into the circuit. At both time points (first and fourth post-reperfusion hours), Tru-Cut biopsies of perfused and non-perfused areas were collected under US guidance with contrast enhancement (perfused and non-perfused areas were not visible without CEUS) and analysed with standard Haematoxylin–Eosin (HE) stain. Histological assessment of the extent of liver injury was performed with Suzuki classification in which grade 0-4 is for sinusoidal congestion, hepatocyte necrosis and ballooning degeneration [Table-10].

Numerical assessment	Sinusoidal congestion	Vacuolation/ ballooning	Necrosis
0	None	None	None
1	Minimal	Minimal	Single cell
2	Mild	Mild	<30%
3	Moderate	Moderate	30%-60%
4	Severe	Severe	>60%

Table 10. Suzuki classification for the histological assessment of the extent of liver injury

Statistical analysis:

All data were initially entered into an Excel database (Microsoft, Redmond, Washington, USA) and the analysis was performed using the Statistical Package for the Social Sciences, Windows version 13.0 (SPSS, Chicago, IL, USA). Descriptive statistics consisted of the mean and standard deviation for parametric distributions and median and range for non-parametric distributions after confirmation with the Kolmogorov–Smirnov test and histograms. Comparisons over time of the hemodynamic parameters (HA and PV pressures and flows) and the production of bile were performed with the ANOVA test for repeated measures. Comparison among enhanced and non-enhanced images was performed with the Mann–Whitney. A p value of <0.05 was considered statistically significant.

Results:

Physiological parameters:

The mean liver weight was $1,659 \pm 372$ g, warm ischemia time 19 ± 2 min, cold ischemia time was 162 ± 24 min. The measurement of the hepatic artery and portal venous pressures and flows during the experiments did not show significant differences over the hours. Similar results were obtained for the AV difference of O₂ and CO₂ and the HMRO (ANOVA test for repeated measures, *p* = non-significant). On the other hand, the production of bile started at 1 h

of perfusion and increased significantly until 2h, when it reached a steady production throughout the rest of the experiment (ANOVA test for repeated measures, $p < 0.001$).

Macroscopic appearance:

Ischemic patchy areas were present in the ex vivo liver model at the time of reperfusion but progressively disappeared after few minutes, and a normal appearance was present throughout the rest of the experiment [Fig. 31].

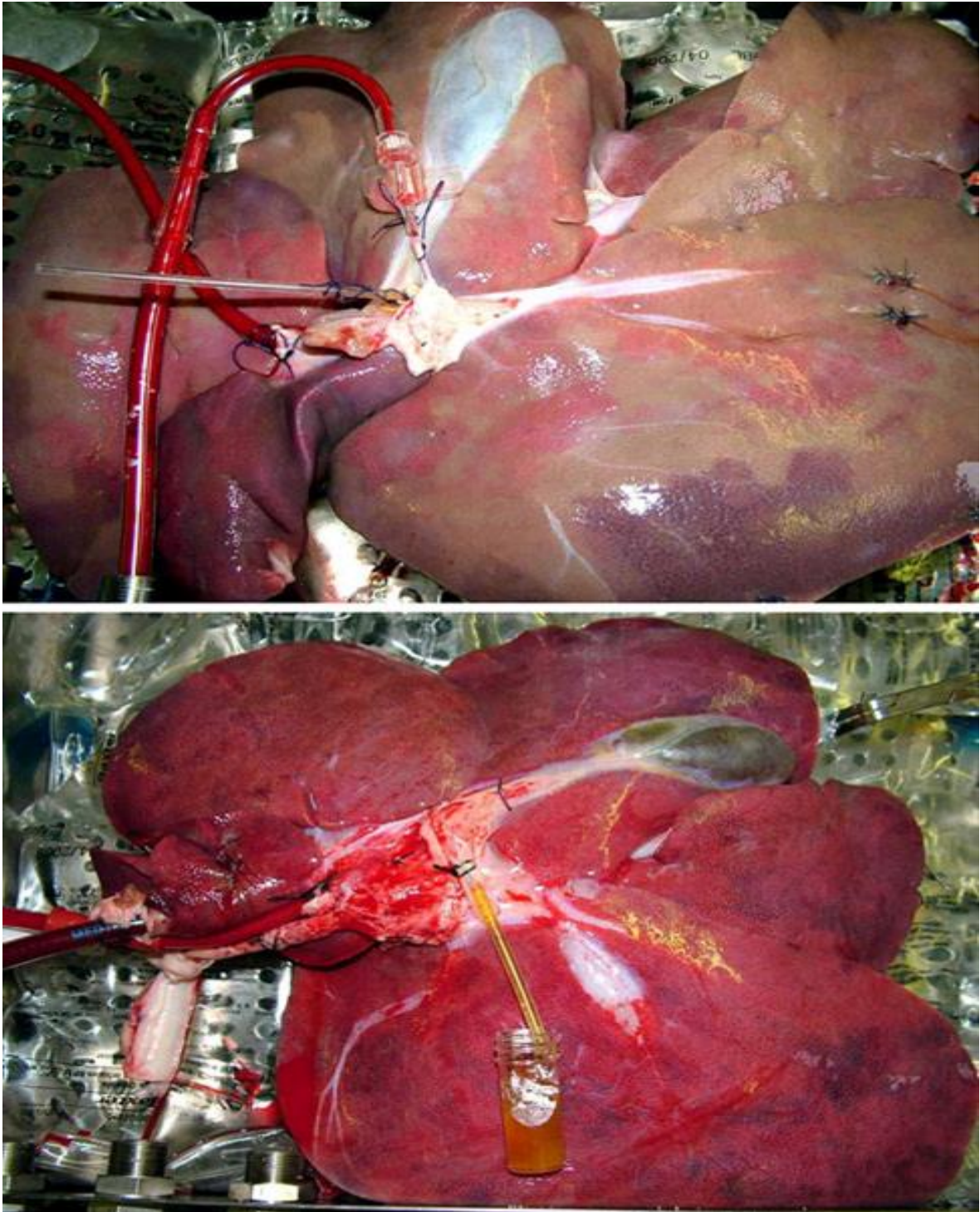


Figure 31. The macroscopic appearance of the liver immediately after connection to the circuit consists of patchy areas of perfusion (upper panel). These progressively disappear from half-an-hour onwards. At the fourth hour the liver is apparently homogeneously perfused (lower panel)

Tissue enhancement:

One hour after commencing the reperfusion of the liver, the entire parenchyma enhanced strongly on non-contrast ultrasound and no perfusion defects were evident on CEUS [Fig. 32].

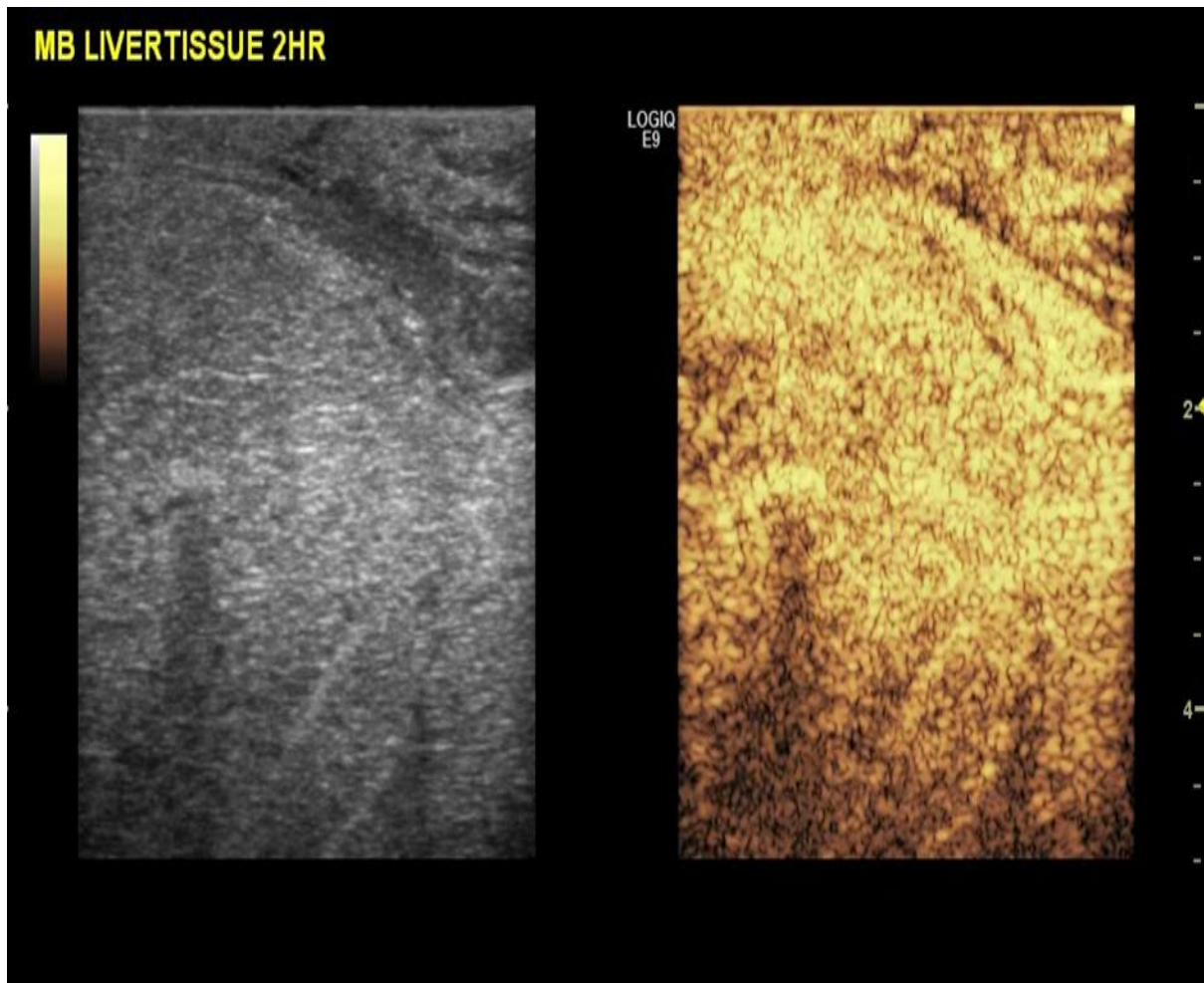


Figure 32. Contrast-enhanced (right) and corresponding non-contrast enhanced (left) images of the same hepatic lobe at the first hour of reperfusion. The entire parenchyma enhanced strongly and uniformly with and without the contrast-enhanced ultrasound.

Four hours later, multiple perfusion defects appeared on CEUS not evident with non-contrast ultra- sound [Fig.33].

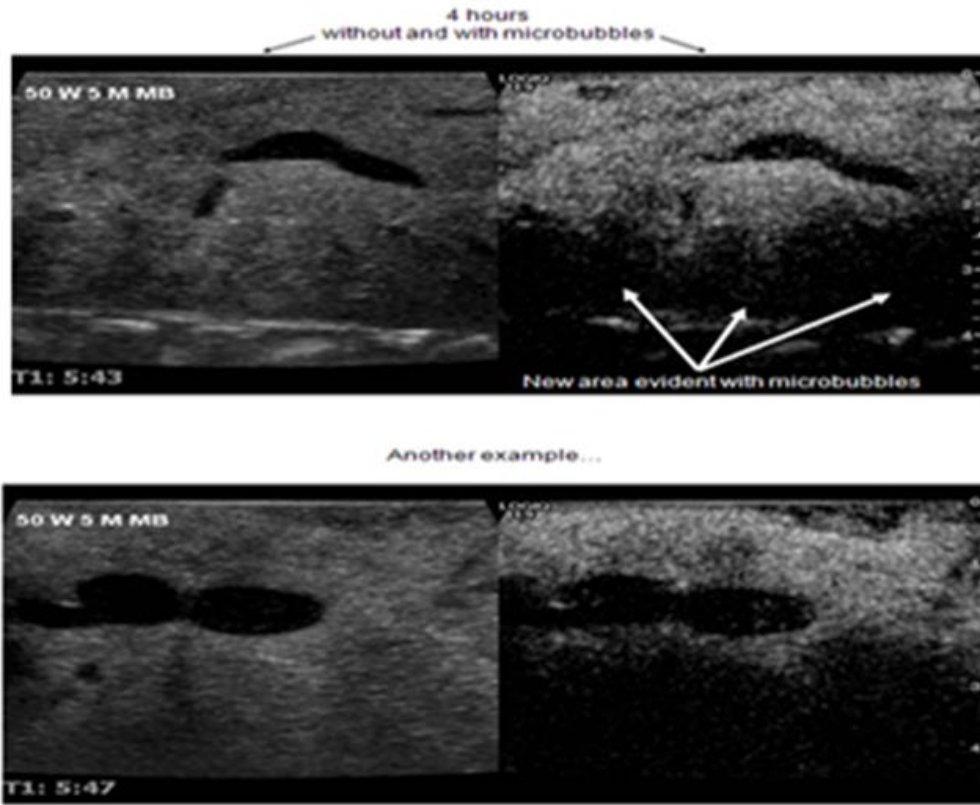


Figure 33. An example of the liver segment after MB injection at 4hr shows good enhancement of the part close to the surface but poor at the mid and deeper zones extending from 4cm deep. Upper and middle panels show “dual view” of vascularized parenchyma and hypovascular areas, with the optimization of the demarcation points by means of “contrast tissue hybrid” application. Contrast-enhanced (right panels) and corresponding non-contrast enhanced (left panels) images of two different lobes from the same liver at the fourth hour of reperfusion. Hypoechoic areas (white arrows in the right panels) correspond to non-perfused zones as evidenced by contrast-enhanced ultrasound. Such areas were not evidenced by non-contrast enhanced images (left panels). Asterisks (white in the left panels, black in the right panels) are close to well-defined, oval areas that correspond to branches of the hepatic veins.

Compared to normal “wash-in” and “wash- out” contrast curves that corresponded to areas of normal perfusion (hyperechoic), delayed “wash-in” contrast curves with small gradients were recorded from areas with decreased perfusion (delayed and reduced acquisition of contrast—hypoechoic) and flat contrast curves were recorded from non-perfused areas (no acquisition of contrast, absence of “wash-in” and “wash-out”—anechoic). The time to peak was significantly longer in the non-enhanced group of images vs. the enhanced (42 s, range

1–146 vs. 21 s, range 1–183; $p < 0.05$). The curve gradient and the area under the curve had lower values in non-enhanced images compared to enhanced (13, range 2–52 vs. 27, range 3–79; $p < 0.005$ and 194, range 7–1,644 vs. 568, range 17–2,432; $p < 0.05$).

Histology:

Analysis of the biopsies before liver dissection [Fig. 34], after dissection [Fig. 35], after connection of the liver to the circuit [Fig. 36] and 1h after commencement of the perfusion [Fig. 37] revealed normal liver parenchymal tissue perfusion with no signs of ischaemia.

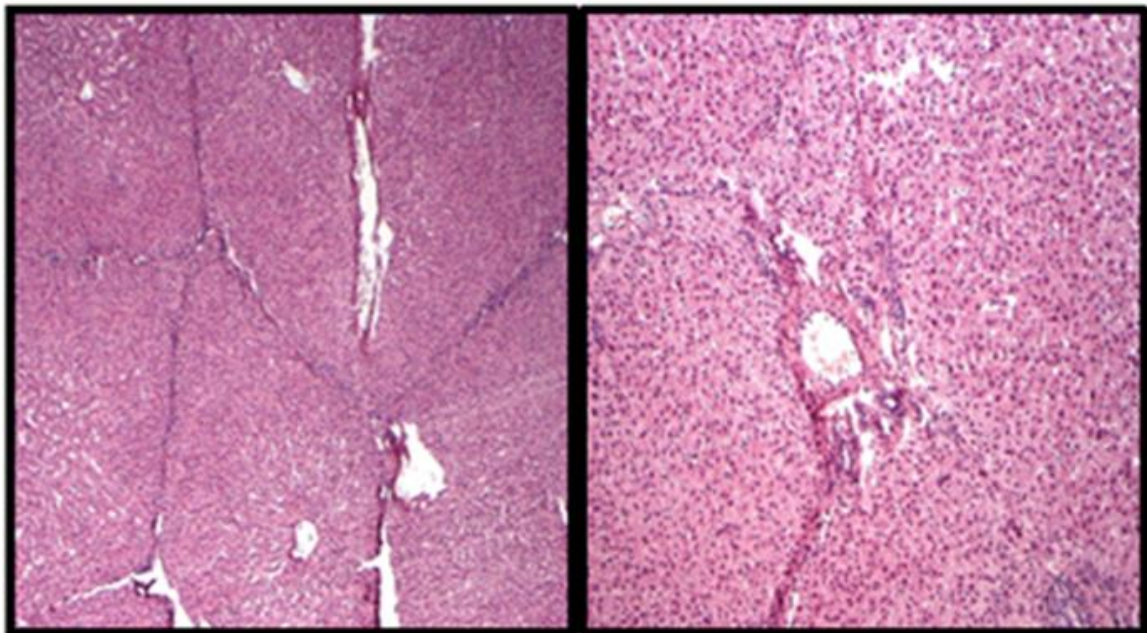


Figure 34. Histological examination of the liver biopsy before dissection showing normal liver parenchymal tissue; left panel (X40), left panel (X100).

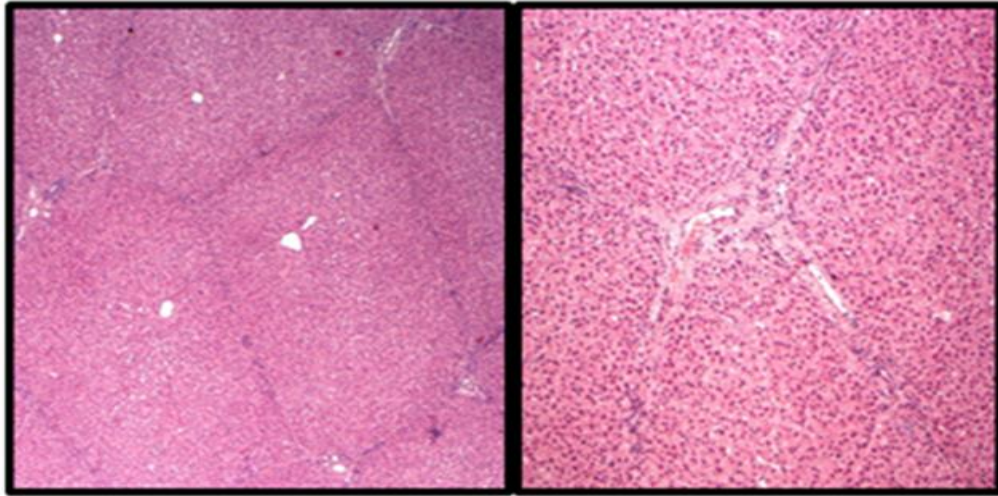


Figure 35. Histological examination of the liver biopsy immediately after dissection showing normal liver parenchymal tissue; left panel (X40), left panel (X100).

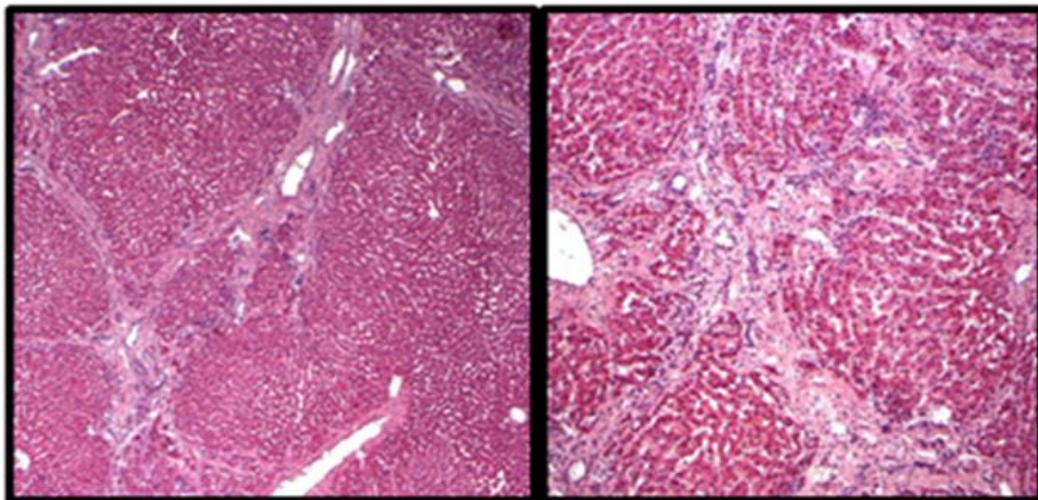


Figure 36. Histological examination of the liver biopsy 1h after connection showing normal liver parenchymal tissue; left panel (X40), left panel (X100).

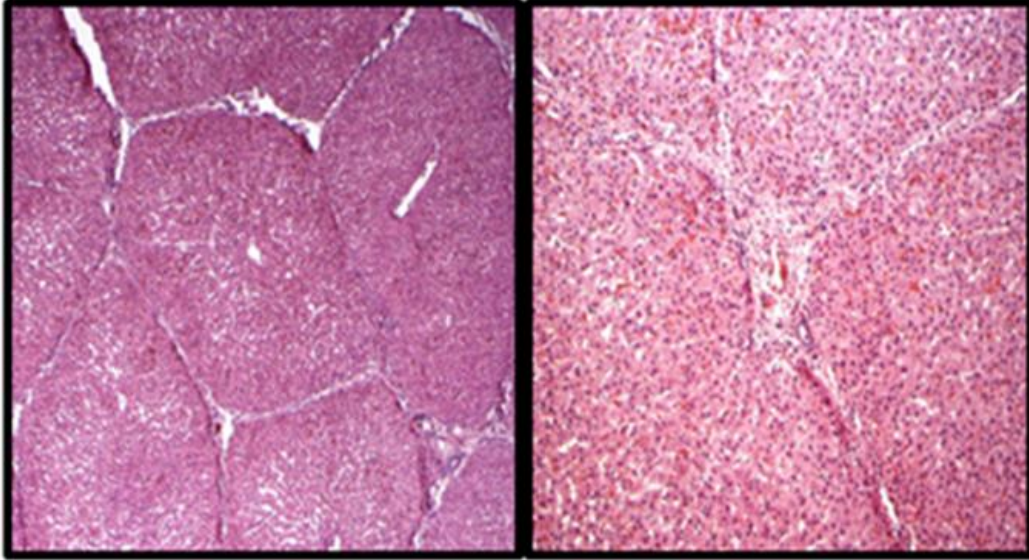


Figure 37. Histological examination of the liver biopsy 1h after connection showing normal liver parenchymal tissue; left panel (X40), left panel (X100).

Biopsies from the perfused and non-perfused areas at 4h confirmed that biopsies collected from non-enhancing areas corresponded to ischemic zones of the hepatic parenchyma compared to those from enhancing areas that revealed normal lobules [Fig. 38 & 39].

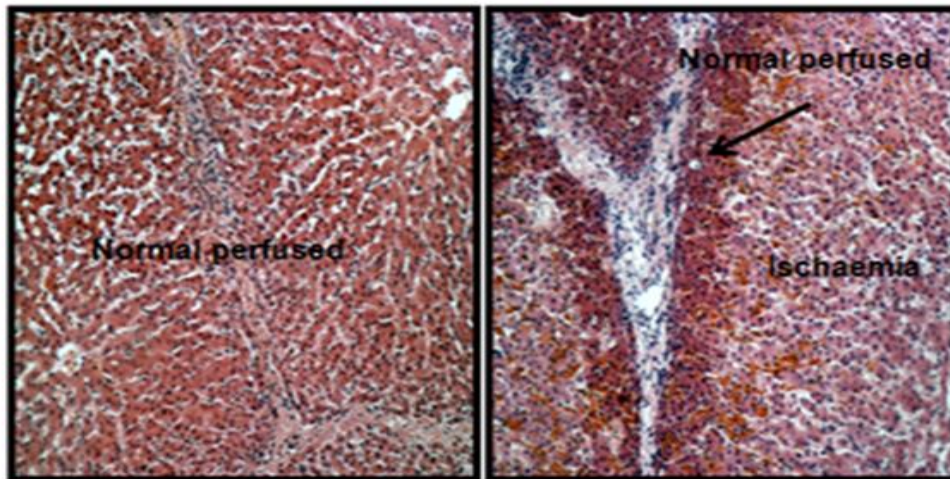


Figure 38. Histological samples of the same experiment from perfused (left panel) and non-perfused (right panel) zones. The normal hepatic lobule in the left panel is substituted by a pale centrilobular area and peripheral sinusoidal haemorrhages in the right one (20 X).

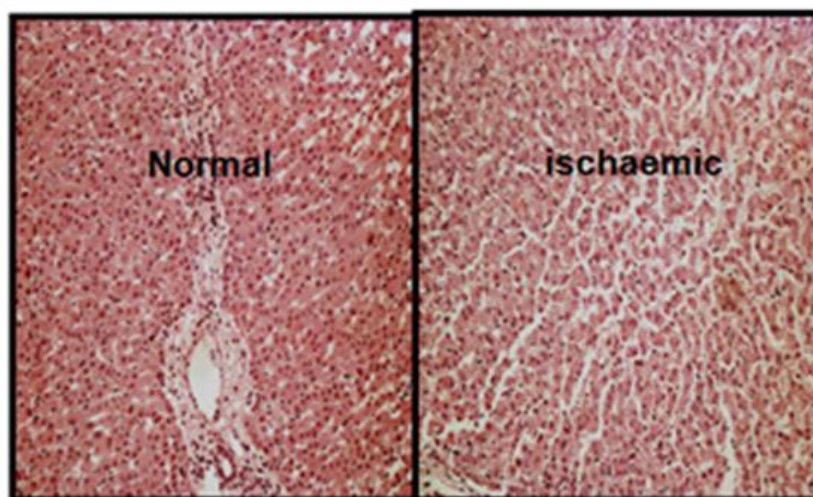


Figure 39. Histological samples of liver biopsies from perfused (left panel) and non-perfused (right panel) zones 4h after perfusion. The normal hepatic lobule (left panel) is substituted by sinusoidal congestion and karyolytic nuclei (right panel; 100 X)

Discussion:

CEUS has already been used to study postoperative complications following liver transplantation, such as biliary stenosis and vascular complications (246, 247). I used CEUS to detect areas of the liver heterogeneously perfused following liver reperfusion. CEUS agents were evenly enhanced in the whole liver parenchyma when they were injected in the first hour, but not after 4h. The decreased time to get a peak in the CEUS curve and the lower peaks achieved (outlined by the maximum gradient and the area under the curve) suggest that lower amounts of CEUS agents were received by tissues and over longer time periods compared to enhanced zones. As the function of MBs is mainly to act as intravascular contrast agents, the cause of the hypoechoic areas is likely due to hypoperfusion. To confirm the reasons for these differences at 4h, I performed Tru-Cut biopsies under US guidance and confirmed that the non-enhanced areas corresponded to tissue ischemia.

In contrast to a PET-CT scan, which is an imaging modality that metabolically evaluates the organ, CEUS at present only enhances the ability of US to detect areas of deficient perfusion, but does not furnish any information about their metabolism. Bearing this in mind, the clinical implications of this project's findings could be important in the future because

ischemic areas detected by CEUS could possibly be correlated with other parameters of liver function. This could give more data to the clinicians in the early postoperative period following liver transplantation in cases of non-functional grafts, such as livers with initial poor functions (IPF) or primary non-functions (PNF) (42-45). The use of CEUS could furnish a simple and non-invasive visual representation of ischemic areas in the early post-transplant period, opening the way to future studies of correlation with clinical outcomes (i.e. IPF vs. PNF) and experimental trials of therapies aimed to improve the local circulation (i.e. splanchnic vasodilators) or the oxygenation (i.e. increasing the inspired amount of oxygen). CEUS could also be used to follow the response to ad hoc techniques aiming at improving the perfusion.

Limitations of the study:

Although colour-coded duplex is normally used in this capacity, it was not the case in our experiments because the CEUS effects can only be exploited with Duplex imaging in large and medium-sized vessels. However, it would have been useful in this setting to compare its results with those of the CEUS. The second limitation of the current study is that it was conducted in an ex vivo translated to the clinical setting. The ischemic areas of the ex vivo model may simply result from the peculiar circuit perfusion. In fact, normothermic autologous perfused ex vivo models may deteriorate over time due to worsening acidosis from the lack of organs with clearance functions (16, 248). In this study, the focus was not to prove that ischemic areas increased in one experimental setting compared to the other (ex vivo vs. in vivo), but that CEUS was able to show them when present. CEUS is not required to detect visible ischemic zones, such as those noted at the time of reperfusion but its utility becomes evident when uncovering areas at 4h which seem perfused homogeneously. Although live animals have more physiologic mechanisms of compensation to the local microvascular hemodynamic changes than an ex vivo perfused organ, some of these are lost following transplantation (i.e. autonomous denervation). The use of live animals would necessarily require a liver transplant and the maintenance of anaesthesia for the first postoperative hours to scan the animal with the ultrasound probe. Before starting this experimental set-up, I thought it was appropriate and ethical to test CEUS on an ex vivo perfused organ first. The third limitation is the contribution of CEUS over non-contrast US in identifying ischemic areas. While such areas were not clearly identified until contrast agents were added to the circuit, this improvement shall now be defined more clearly in terms of objective data. For instance, Haematoxylin–Eosin-stained biopsies obtained from livers using each modality separately could be compared to evaluate if CEUS is more sensitive than non-contrast US for identifying areas of ischemia.

Conclusion:

Contrast-enhanced ultrasound is a useful tool for identifying areas of the liver that are hypoperfused in our ex vivo porcine liver model. The clinical implications are important because ischaemic areas detected by CEUS could be correlated for the first time with IPF or PNF, helping in the differential diagnosis of non-functional grafts. However, they could represent features peculiar to the ex vivo perfusion protocol and not necessarily be present in

an in vivo setting. Therefore, it is important to compare them with other experimental methods before testing them in clinical practice.

Chapter Three

Enhanced Role for Apoptosis in a hepatic ischaemia-reperfusion injury model

Abstract:

Background:

Prior to reperfusion, a variable period of ischaemia occurs in transplanted donor organs. There is growing evidence that apoptosis contributes to the ischaemia-reperfusion injury conundrum that follows, but its extent has not been precisely quantified. Understanding its extent and effects can help find ways to mitigate or counteract such an injury in the liver. We therefore evaluated the extent of apoptosis semi-quantitatively from the expression of Caspase-3 and M30 in a porcine ex-vivo hepatic ischaemia-reperfusion injury model and correlated the timing of expression of M30 antibody with that of Caspase-3.

Method:

From the paraffin-embedded samples of the ischaemia-reperfusion injury experiments (see chapter two, page 48), three biopsies were taken for each of 7 time points (total 21); before dissection of the liver (BD) of the livers, after dissection (AD), after connection (AC) to the circuit, at one hour perfused (1hrP) & non-perfused (1hrNP), at 4 hours perfused (4hrP) and non-perfused (4hrNP). Samples were stained with standard Haematoxylin–Eosin (HE) and immunohistochemically with Caspase-3 and M30 monoclonal antibodies. Positive cells were quantified using an ocular grid and expressed as number per square area. Cells positive for Caspase-3 & M30 antibodies were counted on the whole section. Data were expressed as median number per square millimetre. Statistical analysis was done using AVOVA and t-test. A p value of <0.05 was considered significant.

Results:

After four hours of perfusion, multiple areas of perfusion defects appeared macroscopically in all 3 livers. HE staining confirmed that these non-perfused areas were ischaemic. There was a gradual increase in Caspase-3 expression over time in all samples. There was no statistically significant difference in the Caspase-3 and M30 between the 9 specimens at 1hrP ($p=0.06$) but there was a highly significant difference between Caspase-3 and M30 at 1hrNP ($p=0.001$). Caspase-3 expression peaked at 4hrP ($p=0.001$) and 4hrNP ($p=0.03$). A similar pattern was noted with M30 which peaked at 1hrP ($p=0.001$) and maintained a non-significant expression at 4hrP ($p=0.07$) and 4hNP ($p=0.1$).

Conclusion:

The significant expression of Caspase-3 and M30 confirms that apoptosis plays an important part in tissue loss in this model of liver ischemia-reperfusion injury. Inhibiting both Caspase-3 and M30 might be useful in alleviating hepatic reperfusion injury.

Introduction:

IRI is a relatively common pathological process that follows a range of conditions of the liver including trauma, resection, transplantation, infections and shock states (249). IRI occurs when organ ischaemia results in tissue adenosine triphosphate (ATP) depletion which results in the activation of anaerobic metabolic pathways (250). These do not maintain cellular function for prolonged periods, and that ultimately leads to cell death. Restoration of blood flow is necessary to recover cellular function. Paradoxically however, reperfusion can initiate cascades that cause further cellular damage (251). Necrosis is the major mode of cell death in IRI, but its occurrence in many other situations such as liver transplantation, haemorrhagic trauma, tumour resection, and many others suggests that other mechanisms of cell death are involved. Recent studies have concluded that apoptosis is another mechanism of cell death in warm and cold hepatic IRI (7). Dramatic progress has been made over the last two decades in elucidating the intracellular signalling mechanisms of apoptosis (252). In most cells, the pro-apoptotic mediator binds to its receptor which causes receptor oligomerization and the association of various adapters (7). However, in hepatocytes, the receptor signal needs to be amplified through the mitochondria (253) which activates Caspases and initiates apoptotic nuclear changes (254). The apoptosis pathway is activated by the Caspases which are synthesised as inactive precursors and activated by specific cleavage at defined aspartate residues (255).

During IRI, TNF-alpha and various other mediators activate many of the proteins that initiate the apoptotic cascade. Apoptosis is the highly regulated process of cell death which unlike necrosis, does not elicit an immune response. It is characterised by distinct morphological changes. Cell shrinkage is seen where the cytoplasm becomes dense with cellular organelles tightly packed; followed by the irreversible condensation of chromatin, known as pyknosis, and nuclear fragmentation. This eventually leads to the immaculate removal of 'apoptotic bodies' through phagocytic engulfment; a process by which tissue homeostasis is maintained. It also acts as a defence mechanism to damaged cells due to disease or toxins. However, inappropriate apoptosis can occur in ischaemia, cancer, autoimmune and neurodegenerative diseases. In the healthy liver, the number of cells destroyed by apoptosis and produced by mitosis should be equal. However, this balance is altered during liver injury; either by disease or IRI.

The mechanism of apoptosis is highly complex with various proteins and signalling molecules involved. Research indicates that there are two main apoptotic pathways: intrinsic and extrinsic. The extrinsic pathway is initiated by ligand binding to cell surface death receptors which leads to the formation of the death-inducing signalling complex (DISC). The intrinsic pathway of Caspase activation is initiated by mitochondrial events such as DNA damage, growth factor withdrawal, or loss of contact with the extracellular matrix (256). However, both pathways can influence each other (257).

Caspases (cysteinyl aspartate-specific protease):

Caspases are a family of aspartate specific cysteine proteases that are synthesized as inactive zymogens containing a variable length pro-domain followed by a large (20kDa) and a small (10kDa) subunit. They are the primary mediators in the role of apoptosis and inflammatory response of a mammalian cell. There are three functional subdivisional groups of the caspase family, apoptotic initiator caspases (8, 14-16), apoptotic effector caspases (3,6,7) and caspases involved in inflammatory cytokine activation (1,4,5,11 and 12L/12S) (257).

Apoptotic Caspases are activated by either an extrinsic or an intrinsic stimulus. The extrinsic pathway is initiated by ligand binding to cell surface death receptors (TNF RI, Fas/CD95, DR3, TRAIL R1/DR4, TRAIL R2/DR5) causing receptor oligomerization and cleavage of Pro-caspases-8 and -10 which leads to activation of Caspase-8 and Caspase-10 resulting in cleavage of BID and downstream effector Caspases. Activation of the intrinsic Caspase pathway is initiated by changes in a cells homeostatic state by events such as DNA damage, growth factor withdrawal or loss of contact with the extracellular matrix. These events lead to changes in the integrity of the mitochondrial membrane that result in the release of pro-apoptotic proteins including Cytochrome c, Smac/Diablo, HtRA2/Omi, Apoptosis-Inducing Factor (AIF) and Endonuclease G (258).

Initiator Caspases are activated in three distinct protein complexes, the death inducing signal complex (DISC; Caspase-8 and -10), the apoptosome (Caspase-9) and the PIDDosome (Caspase-2). The DISC is formed following ligand binding and death receptor oligomerization. In contrast, Pro-caspase-9 is activated following an intrinsic change to the cells mitochondrial membrane leading to the release of Cytochrome C. When released into the cytoplasm, Cytochrome C interacts with APAF-1, recruiting Pro-Caspase-9 by way of its Caspase recruitment domain (CARD) to form the apoptosome. This formation of the apoptosome leads to the cleavage and activation of Caspase-9 (259).

Bcl-2 Family:

Bcl-2 is a family of proteins that is notable for the regulation of apoptosis at the level of the mitochondrion. They exhibit their effects on promoting or inhibiting apoptosis by governing the outer membrane permeabilisation. They act upstream of the Caspases. Inhibiting apoptosis members of Bcl-2 include bcl-2, bcl-xL, bfl-1, mcl-1 and A1. Apoptosis promoting members include bax, bak, bcl-xS, bad, bid, bik and Hrk (260). The family regulates apoptosis in an on/off (rheostatic) effect. An increase in the pro or inhibitory members over the converse members will cause the desired effects.

Bcl-2 proteins key function at the mitochondrion is to change the transmembrane potential and release Caspase activating agents, such as cytochrome C. The main theory is that activation of the mitochondrial permeability transition pore, by changes in Ca²⁺ and voltage leads to changes of voltage-gated channels. This causes changes to the mitochondrial membrane permeability, and proteins such as cytochrome C are released and become

involved in downstream mechanisms that activate Caspases (261). Conversely the agents prohibiting apoptosis prevent the release of such substances to the cytosol (261).

Bcl-2 is a strong regulator in anti-apoptosis mechanisms. For example in breast epithelial cells, Estrogen stimulation leads to up-regulation of bcl-2 and the resistance to apoptosis (262). Bax has been shown to act as a tumour suppressor gene. One study has shown that more than 50% of colon cancers exhibiting the microsatellite mutator phenotype contain disabling somatic mutations in the Bax gene (263).

Cytokeratin 18 (CK18):

This is a filament protein (a substrate of Caspase) during hepatocellular apoptosis, and is subsequently released into the circulation. Identifying levels of CK18 can be used as a non-invasive method to quantify liver damage. Essentially, it can be used as a biomarker of apoptosis in liver disease or damage. During the apoptotic cascade, CK18, once cleaved by Caspase 3, exposes a specific epitope, not usually identified on normal CK18 cells. This epitope is not seen in cells dying by necrosis (264).

Caspase-3:

Caspase 3 is a protein and signalling molecule encoded by the *CASP3* gene on the q arm of chromosome 4. It is activated by both the intrinsic and extrinsic pathways of apoptosis. Known as the 'executioner', it co-ordinates the destruction of cellular structures, in particular DNA fragmentation. Poly ADP ribose polymerase (PARP) is a nuclear protein that functions in DNA duplication, recombination, repair, regulation and control of cell cycle, cell differentiation, and cellular apoptosis (255). Activation of Caspase-3 requires cleavage of its zymogen into two segments. Following activation it participates in activating PARP, thus inducing cellular morphological changes and DNA degradation. The activity of Caspase-3 is also regulated by other apoptosis regulating and controlling factors, such as p53, bcl-2, and bax (251).

M30:

This is a monoclonal antibody that is a major intermediate filament protein in the liver. It detects an epitope on CK18. More recently the detection of M30 has been used as an indicator of the apoptotic process as it is easily detected in the plasma (265).

It has been noted that high levels of M30 is associated with severe inflammation and tissue damage, especially for liver diseases, particularly steatohepatitis. Raised levels of M30 have also been detected in patients diagnosed with cholestasis or cholangitis; indicating the occurrence of apoptosis (266).

One study showed that levels of M30 and other apoptotic proteins were significantly raised in patients with acute liver failure (ALF) in comparison to patients with chronic liver disease or healthy controls. It also showed that levels of M30 correlated with severity of liver damage, with the highest noted in patients in coma stage of ALF (113).

Various studies have been conducted to assess apoptosis in IRI by measuring levels of CK18 and M30 using antibody assays. The majority of hepatocellular damage is shown to occur in the acute phase of IR. A study by Sasaki *et al* (236) showed that high levels of M30 were seen 3-4 hours after IR indicating commencement of apoptosis. After 24 hours M30 levels were undetectable. However a study conducted by Topaloglu, *et al* (265) showed that levels of M30 had significantly decreased but was not entirely undetectable.

A study assessed levels of CK18 during IR of mice liver showed that CK18 levels did not change during both ischaemia and reperfusion, except for 3 hours post reperfusion, where levels had increased 3-fold. In comparison levels of FK18, a biomarker for necrosis, had increased more than 200-fold. This study suggested that the vast majority of damage during IRI is due to necrosis rather than apoptosis (237).

Herein, I explored the expression of Caspase-3 antibody in IRI to assess the role of apoptosis in in IRI. I also used the monoclonal M30 antibody that recognizes a Caspase-generated Cytokeratin-18 neoantigen, and studied its correlation with Caspase-3 in a time-dependent manner.

Method:

Tissue samples:

The experiments were performed on the tissue samples taken from the paraffin-embedded sections of the ischaemia-reperfusion injury experiments (see chapter two, page 48). Three biopsies were taken for each of 7 time points (total 21); before dissection of the liver (BD) of the livers, after dissection (AD), after connection (AC) to the circuit, at one hour perfused (1hrP) & non-perfused (1hrNP), at 4 hours perfused (4hrP) and non-perfused (4hrNP) [Fig. 40].

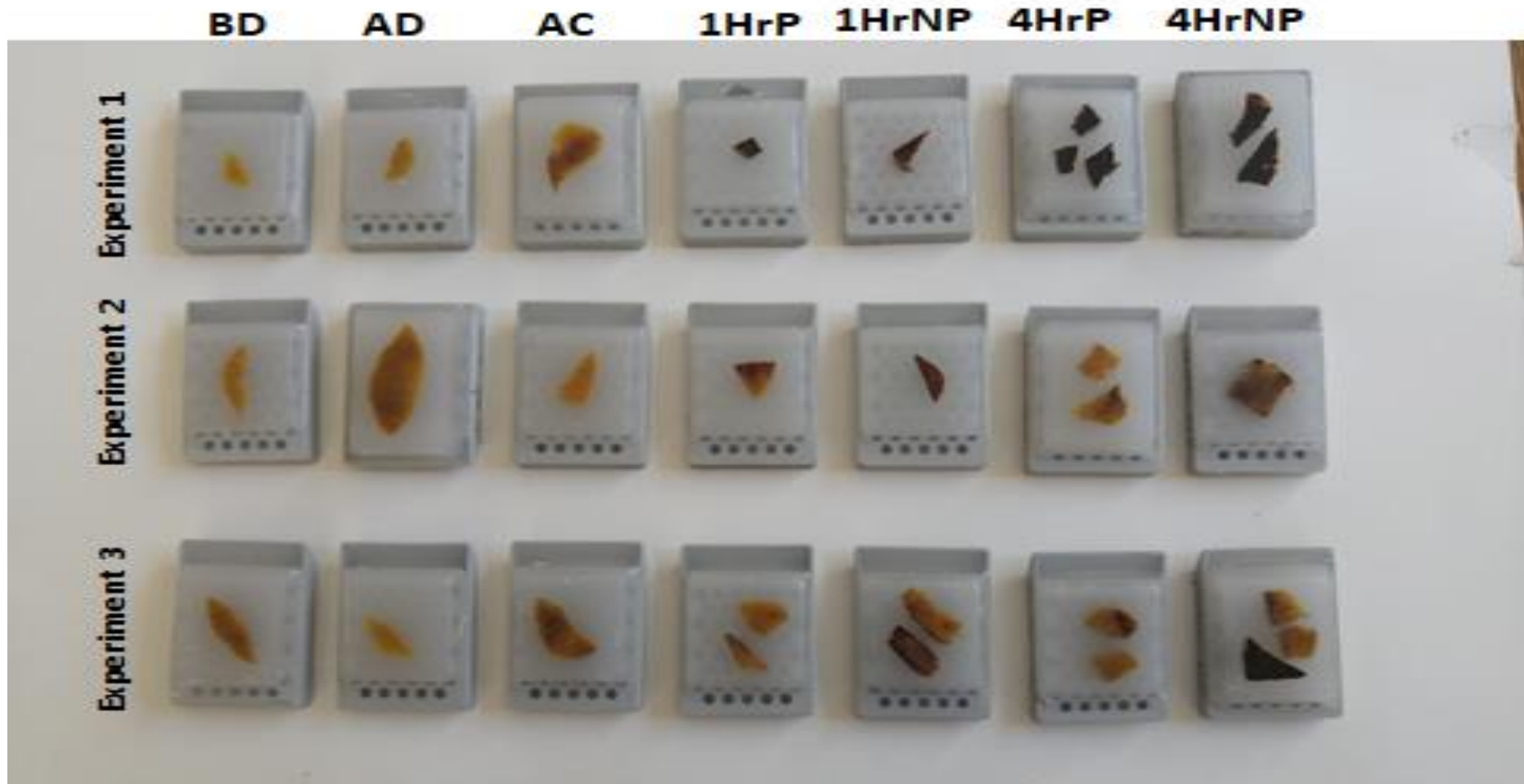


Figure 40. Paraffin-embedded section. (BD=Before Dissection, AD=After Dissection, AC=After Connection, 1hrP=1 hour Perfused, 1hrNP=1 hour Non-Perfused, 4hrP=4 hour Perfused, 4hrNP=4hour Non-Perfused)

Antigen retrieval:

In order to retrieve the antigens, the specimens were cut onto Vectabond slides, left to dry at 37°C overnight and heated for 10 minutes at 65°C. They were then deparaffinised using xylene, rehydrated using graded alcohols (99% then 95% Industrial Methylated Spirits “IMS”) and then rinsed with tap water for five minutes. The slides were placed on a slide rack in a plastic dish, which was then topped up with 10mM Sodium Citrate (pH 6.0). The dish was microwaved at 80% power for 20 minutes and left to cool in the buffer at room temperature.

Immunohistochemistry assays:

Immunohistochemistry for apoptosis was performed using Cleaved Caspase-3 “Asp 175”, (New England Biolabs) as the primary antibodies: and M30 (CytoDeath. Bioaxxess) utilising NovoLink Polymer Detection System (Leica Microsystems. RE7140-CE). The slides were washed with a buffering Blocking Solution - (TBS/3%BSA/0.1% Triton-X-100) which acted as the primary antibody diluent. The endogenous peroxidase was neutralised by using Peroxidase Block for 5 minutes. The slides were washed in alternate cycles using TBS for 2 x 5 minutes. After each washing cycle, the following was done in this order: the slides were incubated with Protein Block for 5 minutes, incubated with optimally diluted primary antibody, second incubation with Post Primary Block for 30 minutes, third incubation with NovoLink Polymer for 30 minutes and finally developed peroxidase activity with DAB working solution for 5 minutes. The slides were then washed in tap water for another 5 minutes and counterstained using Mayer’s Haematoxylin for 30 seconds. A final wash with tap water for 5 minutes before dehydration with air and mounted in DPX. The identification of apoptotic cells was confirmed when there was evidence of Caspase-3 and M30 positivity

Quantitative apoptotic index:

The apoptotic index was expressed as the ratio of the number of hepatic cells with Caspase-3 and M30 positivity out of the total number of nucleated cells in each field (magnification, x40) calculated after counting 5 random microscopic fields for each time point with a 19mm Whipple grid graticule lens (Pyser-SGI LTD) [Fig. 41]. In each field, 100 squares were evaluated for the presence of apoptotic cells. Activated Caspase-3 hepatocytes positive for DNA fragmentation [Fig. 42] and for cytoplasmic activity for M30 [Fig. 43] were counted on the whole sections. The mean counts were expressed as a percentage of the total number of non-apoptotic cells counted in each field.



Figure 41. The 19mm Whipple grid graticule lens (Pyser-SGI LTD)

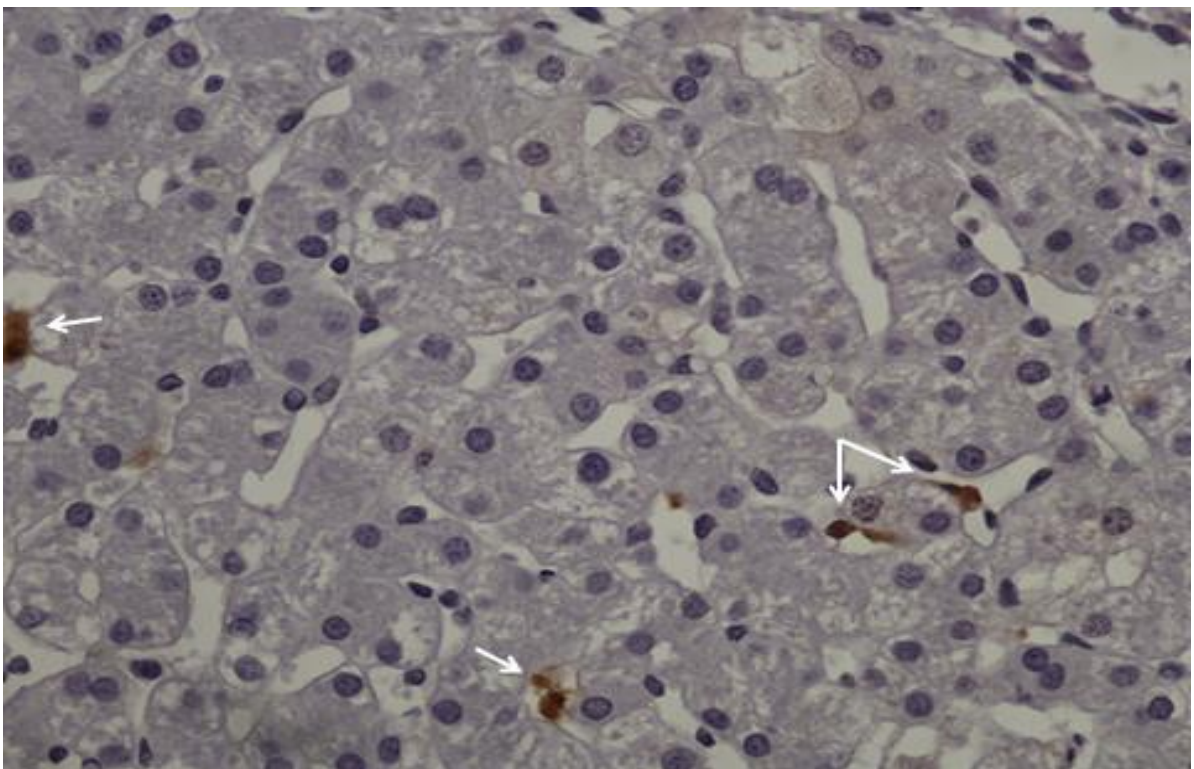


Figure 42. An example of Caspase-3 expression

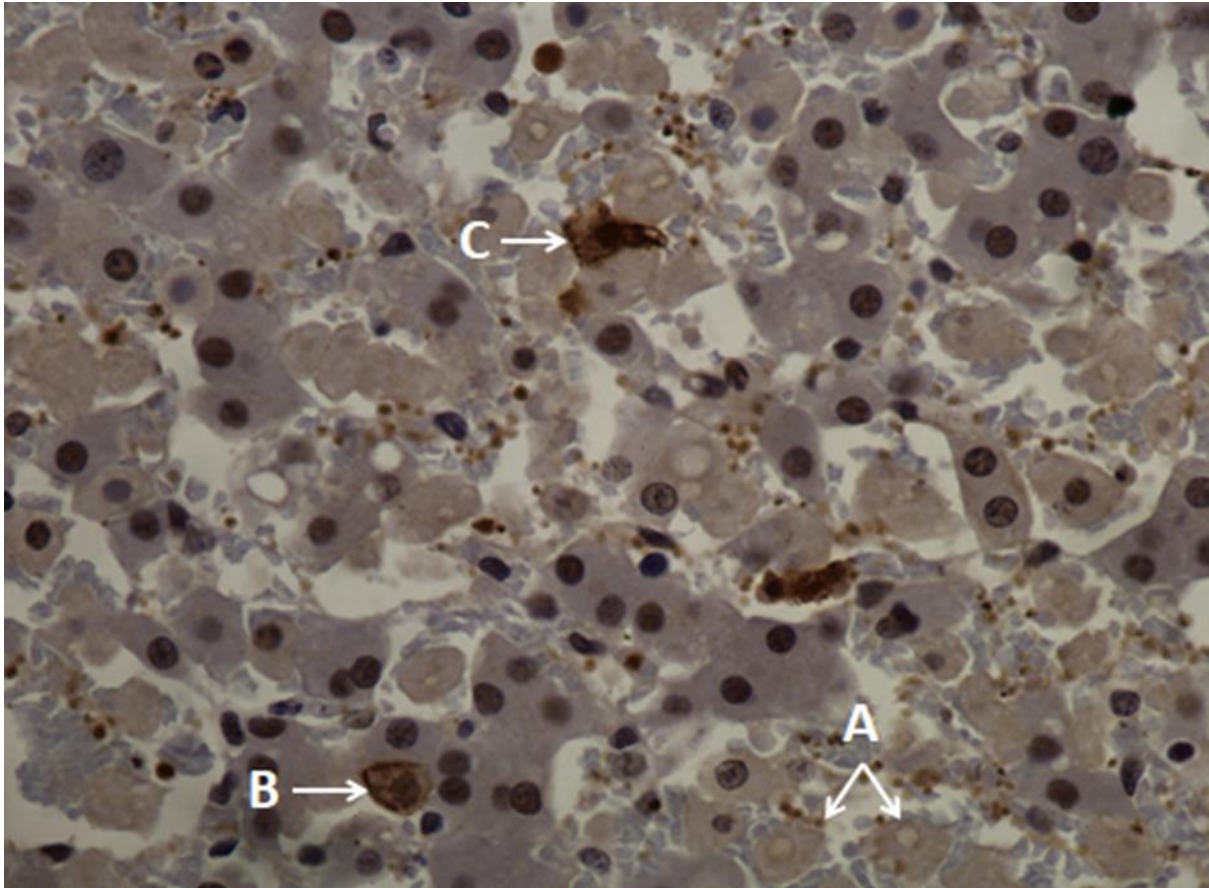


Figure 43. An example of M30 expression in hepatocytes ranging from weak (A), intermediate (B) to strong (C) reactions (original magnification $\times 50$).

Microscopic examination:

Caspase-3 expression:

Caspase-3 maintained the same expression BD & AD, dipped AC then gradually increased after perfusion in the Perfused and non-perfused areas [Fig. 44].

M30 expression:

There was not much evidence of M30 BD. It slightly increased AD, dipped AC, but peaked at 1hrP. Its expression was less in the 1hrNP and at 4hrP and 4hrNP [Fig. 44].

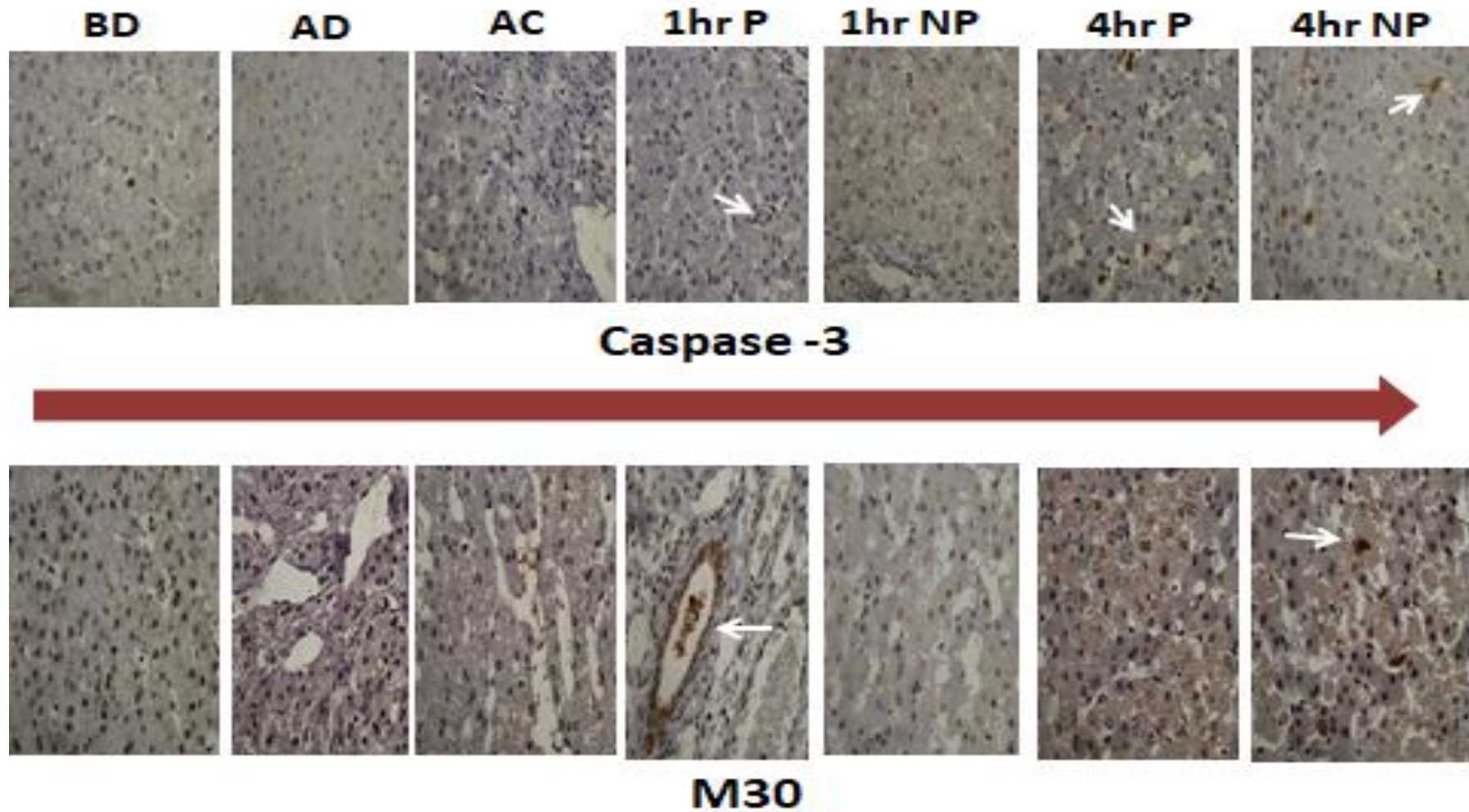


Figure 44. A comparison between the expression of Caspase-3 (upper panel) & M30 (lower panel) “white arrows” at each point in time (BD=Before Dissection, AD=After Dissection, AC=After Connection, 1hrP=1 hour Perfused, 1hrNP=1 hour Non-Perfused, 4hrP=4 hour Perfused, 4hrNP=4hour Non-Perfused). (Original magnification x 50)

Statistical Analysis:

Median values of the different groups were compared by ANOVA and linear correlation tests.

Caspase-3 expression:

There was a gradual increase in Caspase-3 expression in all samples. The difference was non-significant at 1hrP ($p=0.06$) and a highly significant at 1hrNP ($p=0.001$), then it peaked at 4hrP ($p=0.001$) and 4hrNP ($p=0.03$) [Fig. 45].

M30 expression:

A similar pattern to Caspase-3 expression was noticed with M30 which peaked at 1hrP ($p=0.001$) and maintained a non-significant expression at 4hrP ($p=0.07$) and 4hNP ($p=0.1$). The overall difference among the groups along the time scale was significant ($p=0.01$) [Fig. 45].

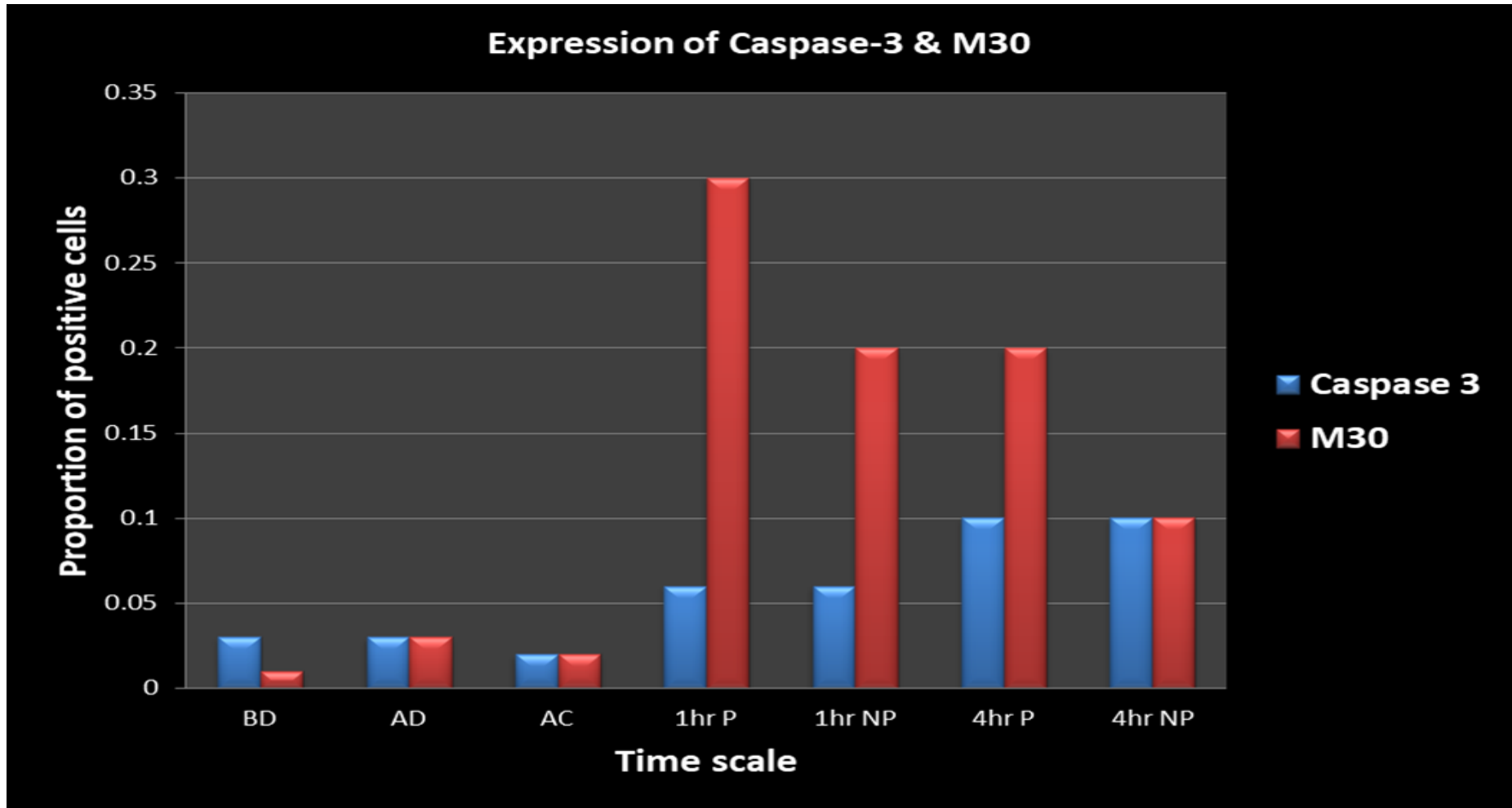


Figure 45. Expression of Caspase-3 & M30 in the liver biopsies at each time point (BD = Before Dissection, AD = After Dissection, AC = After Connection, 1hrP = 1 hour Perfused, 1hrNP = 1 hour Non-Perfused, 4hrP = 4 hour Perfused, 4hrNP = 4 hour Non-Perfused).

Discussion:

Its dual blood supply makes the liver uniquely suitable for IRI modelling. The complex conundrum of IRI in the liver appears to involve cellular mediators, reactive oxygen species, the complement system, cytokines and other secreted factors. It has been postulated that much of the damage in IRI was due to necrosis (7). However there is growing evidence that apoptosis also contributes to the damage since blocking necrosis does not completely stop the damage from IRI (7).

None of the proxy methods currently used to infer apoptosis or its extent is considered to be valid. For example, serum parameters such as ALT, AST and LDH do not reflect the scale of IRI tissue injury as they have to be monitored before and after perfusion (267). Although HE staining demonstrates Councilman bodies which are the end result of apoptosis, it does not reflect the number of events in this mode of cell death. The terminal deoxynucleotidyl transferase-mediated deoxyuridine triphosphate nick-end labelling (TUNEL) assay is no different from the first two methods. It is not reliable as it has been shown to be non-specific. It requires highly standardized procedures and it does not differentiate between apoptotic and necrotic cells (264, 268).

The exploration of different modes of cell death can help open new venues for therapeutic targeting of IRI. Jaeschke, *et al* (7) propose the theory of necroapoptosis in which common pathways lead to both necrosis and apoptosis. This is due to the mitochondrial permeability transition, whereby ATP depletion leads to cell membrane failure and necrosis while partial ATP preservation allows the mitochondria to release Caspases which lead to apoptosis. Therefore in this theory, necrosis and apoptosis could be thought of as leading to the ends of a spectrum depending on the ATP depletion. Accordingly if the start of this common pathway could be found then both necrosis and apoptosis could be reduced during liver IRI.

In this study, I have demonstrated the correlation between Caspase-3 and M30 antibodies in IRI-associated apoptosis, showing a statistically significant gradual increase in Caspase-3 expression, However M30 showed a statistical significant increase after the first hour. Those results show that apoptosis as well as necrosis had a significant role to play in liver IRI. Therefore to stop the injury from IRI then one would need to stop both the pathways of necrosis and apoptosis.

Limitations of the study:

Ex-vivo models like this one are limited by a 6-hour run time in contrast to in-vivo models such as that of Sun, *et al* (269) and Tsung, *et al* (270) who could extend their experiment to measure late effects for up to 24hrs after reperfusion. Secondly, the accuracy of the apoptotic index depends on the identification of apoptotic cells which can be magnification dependent, as Shining, *et al* (271) point out. To reduce such counting errors we used the recommended high-power (x40) lens. Finally, because the duration of morphologically detectable stage of apoptosis may vary, apoptotic index does not always correlate well with an actual "death index" (272).

Conclusion:

In this model, apoptosis plays a significant role in liver IRI. However, further research is needed to validate this both ex-vivo and in-vivo to confirm our findings and thus pave the way for work to find a suitable apoptosis-based therapeutic target. This could have wide ranging implications and application in liver trauma, sepsis, resection and transplantation.

Chapter Four

Contrast-enhanced ultrasound provides better evaluation of microwave ablations in an ex vivo perfused porcine liver model

Abstract:

Background:

Microwave ablation (MWA) under different imaging guidance is a new technique for treating liver malignancies.

Aims:

To investigate the use of contrast-enhanced ultrasound (CEUS) in the assessment of the ablation zone in an ex vivo perfused porcine liver model.

Material and methods:

MWA ablations with different powers (50W, 70W, 90W) were created in five perfused porcine livers. Dimensions of the ablations were measured on morphology, grey-scale US and CEUS. Biopsies from the ablated areas were taken for histology. ANOVA test was used for analysing data.

Results:

There was better demarcation of the lesion border on CEUS when compared with Grey-scale US. There was a significant difference ($p < 0.0001$) in the long axis of the ablation among morphology, grey-scale US and CEUS, and a significant difference in the lesion size between powers ($p = 0.0064$). There was no difference in the short-axis, but a significant difference in the lesion size between powers ($p = 0.0306$). A significant difference in the width of the transitional zone (TZ) was noticed between powers 50W and 90W ($p = 0.015$).

Conclusion:

CEUS shows better demarcation of the ablated zone when compared with grey-scale-US, a finding that could provide guidance in the assessment of the ablation zone during treatment. CEUS does not show superiority over morphology or grey-scale US in reflecting the actual size of the lesion. Histology remains the only method to provide the exact measurements of the transitional zone width when compared with morphology. Further research is required confirm these results.

Introduction:

Different in vivo and ex vivo experimental and clinical studies have been performed to evaluate the relation between power, type of probe and ablation size on morphology, histology, and radiology. In their review article, Gravante *et al* (55) concluded that the correct use of MWA with technical improvement in the equipment could achieve a large ablation size with a high rate of complete tumour destruction. That conclusion was also confirmed by four more studies (43, 273-275). Other experiments assessed ablation lesions on morphology, histology and imaging. Matsukawa, *et al* (276) compared the created MWA lesions in 12

cadaveric porcine livers and 9 live rabbit livers on histology and grey-scale US. They found that the hyperechoic areas measured with grey-scale US were significantly larger than the actual necrotic areas ($p < 0.01$) on histology, probably due to air bubbles which developed within the tissue. Correlation between histology and MRI intensity signal (low in the central necrotic zone, a high in the intermediate zone and an isointensity in the outer zone) was demonstrated in other studies (277, 278). CT showed a hypodense necrotic ablated lesion with no enhancement with contrast (275, 277, 279). Lesion evaluation with these methods has few practical and logistical issues such as efficiency of the imaging technique, exposure to radiation, cost, time, experimenting on live animals and the need for a well-trained radiographer or surgeon with enough knowledge to assess targeted lesion during or after treatment (244, 280).

Material and Methods:

Liver Procurement:

Five white were used for this study and liver procurement was done as described on page-54.

Circuit preparation: as described on page 79.

Perfusion: as described on page 79.

Microwave ablation:

In each liver, MWA lesions were created one hour after liver perfusion to make sure all physiological parameters have settled. The microwaves were generated by a Microsulis Tissue Ablation Sulis TMV Generator (Microsulis Ltd., Denmead, Hampshire, UK) at a frequency 2.45 GHz [Fig. 46] and delivered via the Accu5i applicator (Microsulis Ltd., Denmead, Hampshire, UK) which has a shaft diameter of (9mm) and a biocompatible non-stick coating [Fig. 47]. The applicator was inserted to 2cm beneath the surface of the liver in all applications to achieve a consistent shape throughout the study. Nine lesions were created at three different powers (50W, 70W and 90W), (3 lesions for every power) for a two-minutes time duration for each lesion [Fig. 48].



Figure 46. Microsulis Tissue Ablation Sulis TMV Generator (Microsulis Ltd., Denmead, Hampshire, UK)



Figure 47. Accu5i antenna (Microsulis Ltd., Denmead, Hampshire, UK)

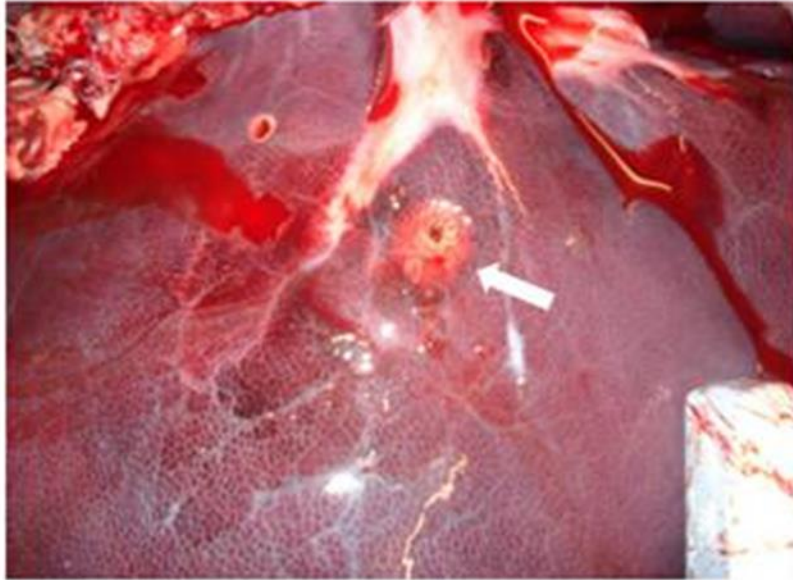


Figure 48. An example of the created microwave ablation in the porcine liver (white arrow)

Liver scanning:

Baseline liver images were taken without CA [Fig. 49] and with CA [Fig. 50]. After MWA, the liver was again scanned without CA [Fig. 51] and with CA [Fig. 52]. All images and cine loops were saved on a LOGIQ 9 US machine (GE Healthcare, Chalfont St Giles, UK) [Fig. 53]. The CA (Sonovue, Bracco, Milano, Italy) consisted of phospholipid-stabilized MBs containing Sulphur Hexafluoride gas with a diameter of less than 8 μm (mean 2.5 μm) reconstituted with 5ml of 0.9 % normal saline solution [Fig. 54]. The MBs were injected in the hepatic artery (HA) valve followed by 5ml normal saline wash.



Figure 49. Baseline grey-scale ultrasound image of the liver without contrast agents

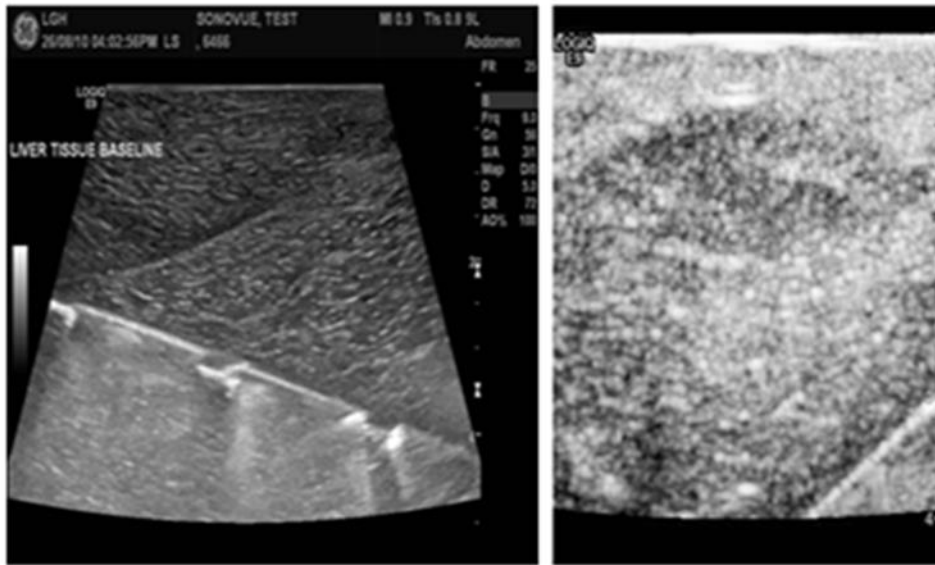


Figure 50. Baseline grey-scale ultrasound image of the liver with contrast agents

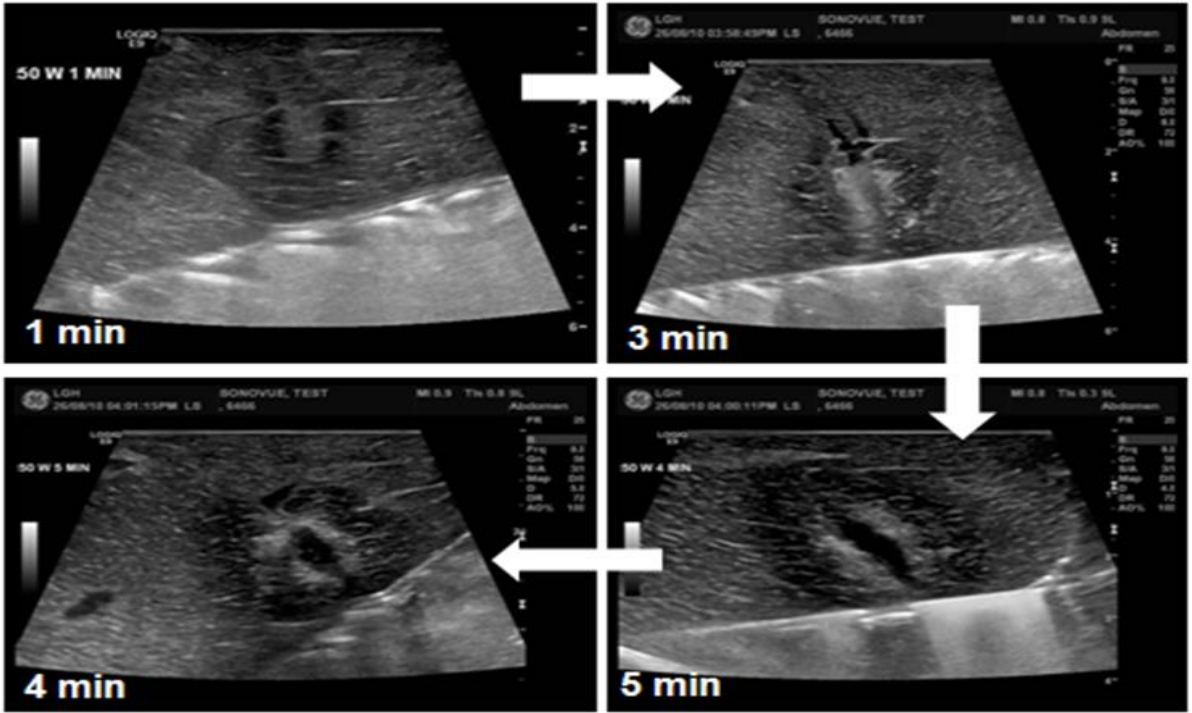


Figure 51. Baseline grey-scale ultrasound image of the microwave ablation without contrast agents. Notice the changes in the lesion appearance with time (white arrows).

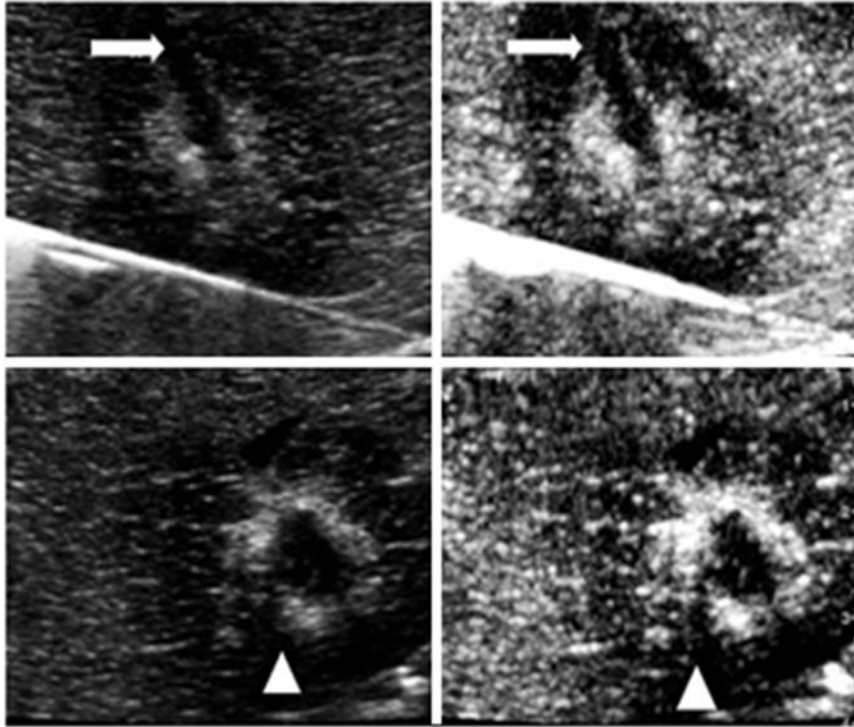


Figure 52. The appearance of the same microwave ablation lesion with contrast agents. Coronal plane (upper panel) and transverse plane (lower panel). Notice the probe insertion site (white arrows) and the necrotic tissue around it (white triangles).



Figure 53. Logiq E9 ultrasound machine ((GE Healthcare, Chalfont St Giles, UK)

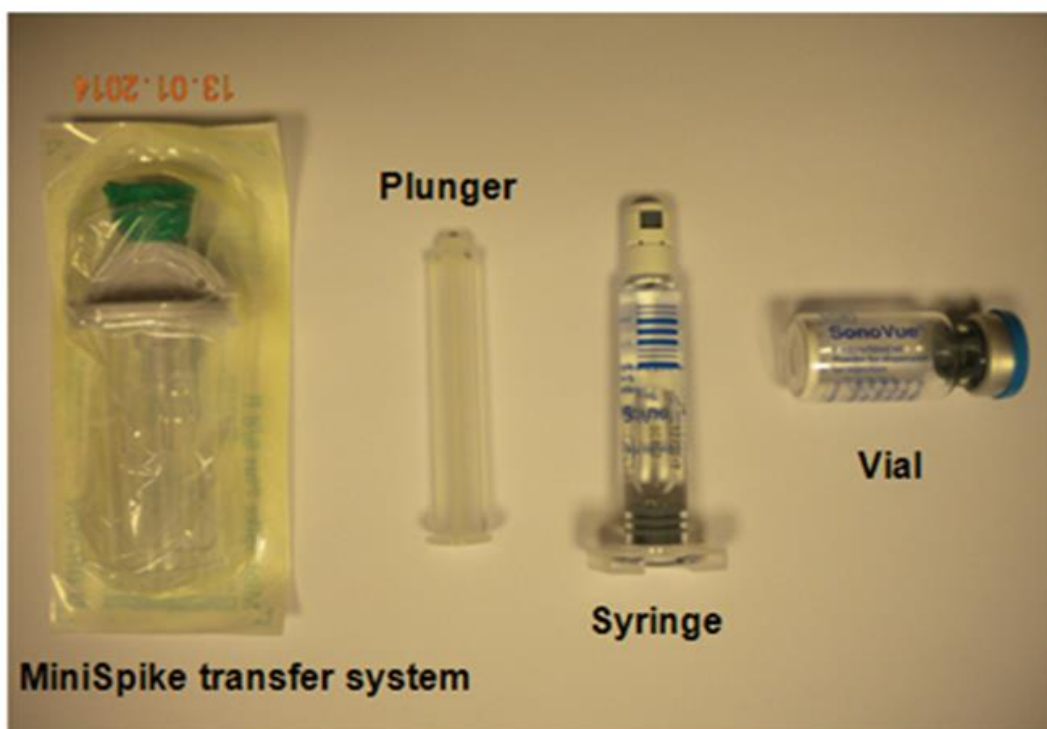


Figure 54. Sonovue microbubbles (Sonovue, Bracco, Milano, Italy)

Quantification of MBs in the ablated zone:

The US machine was equipped with a specific contrast software to create “wash-in”/“wash-out” curves, a measure of the contrast acquisition and removal in a particular scanned area, evidenced during the imaging acquisition and processing. The software provided real-time images with and without the presence of contrast, and the intensity of the acoustic signal was assessed on the video recording extracted every 5s following injection. Standardized 12- to 18-mm regions of interest were chosen for analysis from hyperechoic, hypoechoic, and anechoic areas. The parameters which were evaluated from the time–intensity curves included “time to peak” (time elapsed from the start of the scan to the maximum intensity of the medium contrast in a defined region, evaluating how quickly the medium contrast peaks in that region), “maximum gradient” (maximum difference between the lowest and highest values recorded of the medium contrast intensity from the start to the end of the scan, evaluating the net increase of contrast reaching that region), and the “area under the curve” (the area under the actual time–intensity curve of the medium contrast, a measure of the total amount of contrast reaching the area over the scan).

Lesion analysis:

The lesions were sliced and the dimensions (long-axis and short-axis) of the whole lesions were measured on morphology [Fig. 55], grey-scale US [Fig. 56A] and CEUS [Fig. 56B] and then compared. Wedge biopsies were taken from the lesion for histology. All biopsies were saved in Formalin and then assessed with Haematoxylin-Eosin (HE) stain. All data were entered into an Excel database. Numerical data reported as mean (M) +/- standard deviation (SD). Analysis of data was performed with ANOVA test. A (*P* value of <0.05) was considered significant.

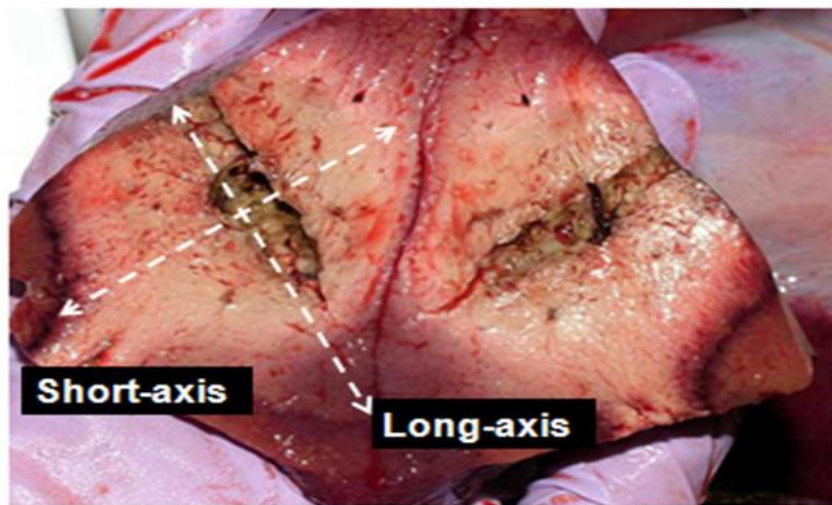


Figure 55. Measurements of a lesion dimensions on morphology

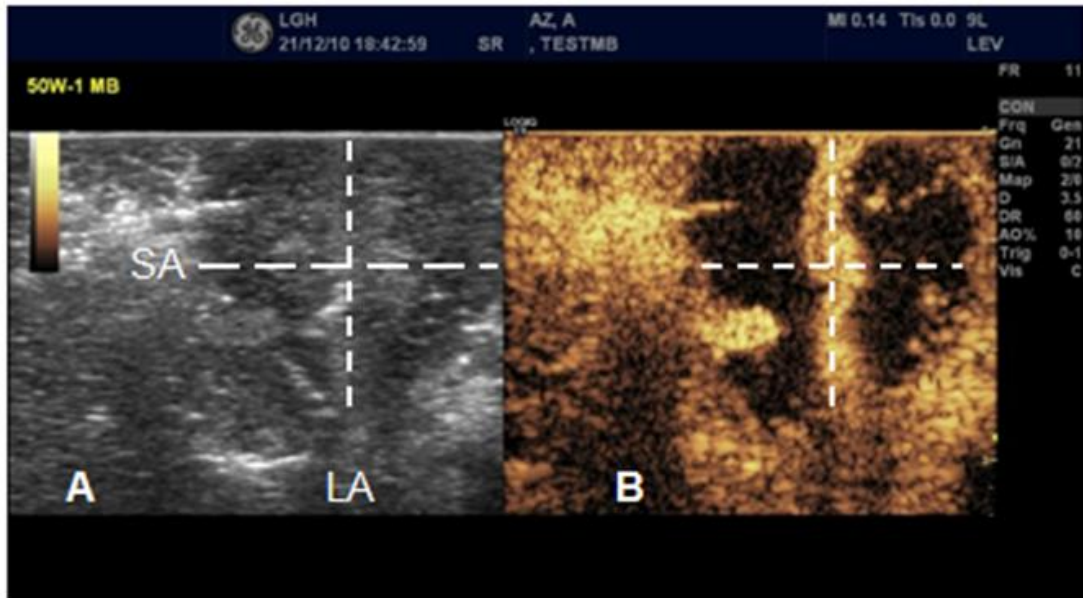


Figure 56 A & B. An example of the measurement of a lesion dimensions on grey-scale ultrasound (A) and CEUS (B)

Results:

Grey-scale US:

All baseline images showed homogenous enhancement of liver tissue. The ablations were reported as one hypoechoic area compared to the normal isoechoic surrounding liver parenchyma [Fig. 57 A, B & C “left panel”].

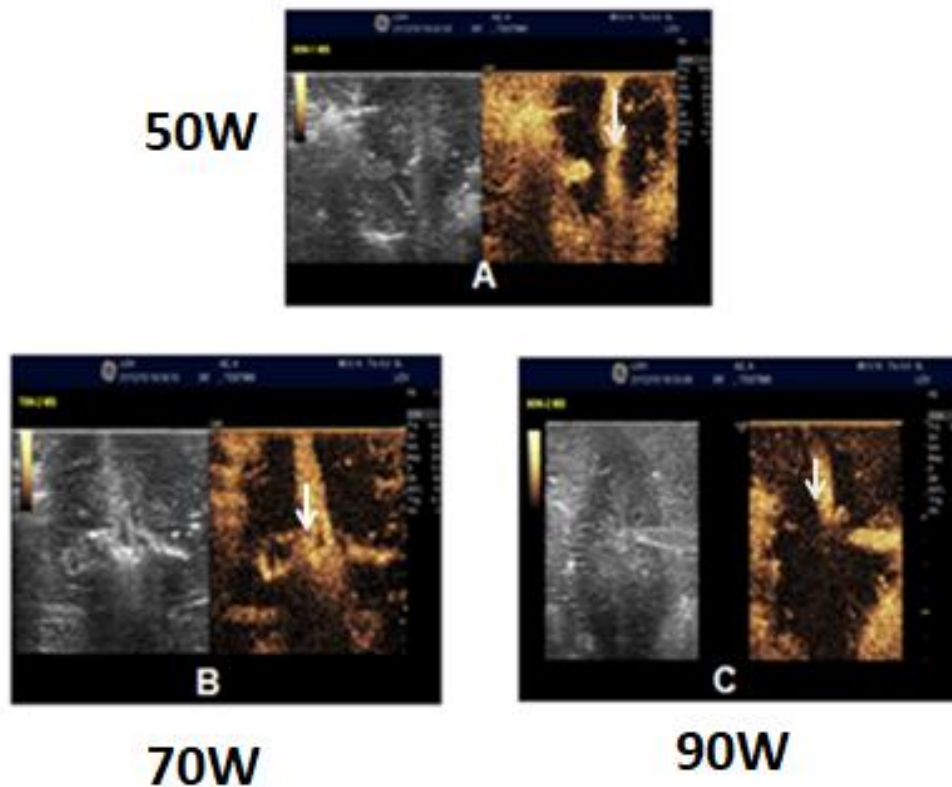


Figure 57. An example of the hypoechoic lesions with different powers on grey-scale ultrasound (left panel) and with CEUS (right). Notice the enhancement of the probe insertion site with MBs (white arrow)

For powers 50W, 70W and 90W, the mean values for the long-axis dimensions were (25.8 \pm 1mm), (28.9 \pm 2.8mm), (34.6 \pm 2mm) respectively, and for the short-axis were (25.2 \pm 0.8mm), (28.1 \pm 2.2mm), (26.3 \pm 2.7mm) respectively. There was a significant difference in the long-axis between power 50W and 90W ($p=0.05$) [Fig. 58]. There was no difference in the short axis among the powers [Fig. 59].

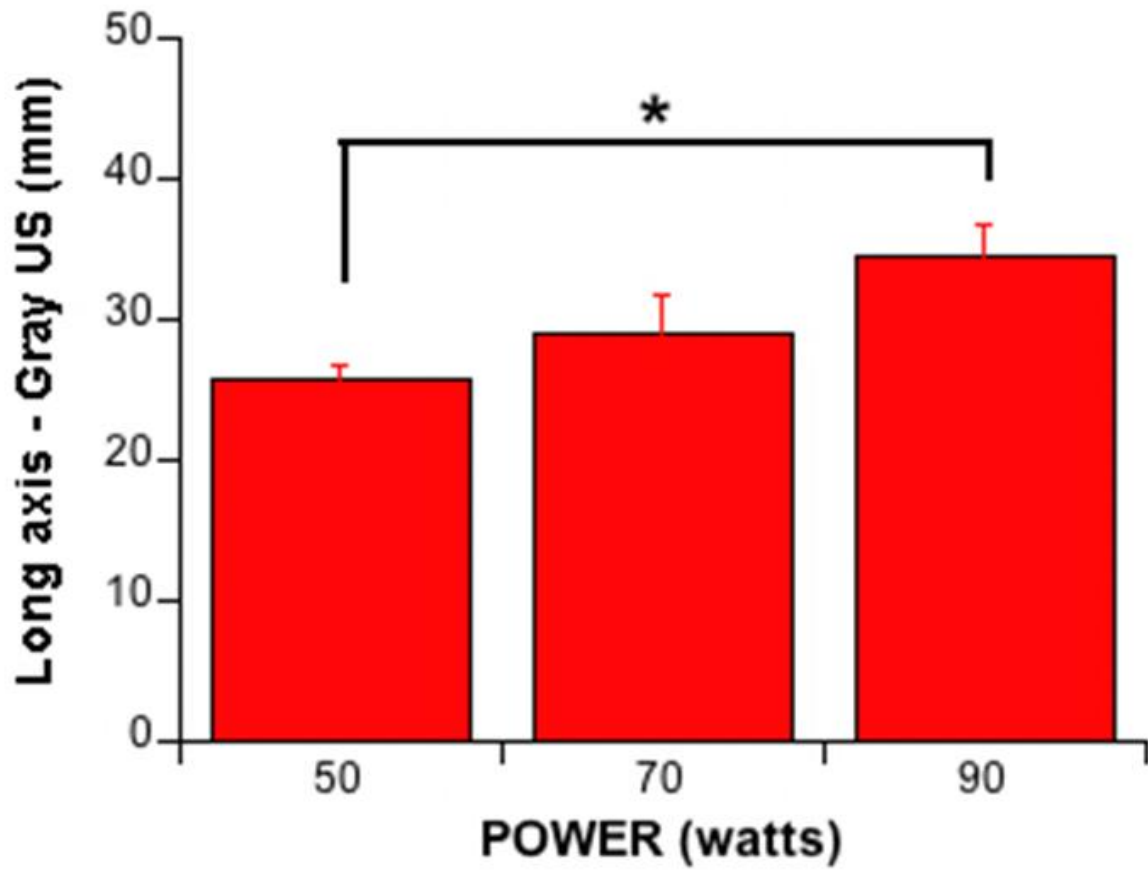


Figure 58. Comparison of the lesion long-axis on grey-scale ultrasound among the three different powers showing the significant difference between power 50W and 90W, $p = 0.05$

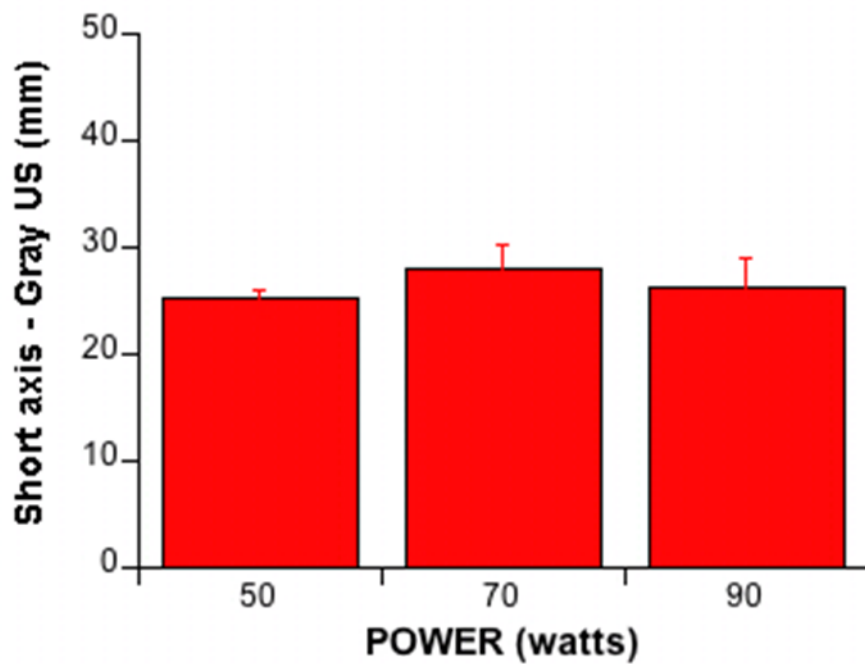


Figure 59. Comparison of the lesion short axis on grey-scale ultrasound showing no differences.

CEUS:

All baseline images showed homogenous enhancement of the liver tissue with MBs. The ablations were reported as anechoic with well-demarcated borders separating them from the contrast-enhanced liver parenchyma in the arterial and venous phase [Fig. 57 A, B & C “right panel”]. The ablated areas did not show any contrast in them apart from the probe insertion site. The long-axis mean values for powers 50W, 70W and 90W were (26.2 +/- 1.1mm), (30.7 +/- 2.2mm), (44 +/- 4mm), and for the short-axis were (27.9 +/- 06mm), (30.8 +/- 1.6mm), (31.5 +/- 1.8mm), respectively. There was a significant difference in the long-axis between powers 70W and 90W ($p=0.015$) and a highly significant difference in the long-axis between powers 50W and 90W ($p=0.001$) [Fig. 60]. There was no difference in the short-axis dimensions among the three powers [Fig. 61].

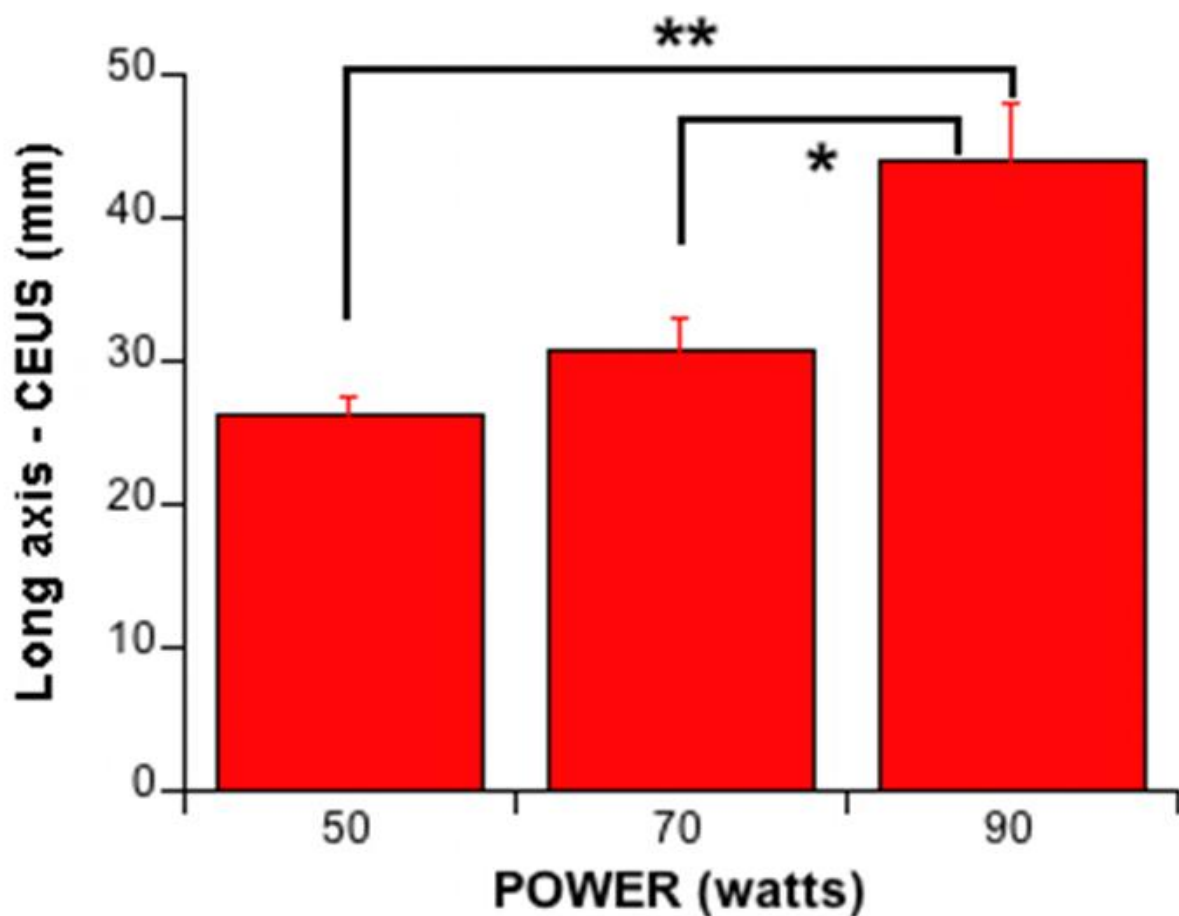


Figure 60. Comparison of the lesion long axis among the three different powers on CEUS showing significant difference between power 70W and 90W ($p = 0.015$), and between power 50W and 90W ($p = 0.0015$).

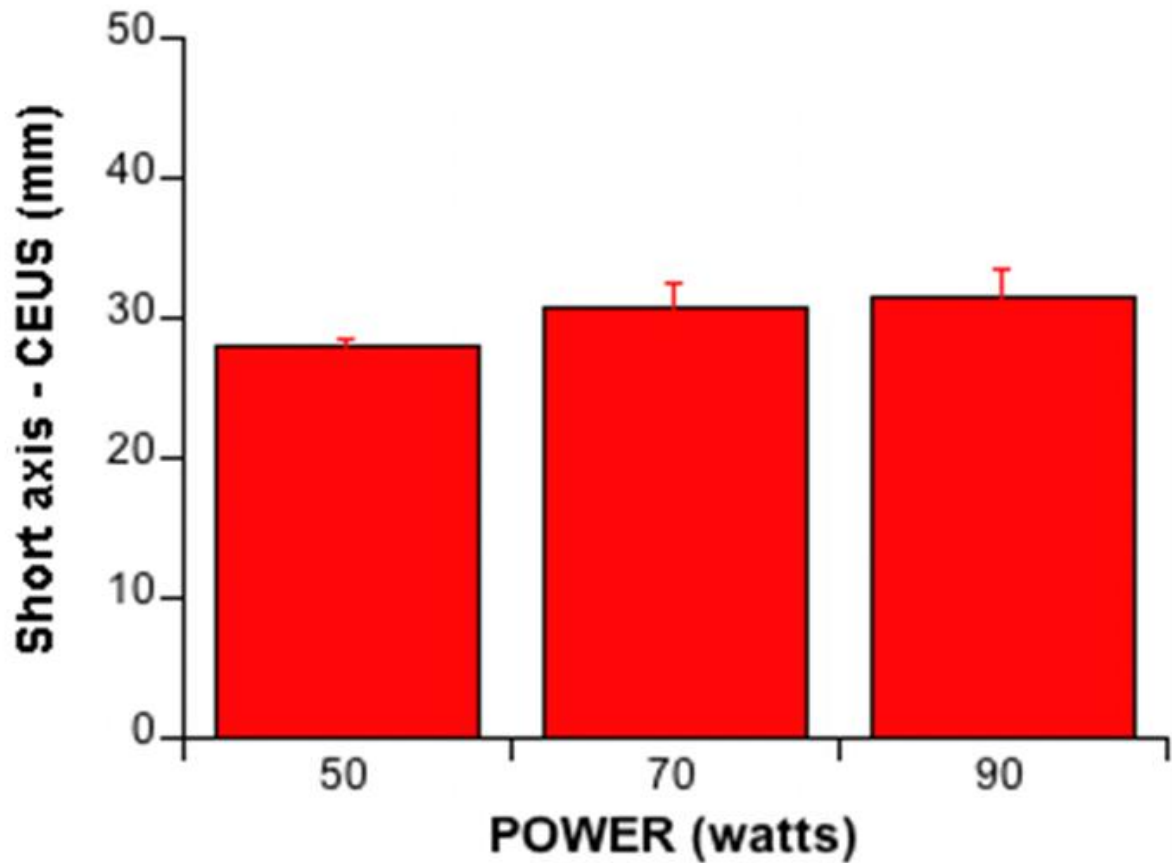


Figure 61. Comparison of the lesion short axis among the three different powers on CEUS showing no differences

Histology:

Gross morphology:

Each lesion consisted of three zones; central charring “black” around the probe insertion site, surrounded by a white pale zone, and then a red-purple perinecrotic zone separating it from the normal looking liver tissue. The zones were all spherical in shape [Fig. 62].

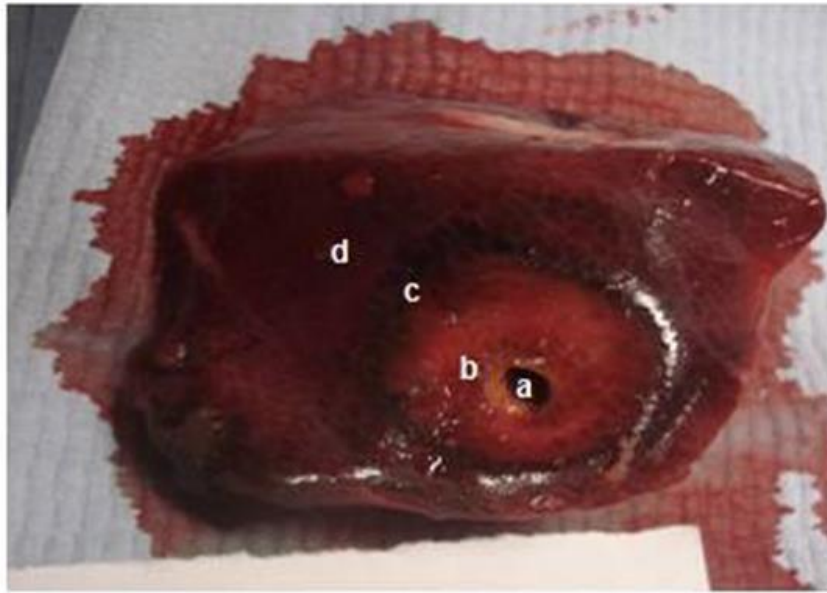


Figure 62. A microwave ablation lesion sample showing the different zones; probe insertion site (a), necrotic zone (b), perinecrotic zone (c) and normal liver tissue (d).

The whole diameter of the lesion was taken including all zones. The long-axis mean values for power 50W, 70W and 90W were (31.7 +/- 3.1mm), (35.18 +/- 1.1mm), (43.3 +/- 3.3mm) respectively, and for the short axis were (28.9 +/- 1.6mm), (30.3 +/- 2.3mm), (32.18 +/- 2.1mm), respectively. There was a significant difference in the long-axis diameter between power 50W and 90W ($p=0.034$) [Fig. 63], but no difference in the short axis diameter [Fig. 64]. The mean values for the perinecrotic zones were (2.3 +/- 0.09m), (2.9 +/- 0.2mm), (2.9 +/- 0.3mm) respectively, with no difference [Fig. 65].

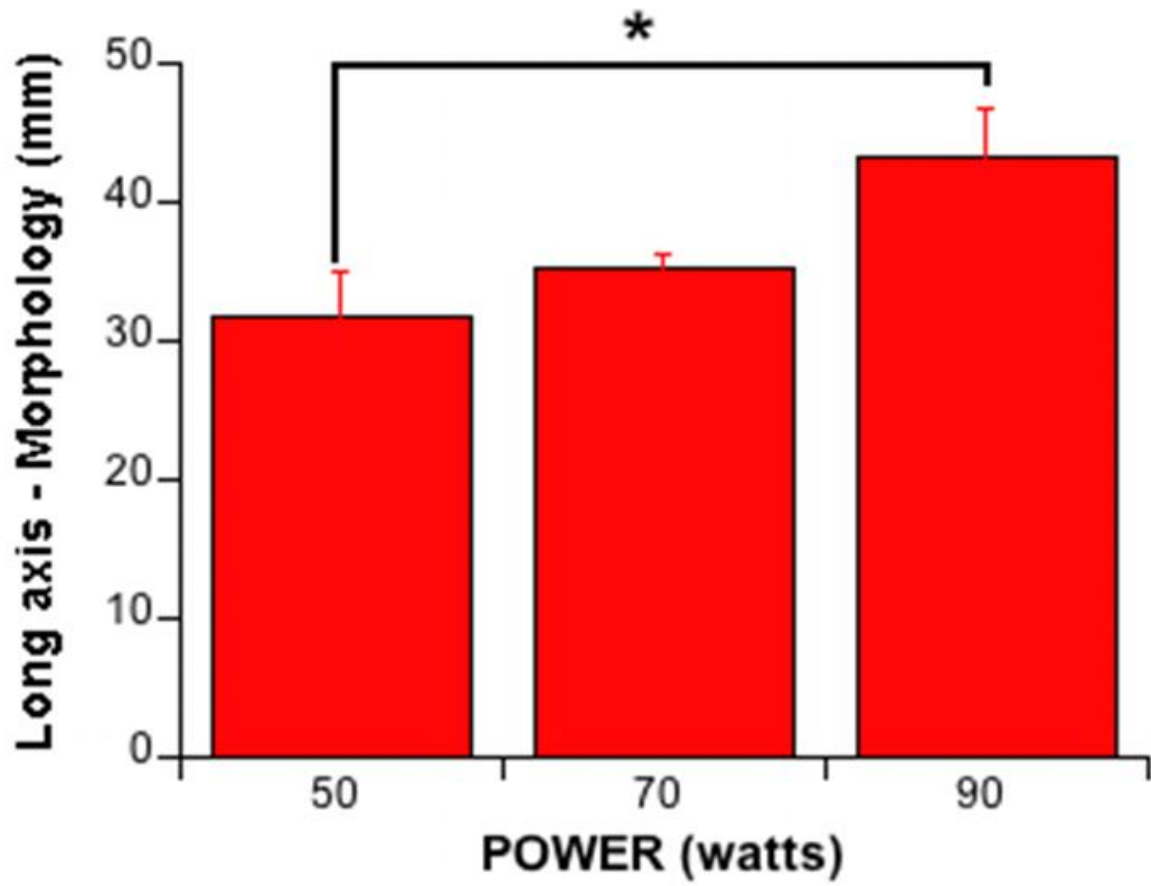


Figure 63. Comparison of the lesion long-axis on morphology among the three powers showing a significant difference between power 50W and 90W ($p=0.034$)

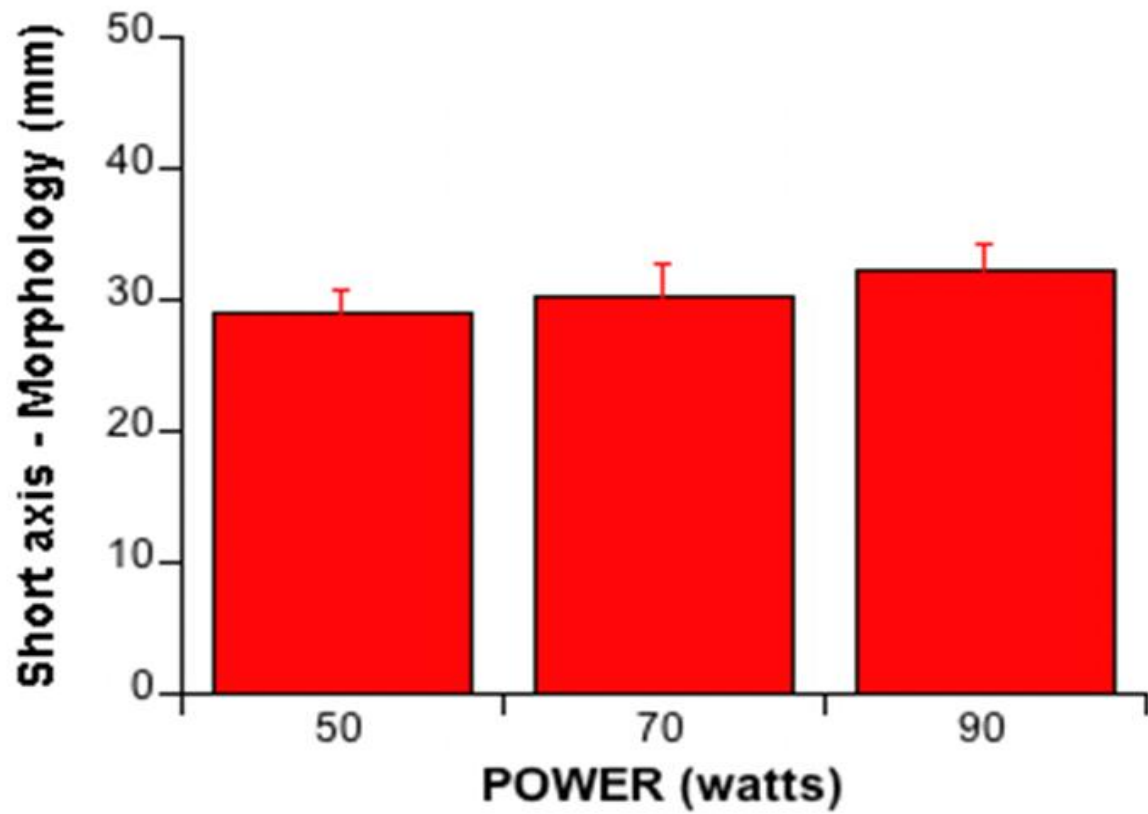


Figure 64. Comparison of the lesion short-axis on morphology among the three different powers showing no difference

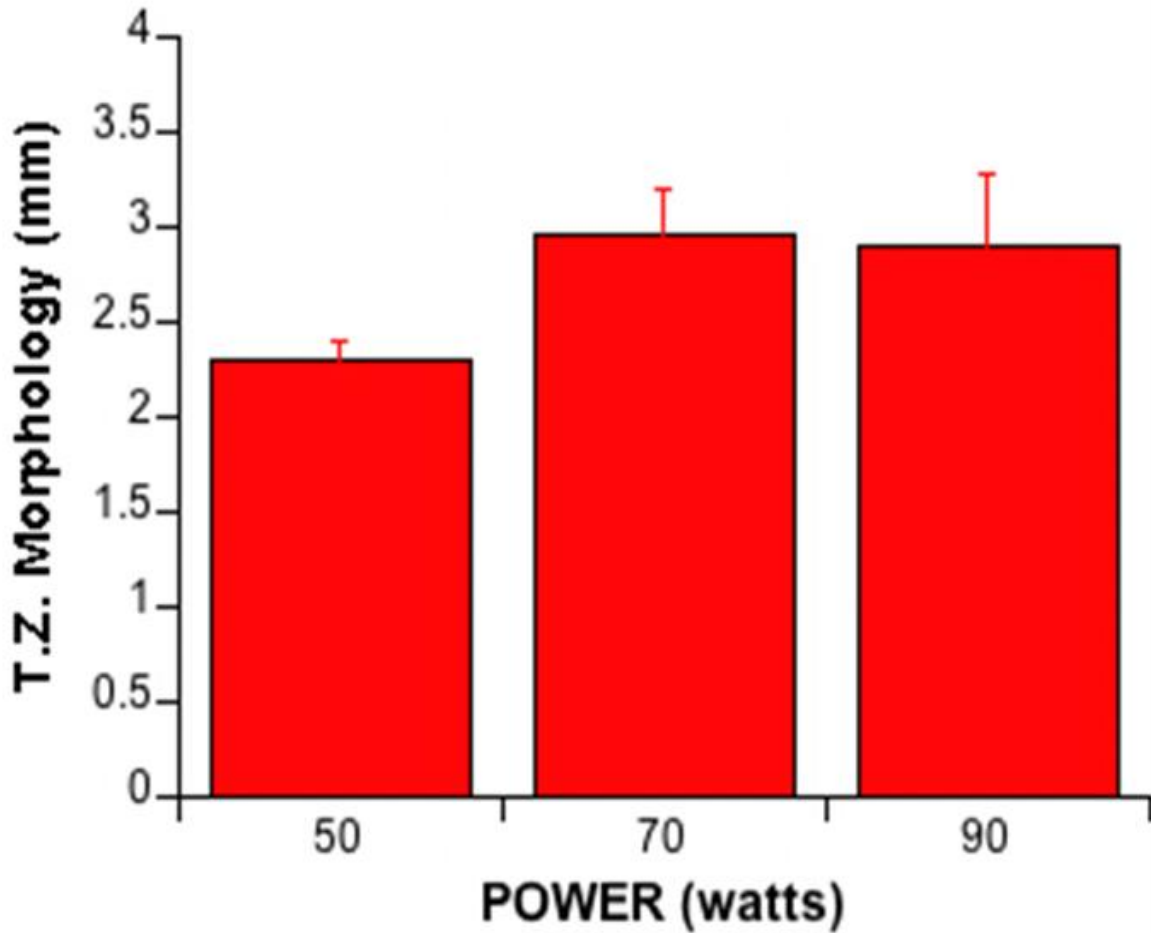


Figure 65. Comparison of the transitional (perinecrotic zone) on morphology among the three different powers showing no difference

Microscopy:

Thermal damage was shown around the probe insertion site with signs of central coagulative necrosis with unrecognizable cell boundaries and collapsed collagen fibres consistent with the white zone [Fig. 66].

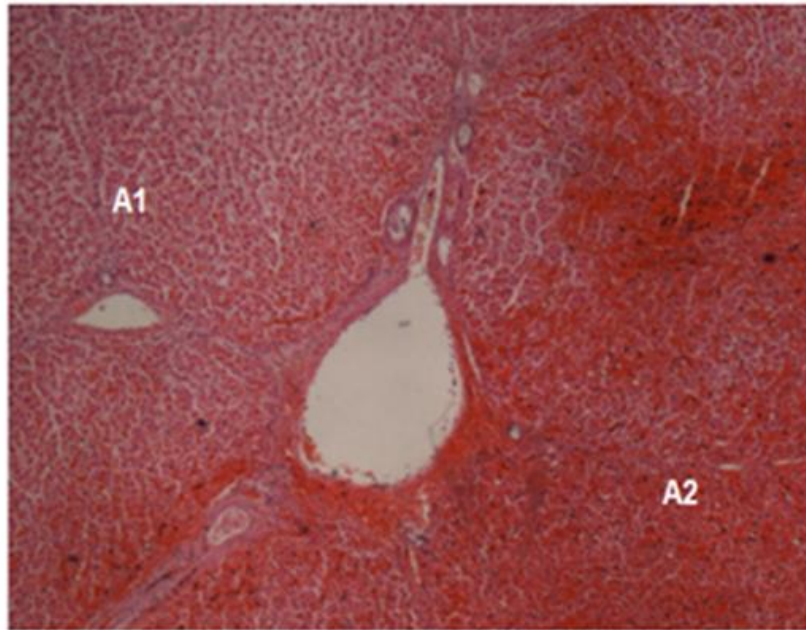


Figure 66. Histological examination of the ablated zone showing central coagulative necrosis (A1) with unrecognizable cell boundaries and collapsed collagen fibres (X 40). Transitional zone (A2)

This zone was surrounded by a transitional zone with signs of vacuolation of hepatocytes, sinusoidal dilatation and haemorrhagic extravasation of red blood cells from the sinusoids into the liver parenchyma, consistent with the red-purple perinecrotic zone on macroscopy [Fig. 67].

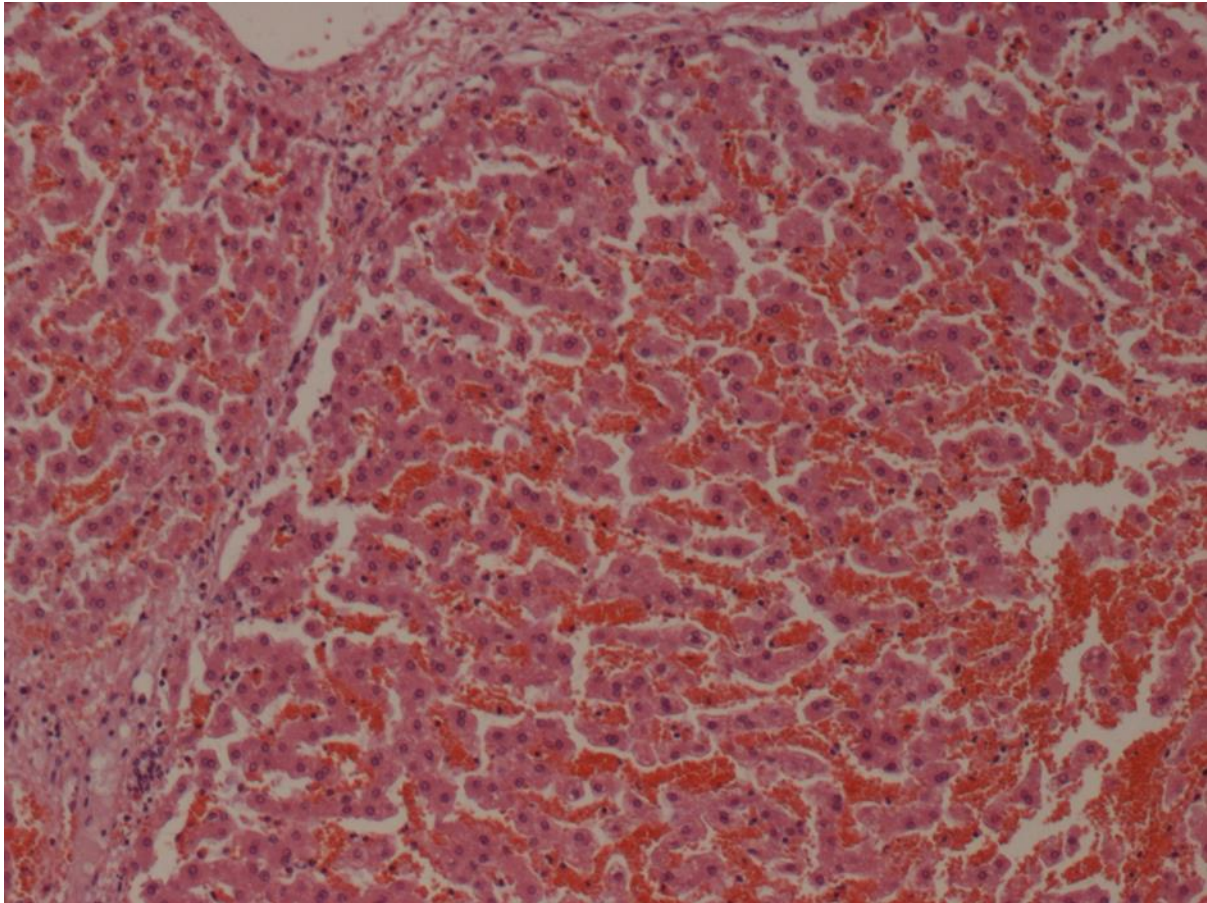


Figure 67. Histological examination of the transitional zone showing vacuolation of hepatocytes, sinusoidal dilatation and haemorrhagic extravasation of red blood cells from the sinusoids into the liver parenchyma (X 100)

The mean values for the transitional zone width for powers 50W, 70W and 90W were (0.4 \pm 0.02mm), (0.5 \pm 0.06mm), (0.6 \pm 0.02mm), respectively. There was a significant difference in the dimensions between powers 50W and 90W ($p = 0.015$) [Fig.68].

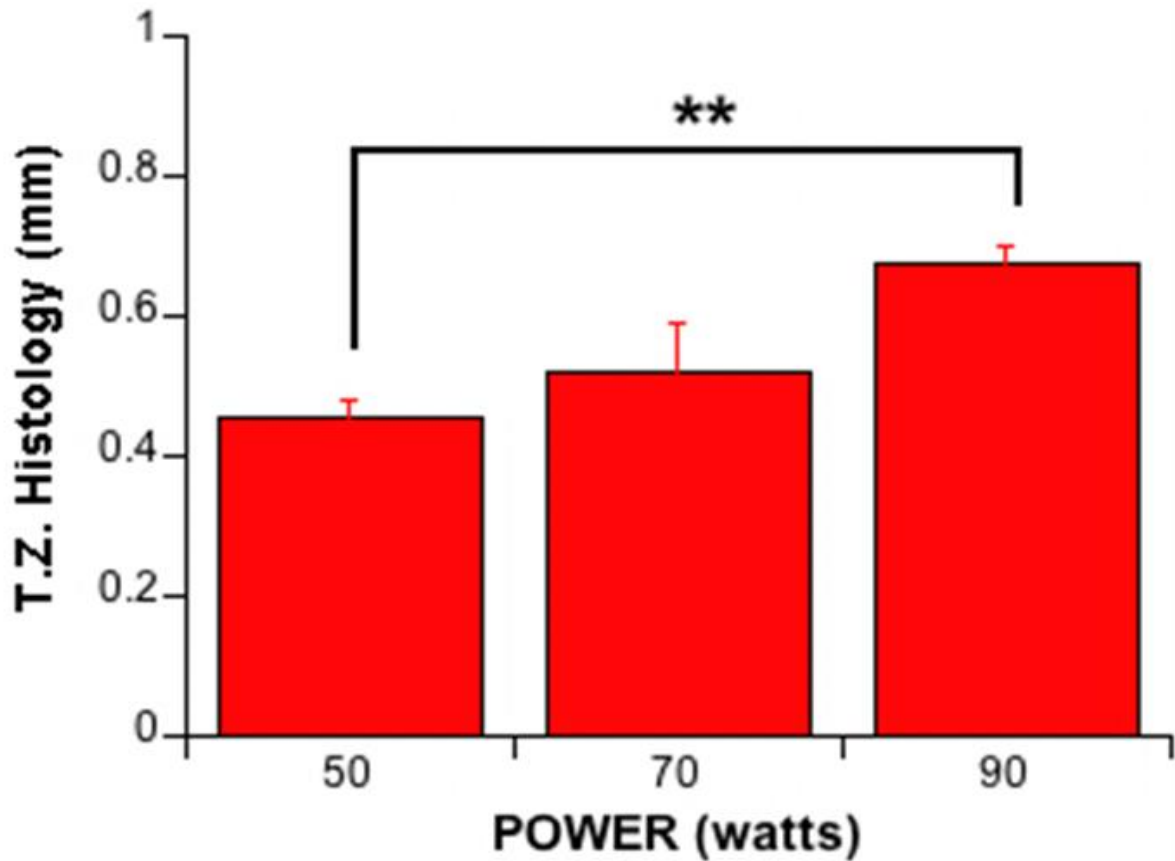


Figure 68. Comparison of the transitional zone width on histology among the three different powers a significant difference in the dimensions between powers 50W and 90W ($P = 0.015$).

Data comparison:

There was a significant difference between the long axis of the ablations on morphology, grey-scale US and CEUS ($p < 0.0001$). There was also a significant difference in the lesion size between powers ($p < 0.0064$) [Fig. 69]. There was no difference in the short-axis for the ablations on morphology, grey-scale US and CEUS, but there was a significant difference in the lesion size between powers ($p < 0.0306$) [Fig. 70].

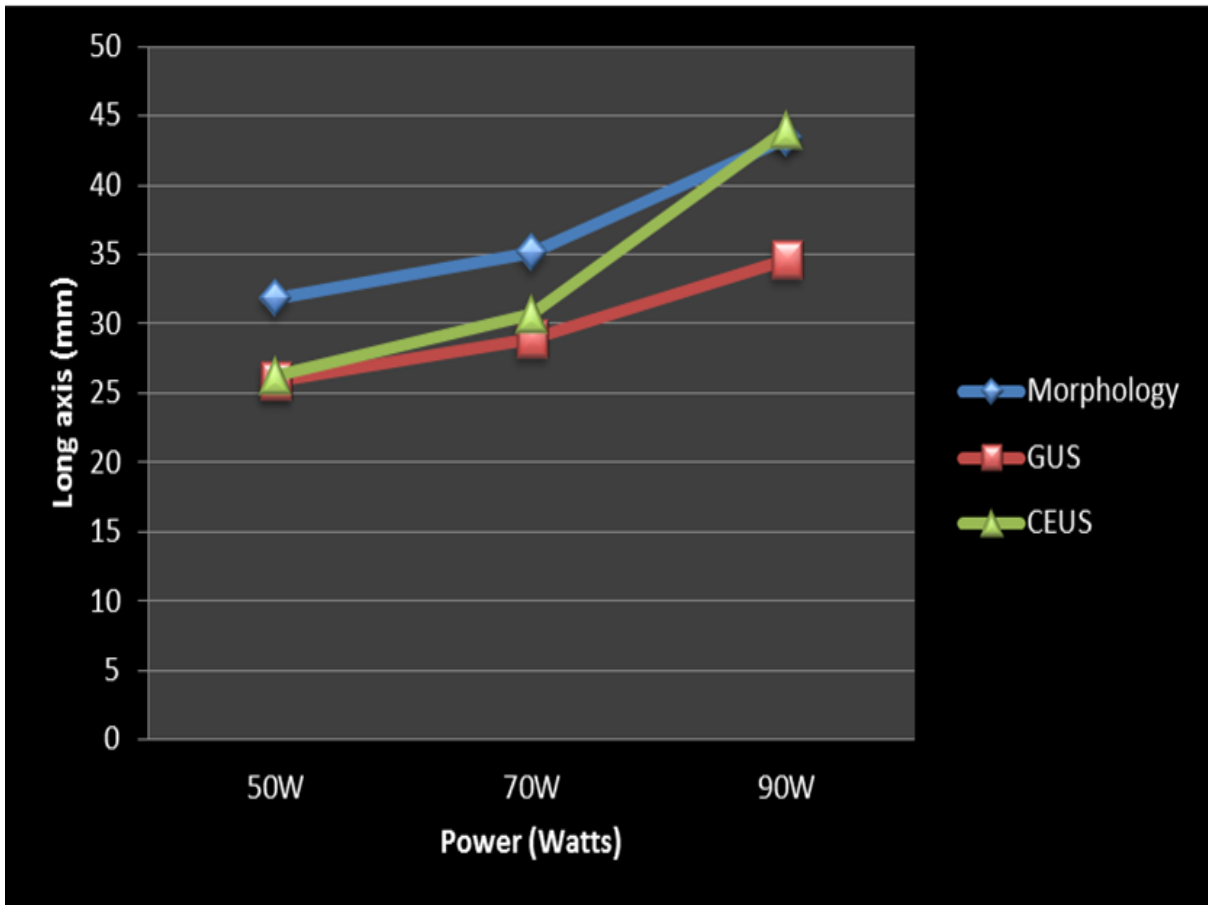


Figure 69. Data analysis (ANOVA test) showing the correlation in the long-axis of the lesion between morphology, grey-scale US and CEUS showing a significant difference ($p < 0.0001$) and a significant difference in the lesion size among powers ($p < 0.0064$).

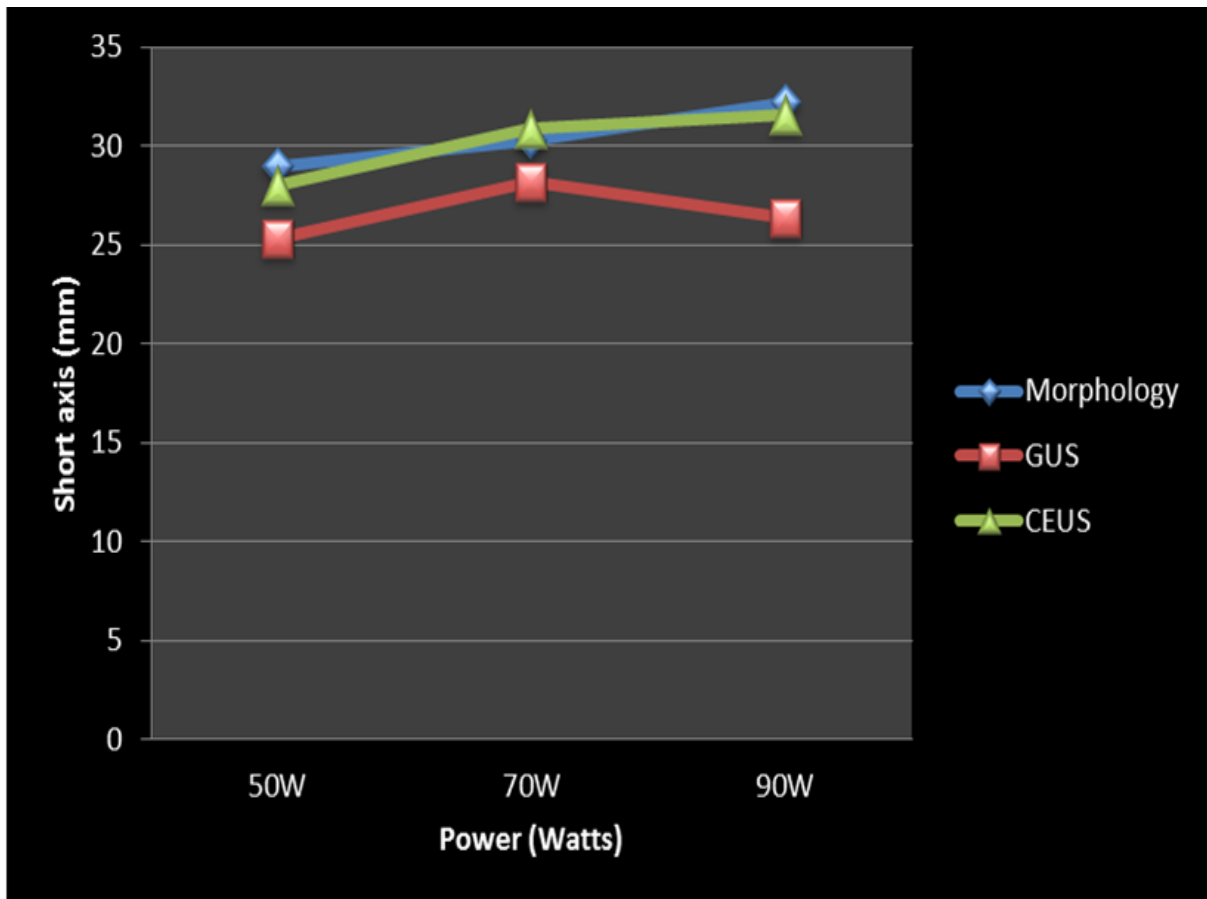


Figure 70. Data analysis (ANOVA test) showing the correlation in the short-axis of the lesion between morphology, grey-scale US and CEUS showing no difference. There is a significant difference in the lesion size among the powers ($p < 0.0306$).

Quantification of the MBs in the ablated area:

The whole ablated areas (centre and periphery) did not show signs of enhancement with MBs during the “Wash in” and “Wash out” phases and all curves were flat, corresponding to the central necrotic and perinecrotic zones (due to stasis), while the healthy perfused liver tissue around the ablations showed homogeneous enhancement [Fig. 71].

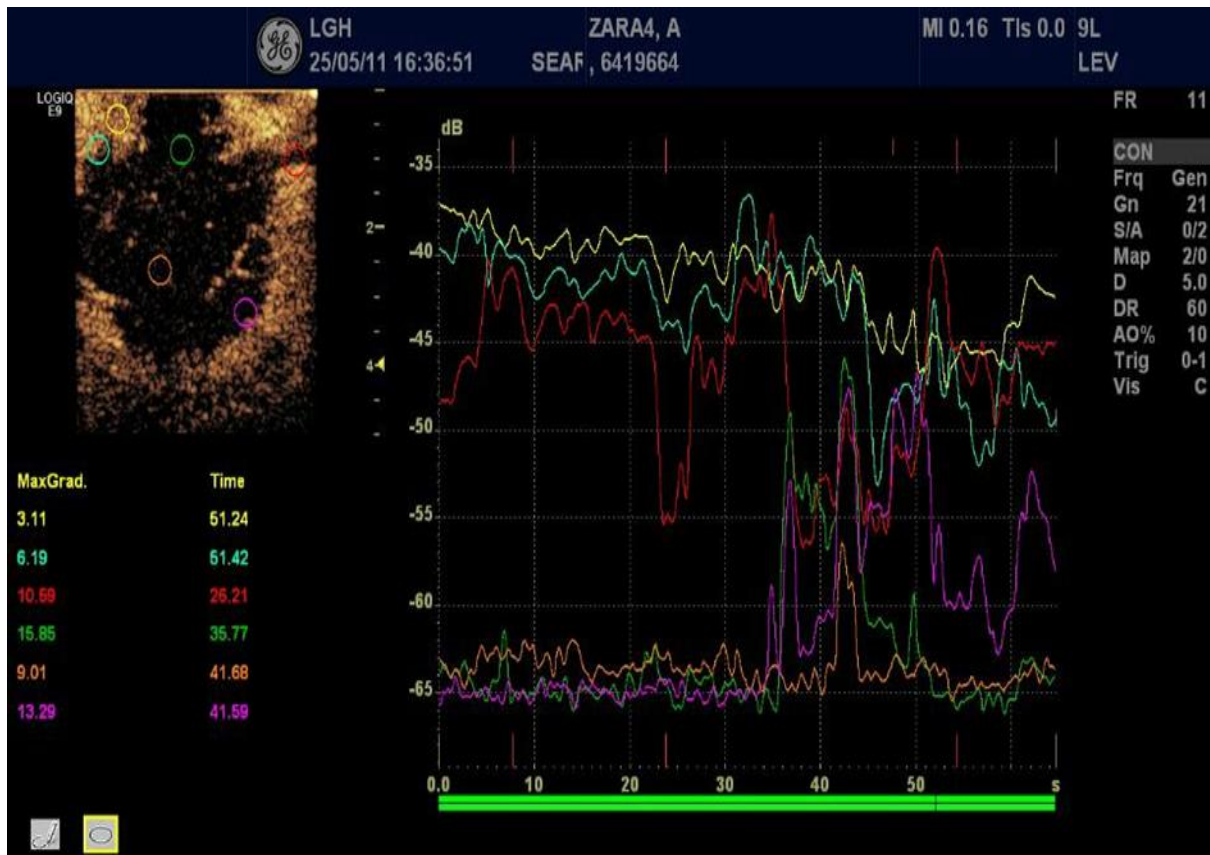


Figure 71. An example of the quantification of the MBs in the ablated area showing different time–intensity curves. The flat (orange, green and purple) curves correspond to the necrotic area with no perfusion. The (yellow, blue and red) curves correspond to the perfused normal liver tissue during “Wash in” and “Wash out” The coloured circles in the left upper panel represent the regions of interest (12–18 mm) where data were sampled during the contrast administration (colour figure online).

Discussion:

Due to its flexible approach (laparoscopic, percutaneous, with open surgery), MWA has become of the new trends for treating liver cancer (38, 281, 282). Its advantages over other thermal ablative techniques include higher intratumoural temperatures, faster ablation times, improved heating of cystic lesions, less procedural pain as it does not require the placement of grounding pads, and is less susceptible to heat sink which means consistency in the size and the shape of the ablated zone (40, 43, 275).

These advantages have made MWA a useful technique for treating primary liver cancer and secondary metastases. Primary liver cancer is the sixth cancer worldwide with hepatocellular carcinoma (HCC) accounting for 70%-90% of the total incidence (283, 284). MWA can be performed under CT, MRI or US guidance. US-guided MWA is more convenient as it allows scanning body in different positions, does not involve radiation and is less costly (30, 35, 59). On the other hand, US does not always show tumour target because of its texture or even differentiate residual tumour from the treated area after ablation (48, 285, 286). The

recommended guideline of ablation is to destroy cancerous lesions with a normal tissue circumferential safety margin of 5mm to 10mm to make sure that the whole lesion is treated (45, 287). After thermal ablation of a tumour, a hyperaemic rim appears which surrounds the ablated area (46, 47). The rim is not visible on grey-scale US, but contrast CT, MRI and CEUS show this rim as uniform, homogeneous, larger than the initial lesion in benign tumours, and irregular, with a size similar to the initial cancerous lesion if the ablation is not complete (45, 48). Irregular borders mean that residual cancer might still exist as some cancer cells escape heat causing local recurrence. By definition, residual tumour is the hyperenhanced area in the ablated area in the arterial phase, with portal and late wash-out (48). This means multiple reinsertions of the probe may be required to achieve complete destruction of the lesion, prolonging operation time, risking exposure to radiation or even causing unnecessary damage to normal tissues around the lesion (288). Grey-scale US lacks the capability of showing targets clearly during treatment because of the generated steam from the ablation which obscures the view (126, 287). The steam creates a problem with differentiating healthy from necrotic tissue “especially in patients with borderline liver volume and function”, identifying lesions in difficult anatomic positions which can only be treated with a probe, or even inserting the probe for overlapping burns (43, 45, 287).

CEUS allows imaging of liver tissues in real-time (arterial phase, venous phase and parenchymal phase) (45, 286). It also guides viable tissue, avoids necrotic areas, evaluates the therapeutic effect immediately post-procedure, and possible reintervention in case of partial response (48). In their study on 25 patients who underwent ablation of hepatic tumours, Andreano and colleagues (46) suggested including the enhanced peripheral rim to achieve complete ablation of tumours. They assessed the lesions with CEUS and found a highly significant difference ($p < 0.0001$) in the lesion size before and during the arterial phase of contrast enhancement. Meloni, *et al* (45) assessed the diagnostic accuracy of CEUS immediately after ablation, after 24-h, and compared it with the diagnostic accuracy of CT after 24-h and then with both imaging methods after 3 months. They evaluated 55 tumours in the liver (37 treated with RFA and 18 with MWA) in 53 patients and concluded that the immediate postprocedural CEUS was comparable to 24-h CEUS and CT in terms of detecting residual disease. In a pilot study on twenty one patients with known hepatic lesions, contrast-enhanced intraoperative ultrasound (CE-IOUS) detected additional 4 lesions and helped change management in three patients (280).

In this study, although CEUS did show better demarcation of the lesions in the images when compared with grey-scale ultrasound, when ANOVA test was performed, there was a significant difference in the long-axis among morphology, grey-ultrasound, and CEUS. The same test did not show a significant difference in the short-axis when all evaluation modalities were compared. These results suggest that CEUS in this study is not superior to grey-scale US or morphology in the assessment of the lesion size. A possible explanation for that could be the small sample size. Lesion dimensions did increase with increasing powers, but this not a new discovery, and the results match what has been published by other investigators.

Microscopic examination of the lesion did show an increase in in the width of the transitional zone with increasing power. The results did not correlate with the width of the perinecrotic red zone on morphology. This means that histology is the only way to properly evaluate the transitional zone, while morphology failed to do so because of the inflammation which masks the picture. This was also obvious with the CEUS which showed a central hypoechoic zone surrounded by the enhanced liver with normal blood flow. The perinecrotic zone was not visible due to stasis which is caused by the inflammatory process.

Limitations of the study:

There were some limitations to the study. First: the small number of experiments. Second: the short life span for the ex vivo model which could be kept live for a maximum of six hours only in order to achieve convincing results. Third: evaluation of benign tissue ablation only as there was no cancer involved. Fourth: the absence of other interacting organs which have an important effect on liver physiology which influences data.

Conclusion:

My results match the previous studies which showed similar correlation between power and lesion size, and histological characteristics of the ablated zones. There is better demarcation of the ablated zone border with CEUS when compared with grey-scale US, an advantage that could be very useful if it was to be implemented in clinical practice to immediately aid lesion evaluation post MWA therapy. On the other hand, CEUS does not reflect the actual size of the lesion when compared with grey-scale US or morphology. Furthermore, histology remains the only way to reflect the exact width of the transitional zone. Further similar studies are still required to confirm and support our findings.

Chapter Five

Increasing Microwave ablative power enhances Apoptosis Expression in an ex-vivo liver perfusion model

Abstract:

Background:

Apoptosis or programmed cell death has been shown to occur as a delayed or indirect cellular response to microwave ablation of tumour and may help eradicate cancer cells that survive the applied heat. However, the extent of its expression in relation to the power applied is yet to be defined. I therefore investigated whether the ablation power used made any difference to the expression of apoptosis in the ablated and normal tissue in a porcine liver perfusion model.

Method:

Biopsies were taken from the MWA lesions created with 50W, 70W and 90W in chapter five experiments (see page 107) and assessed with Haematoxylin-Eosin (HE) and immunohistochemically with Caspase 3 and M30 for apoptosis in each of three zones: a central necrotic zone (“CNZ”) in the path of the microwave, a penumbra transitional zone (“TZ”) around this and a surrounding zone of normal tissue (“NZ”). Statistical analysis was performed using AVOVA and t-test to detect differences in the expression of apoptosis in these zones.

Results:

None of the CNZ showed expression of Caspase-3. In the TZ, there was significant difference between 50W and 90W ($p=0.009$), but not between 50W and 70W ($p=0.8$) or between 70W and 90W ($p=0.4$). In the NZ, a highly significant difference was also noted between 50W and 90W ($p=0.003$), a significant difference between 50W and 70W ($p=0.01$), but not between 70W and 90W ($p=0.06$). For M30, no expression of M30 was noted in CNZ while in TZ, significant difference was noted between 50W and 90W ($p=0.02$). In the NZ, there were no significant differences in the expression of M30 between 50W and 70W ($p=0.4$) or between 70W and 90W ($p=0.07$).

Conclusion:

Increasing the power delivered enhances apoptosis in the transition zones of microwave-ablated areas in this model. This biological response may help in eradicating cancer cells that escape the heat in the ablated zones in the clinical setting.

Introduction:

Minimally invasive ablative modalities for in-situ treatment of early-stage tumours have been of increasing clinical interest recently. These modalities include ethanol ablation, cryoablation, laser ablation, focussed ultrasound (FUS), Radiofrequency and more recently, microwave ablation (MWA) (55). MWA occurs at characteristic frequencies of between

300MHz and 300GHz, which lies between radio and infrared bands on the electromagnetic spectrum. Clinically, a given thermoablative energy dose is delivered to a target, usually a tumour, under US or CT guidance (278). The energy in MWA alternates the polar electric charge in water molecules (H₂O) in the tissues, causing agitation of, and thereby friction between the molecules to generate heat. The frequency with which the charge in the H₂O molecules alternates depends on the frequency of microwave energy used, but is of the order of $2\text{-}5 \times 10^9$ times per second (23). The supraphysiological temperature rise in the surrounding tissues leads to changes at a molecular, cellular and macro-histological level, resulting initially in a coagulative necrosis of tissues in the immediate path of the ablative energy. This necrotic zone is separated from the normal tissue by a transition zone where a delayed and indirect apoptotic response of a variable degree occurs. This response is of potential therapeutic and prognostic interest in the elimination of neoplastic cells and prevention of tumour recurrence (289).

At the time of this study, published in-vivo and ex-vivo work on MWA has focused on characterising its tumour ablation potential and ability to cause cell necrosis in relation to changes in the wavelength of the microwave energy used. Wei, *et al* (290) compared the necrotic effects of wavelengths of 915MHz and 2.45GHz, energy application time and power used in watts, of between 45W to 60W, and 60W to 180W. The aim of my study was to find out if the degree of apoptosis correlated with the applied MWA power in a porcine liver perfusion model to provide a basis for further studies in animal tumour model. To my knowledge, no similar experiments have been published in the literature

Method:

Specimens:

Control biopsies were collected from the paraffin-embedded sections from chapter five experiments (seven biopsies for each power; 50W, 70W & 90W, total=21) [Fig. 72].



Figure-72. Paraffin-embedded sections from ablated areas with different powers (seven sections for each power; 50W, 70W & 90W, total=21)

Antigen retrieval:

The specimens were cut onto Vectabond slides, Dried at 37°C overnight and were then heated at 65°C for 10 minutes, deparaffinised through xylene, rehydrated through graded alcohols (99% Industrial Methylated Spirits “IMS” and 95% IMS) and then rinsed in tap water for five minutes. The slides were then placed in a plastic slide rack, in a plastic dish which was then topped with 10mM Sodium Citrate (pH 6.0). The dish was then microwaved at 80% power for 20 minutes and was then left to cool slowly in the buffer at room temperature.

Immunohistochemistry assays:

Immunohistochemistry for apoptosis was conducted with the primary antibodies (Cleaved Caspase-3 “Asp 175”, New England Biolabs) and (M30 CytoDeath. Bioaxxess) using the (NovoLink Polymer Detection System), Leica Microsystems. RE7140-CE. The slides were washed with buffer (Blocking Solution - TBS/3%BSA/0.1% Triton-X-100) as a primary antibody diluent. Neutralisation of the endogenous peroxidase was done by using Peroxidase Block for 5 minutes. The slides were then washed in TBS for 2 x 5 minutes, incubated with Protein Block for 5 minutes, washed in TBS for 2 x 5 minutes and were then incubated with optimally diluted primary antibody, then washed in TBS for 2 x 5 minutes, incubated with Post Primary Block for 30 minutes, washed again in TBS for 2 x 5 minutes and incubated with NovoLink Polymer for 30 minutes, washed in TBS for 2 x 5 minutes and developed peroxidase activity with DAB working solution for 5 minutes. The slides were then washed in tap water for 5 minutes and counterstaining with Mayer’s Haematoxylin was done for 30 seconds. Finally, the slides were washed in tap water for 5 minutes and were then dehydrated and mounted in DPX. Apoptotic cells were identified when there was evidence of Caspase-3 and M30 positivity.

Quantitative apoptotic index:

The apoptotic index was expressed as the ratio of the number of hepatic cells with Caspase-3 and M30 positivity out of the total number of nucleated cells in each field (magnification, x40) calculated after counting 5 random microscopic fields for each time point with a 19mm Whipple grid graticule lens (Pyser-SGI LTD) [Fig. 33]. In each field, 100 squares were evaluated for the presence of apoptotic cells. Activated Caspase-3 hepatocytes positive for DNA fragmentation [Fig. 34] and for cytoplasmic activity for M30 [Fig. 35] were counted on the whole sections. The mean counts were expressed as a percentage of the total number of non-apoptotic cells counted in each field.

Results:

Microscopic examination:

Haematoxylin-Eosin staining:

Signs of central coagulative necrosis with unrecognizable cell boundaries and collapsed collagen fibres were seen in the CNZ, surrounded by a transitional zone (TZ) with signs of vacuolation of hepatocytes, sinusoidal dilatation and haemorrhagic extravasation of red blood cells from the sinusoids into the liver parenchyma [Fig. 73].

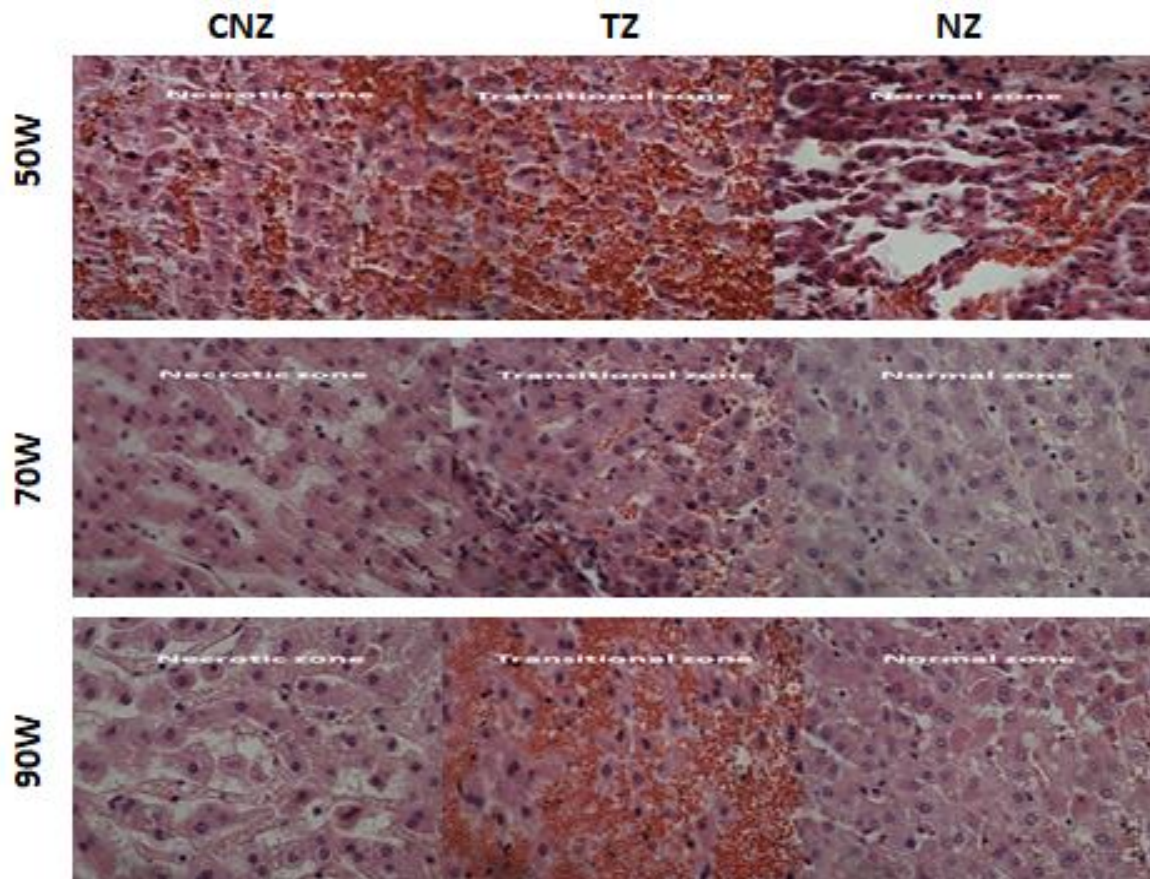


Figure 73. Haematoxylin-Eosin examination of the ablated zone with different powers showing coagulative necrosis with unrecognizable cell boundaries and collapsed collagen fibres in the CNZ (central necrotic zone), vacuolation of hepatocytes, sinusoidal dilatation and haemorrhagic extravasation of red blood cells from the sinusoids into the liver parenchyma in the TZ (transitional zone) & normal hepatocytes in the NZ (normal zone) (X50).

Caspase-3 expression:

None of the samples showed any expression of Caspase-3 in the CNZ with all powers. There was a strong evidence of its expression in all TZ, especially with power 70W, with less expression in the NZ [Fig. 74].

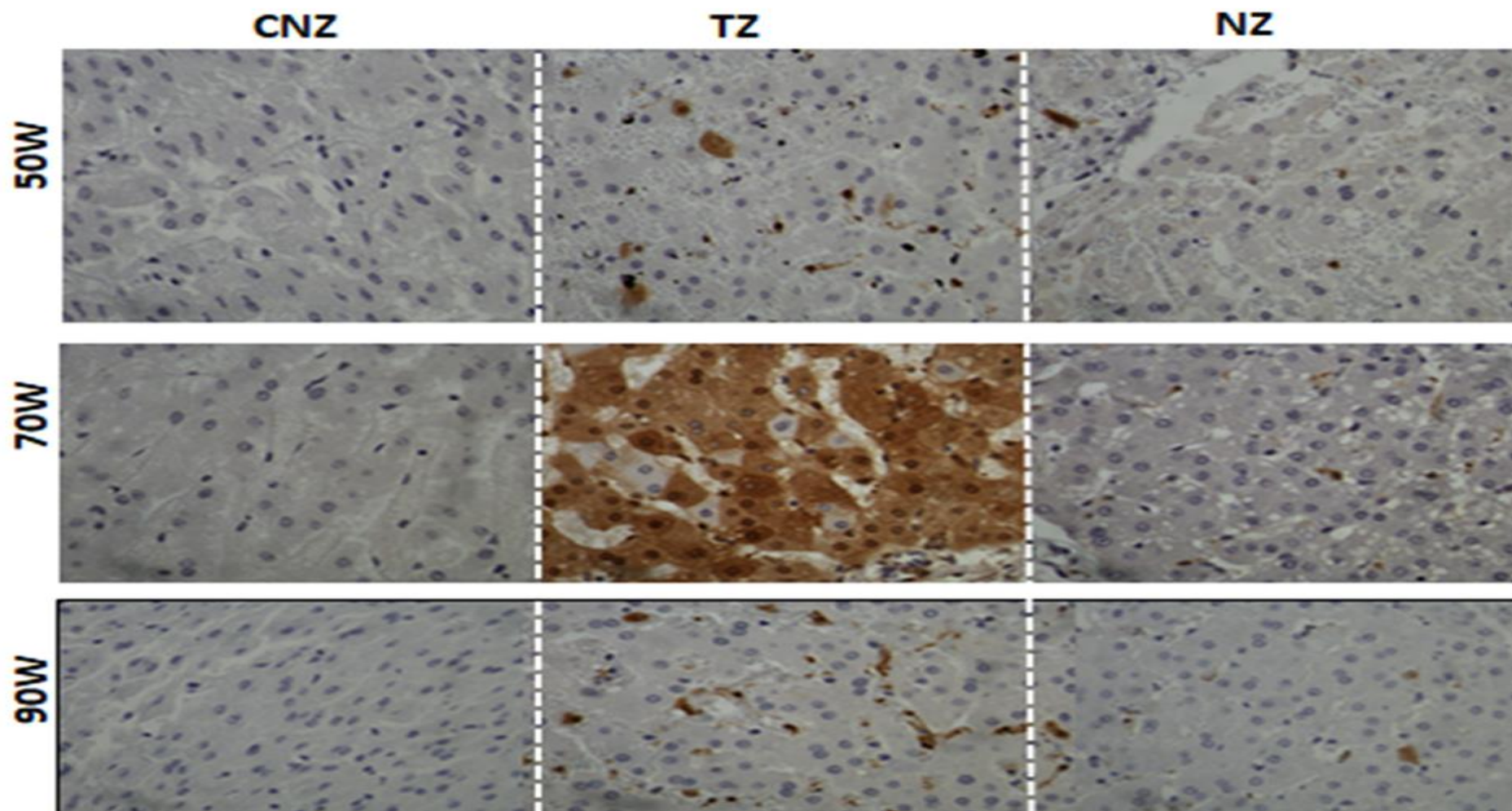


Figure 74. Caspase-3 expression with the three powers (50W, 70W & 90W) in the three zones (CNZ= Central Necrotic Zone, TZ = Transitional Zone, NZ = Normal Zone). (Original magnification x50)

M30 expression:

Different staining of M30 expression was noted in the transitional and normal zones ranging from weak (A), intermediate (B) to strong (C) reactions. There was more expression in the TZ [Fig. 75].

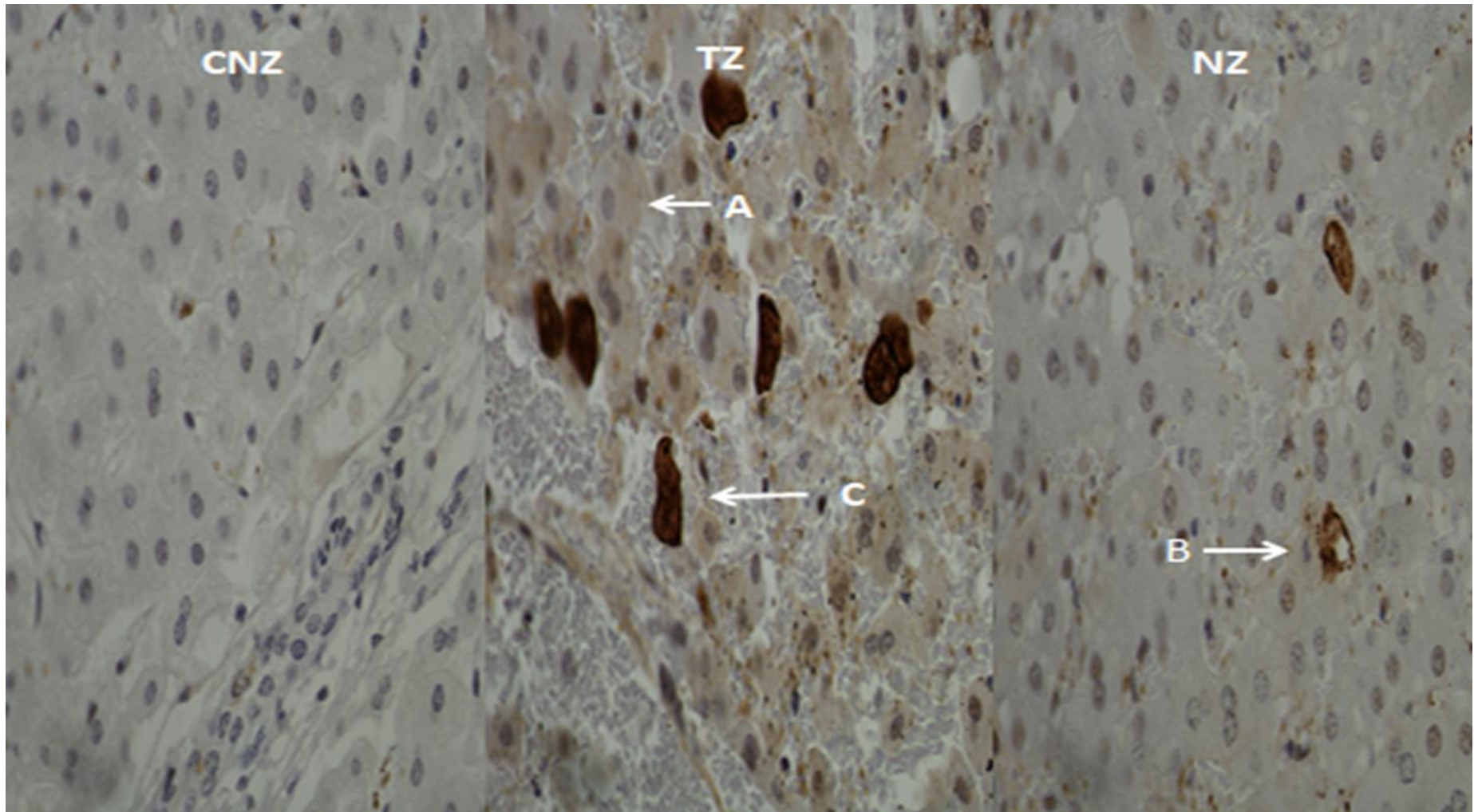


Figure 75. An example of the patterns of staining of M30 expression in the transitional and normal zones ranging from weak (A), intermediate (B) to strong (C) reactions. (Original magnification x50). (change the photo)

Statistical analysis:

Caspase-3 expression:

No expression of Caspase-3 was noted in all necrotic zones. In the TZ, the mean values for 50W, 70W and 90W were (0.28, 0.51, 0.54), respectively. There was significant difference between Powers 50W and 90W ($p=0.009$), but no significant differences between 50W and 70W ($p=0.8$) or between 70W and 90W ($p=0.4$) [Fig. 76]. In the NZ, the mean values were (0.11, 0.17, 0.22), respectively. A highly significant difference was noted between 50W and 90W ($p=0.003$), a significant difference between 50W and 70W ($p=0.01$), but not between 70W and 90W ($p=0.06$).

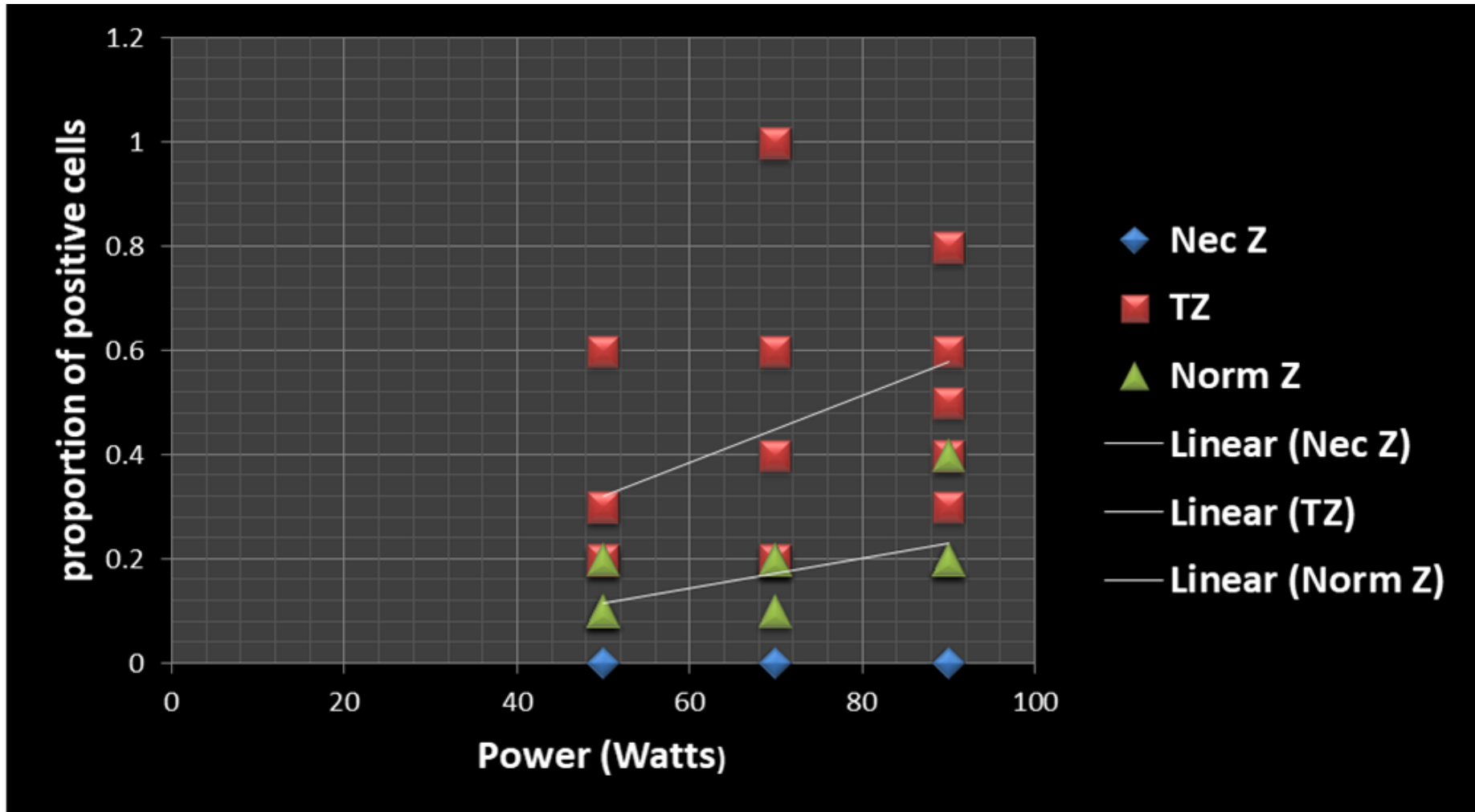


Figure 76. Statistical correlation of Caspase-3 expression among the three zones (CNZ= Central Necrotic Zone, TZ= Transitional Zone, NZ= Normal Zone) with the three applied microwave ablation powers (50W, 70W & 90W)

M30 expression:

No evidence of M30 was noted in all necrotic zones. In the TZ, the mean values for 50W, 70W and 90W were (0.27, 0.29, 0.38) respectively. The only significant difference was noted between powers 50W and 90W ($p=0.02$). There were no significant differences between powers 50W and 70W ($p=0.4$) or between 70W and 90W ($p=0.07$). In the NZ, the mean values were (0.08, 0.08, 0.02), respectively [Fig. 77].

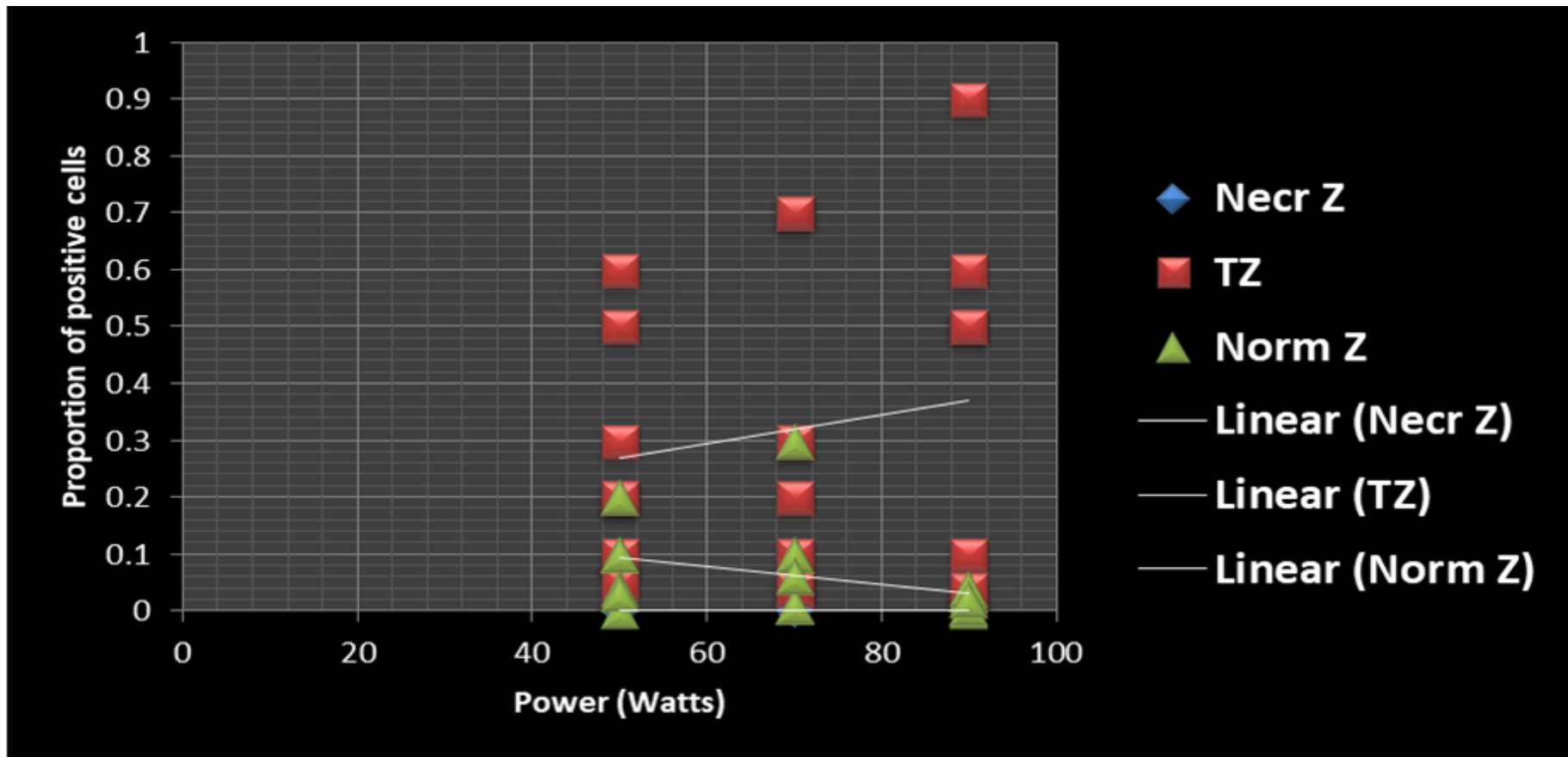


Figure 77. Statistical correlation of M30 expression among the three zones (CNZ= Central Necrotic Zone, TZ= Transitional Zone, NZ= Normal Zone) with the three applied microwave ablation powers (50W, 70W & 90W)

Discussion:

The liver is a particularly suitable organ for isolated perfusion studies of lesions because it has dual blood supply and is a common site for metastasis. Multiple focal ablative methods have been developed and investigated as complementary therapies for primary and metastatic hepatic lesions. These modalities include microwave ablation, high-intensity focused US, laser-induced interstitial thermotherapy, radiofrequency ablation and cryoablation (291). With all forms of thermal ablation therapies there are three distinct zones in heat-ablated lesions: the central necrotic zone (CNZ), which is in the immediate vicinity of the application rod and which undergoes ablation-induced coagulative necrosis; a transitional zone (TZ) of sub lethal hyperthermic injury, which mostly occurs from conduction of heat from the central area and the surrounding normal tissue zone (NZ) that is unaffected by the ablation (292). TZ is of interest as it is either undergoing apoptosis or recovering from reversible injury. It is also the zone where cancer cells may escape the lethal effect of the heat. Four factors determine the extent of cellular damage caused by the heat: the amount of energy applied, the rate of energy delivery, the duration of application and the target tissue's intrinsic thermal sensitivity (293). Previous studies suggest that due to increased cellular density, fewer interstitial vascular and lymphatic channels to dissipate heat and the hypoxic/acidic tumour microenvironment, tumour tissue is more sensitive than normal tissue (294-298).

Ohno, *et al* (22) studied post-MWA apoptosis rates in liver cells as measured by Caspase-3 activity and flow cytometry in TZ at various time points from 0 to 168h. They reported peak activity at 2–6 hours with no evidence of apoptosis in CNZ. Bhardwaj, *et al* (23) reported similar findings and hypothesized that the lack of apoptotic activity in the transition zone at time 0 was likely to be because very little energy had dissipated outside the immediate applicator and central zone and that in addition to other factors such as oedema and local haemorrhage, transition zone cells undergoing apoptosis post-ablation may also account for the increase in macroscopic ablation size observed at 4 and 24 hours.

In my study, when I compared apoptosis at the TZ and NZ using caspase-3 as a marker we observed that there was a marked increase in apoptosis I also noticed an increased apoptosis induction in the NZ at 90W compared to 50W and 70W. When I compared the biopsy samples at the different MWA ablative powers using the M30 marker, I observed a marked increase in apoptosis induction at 90W compared to 50W in the TZ. There were less significant increases of apoptosis at 50W to 70W and 70W to 90W with the peak induction of apoptosis observed at 90W in the TZ. It would seem that a significant power increase is required to induce a parallel increase in apoptosis that reaches statistical significance in this model.

Limitations of the study:

A limitation common to all heat-based ablative models is the so-called heat sink effect (299). This is the centrifugal dissipation of thermal energy by blood flowing away from the ablation zone, preventing the peripheral zones reaching cytotoxic temperatures. This effect potentially reduces treatment efficacy within the TZ where there is increased tumour vasculature. This effect has been observed in the clinical setting, with higher rates of recurrence in tumours adjacent to large blood vessels (300). In this study I have been able to demonstrate that it is

potentially possible to overcome the heat sink effect by increasing the MWA power, which results in increased apoptosis in the TZ and NZ. However it must be noted that the size of the ablation zone with MWA can be harder to predict than other ablative modalities such as RFA (55). Increasing MWA power to escape the heat sink effect could potentially lead to overtreatment and damage to adjacent off-target tissue (300).

Another limitation is inherent in the use of apoptotic index to calculate the extent of MWA induced apoptosis. There is no consensus on the definition and calculation criteria and technical and methodological factors that can influence its determination (301). Some authors use it to denote the number of apoptotic cells per 1000 tumour cells and others have defined it as a percentage of apoptotic cells and bodies per in all tumour cells (302, 303). I calculated the apoptosis index as ratio of all immunohistochemically caspase-3 and M30 stained apoptotic cells out of the total number of nucleated cells in 500 high power microscopic fields.

As samples were taken 6 hours after MWA and no follow up biopsies were taken later, the evolution of apoptosis in the TZ and NZ was not observed. Another limitation was that the duration of ablation was kept the same for all power settings. To obtain the same ablation diameter, the low power settings could have been kept for longer in order to reflect real life scenario. The potential implication of our model for cancer therapy is limited by the fact that I have used a non-cancer model, but it paves the way for future studies using induced or implanted tumour.

Conclusion:

For the first time, I was able to demonstrate the effect of different MWA power settings on the rate of apoptosis in tissues around the zone of ablation. Increasing MWA power enhances apoptosis in the tissue around the periphery of the ablated area in this autologous perfusion model. Further studies are needed to determine if this effect occurs in a cancer model and if this response has potential therapeutic and prognostic benefit for hepatic malignancies.

Conclusions:

In this ex-vivo liver perfusion model, I have investigated the use of CEUS in two types of injury, microwave-induced thermal injury and IRI. In both settings the results show an inverse relationship between the degree of image enhancement and severity of injury. A completely non-enhancing 'black hole' is seen in the area of maximum injury (the 'umbra') and increasing enhancement in the transitional zone centrifugal to it (the 'penumbra'). This transitional zone is of particular interest as tissue is either recovering from the injury or undergoing metabolic changes such as apoptosis. It is therefore potentially targetable for reclamation or destruction if it could be delineated better and early enough. In ex-vivo preparations such as this one, perfusion time is restricted to a maximum of 6 hours, which meant that I could only make meaningful comparisons between the first and fourth hours. In the latter part of this work, I was able to confirm and publish my findings that, using the expression of Caspase-3 and M30 antibodies apoptosis played a significant role in IRI (304), and I was able to quantify it for the first time and relate it to the power of MWA used. As I only took samples at up to 4hrs of reperfusion, I could not assess the extent of apoptosis beyond that point.

To explore the potential clinical application of this part of my work, I used CEUS to assess the size of the MWA lesions that I created as this modality picks up hypoperfused areas (the penumbra or transitional zone) that standard grey-scale colour Doppler US does not. Although histology remains the only definitive way to confirm the extent of the transitional zone, I was able to show a wider area than conventional US.

In this work, I have also used CEUS as an investigative tool, which relies on the ability of MBs to safely enhance US imaging. This type of usage has substantial potential clinical application. Since MBs have an excellent safety profile, the clinician can repeat the imaging as often as necessary. Evidently, MBs can identify hypo-perfused areas of the liver which are at increased risk of reperfusion injury but which Duplex US or other conventional non-invasive imaging modalities do not readily identify. This capability could potentially allow earlier intervention to improve outcome, especially in the field of liver transplantation.

The long gestation period of this work of some nine years does take away from its novelty somewhat, but it also allows further corroborative work to emerge that support the predictions and future directions of this work. In a retrospective study between 2006 and 2015 on 45 liver transplants Rubenthaler *et al* (305) analysed the performance of CEUS in the assessment of vascular complications post liver transplantation and correlated this with histopathology results. They found that CEUS detected vascular complications in the rejected transplants with a sensitivity of 61.5%, specificity of 100% and a positive predictive value of 86.5% (305).

The CEUS images have also been found to tally with elevation of other parameters such as alanine aminotransferase, aspartate aminotransferase, tumour necrosis factor α and interleukin 1β (306). This correlation can provide more information for the early assessment of postoperative complications in transplanted livers as to whether the graft is functioning or non-functioning. However, these parameters need to be monitored pre and post perfusion.

In an in-vivo study to explore the use of CEUS in quantitatively assessing hepatic IRI, Li, *et al* (306) divided 45 rabbits into 3 groups (A, B and C with 15 rabbits each). Group A underwent laparotomy alone, while B and C, hepatic blood was blocked for 30 minutes, and group C underwent left lateral lobe resection. The three groups were assessed by CEUS in a time-dependant manner (after 30 min of ischemia, 0 h, 1 h, 6 h and 24 h. Serum AST and ALT were also monitored pre and post ischaemia. They found that the pathological changes such as inflammatory cell aggregation, erythrocyte destruction and leukocyte infiltration were in accordance with the increased AST and ALT levels as the ischaemic time increased.

Apoptosis has been shown to play a part in the mechanism of injury in IRI (7), but it has also been suggested that there is no method that can accurately assess the extent of apoptosis or differentiate between apoptotic and necrotic cells (118, 122).

A predictable application of this work is in the field of minimally invasive MWA tumour ablation interventions. CEUS can be used to better delineate the field of ablation than conventional grey scale US. Corroborative work by Francica, *et al* (307) characterized the use of CEUS to guide ablation of hepatic tumours which were undetectable or incompletely ablated when grey-US was used. They reported that CEUS improved the ablation rate when compared with the grey-US alone. A similar study by Yan, *et al* on one hundred patients with primary liver cancer compared MWA when used with grey-US versus CEUS. Their results showed that the lesions measured by CEUS were significantly larger than those measured with grey-scale US. The success rate was also reflected in the lower incidence of postoperative pain, fever, intra-abdominal haemorrhage and infection and lower tumour recurrence when compared with similar complications when grey-US was used.

The 3D-CEUS has a promising potential in the assessment of rare liver tumours too. So far, the low incidence rate and the lack of symptoms or biochemical indices of rare liver tumours makes their preoperative imaging assessment limited, and therefore, histology remains the gold standard method to differentiate between malignant and borderline types (308). However, Li, *et al* (110) concluded that using of fusion imaging technique could be as effective as surgical resection. They ablated 12 histologically confirmed rare liver tumours using intra-operative CT/MRI-CEUS or 3D US-CEUS fusion imaging assessments achieving a 100% success on the postoperative CECT/MRI with no complications. Furthermore, no local tumour progression was seen in the 13-month follow up period. Although their results seem promising, the sample size was too small to justify its success on the bigger scale.

Another potential clinical implication of this work is to allow earlier and more accurate mapping of areas of early ischaemia in the liver (“apoptosis map”). In this way the clinician may be better informed in not only assessing extent of liver injury, but also in inducing it in a targeted area as a strategy. The map can also allow assessments of efficacy of on-going treatment of hepatic malignancies to be made. Identifying apoptosis can also help monitor the treatment, where the aim is to induce apoptosis in cancer cells. A corroborative sentient work in this domain was a study by Xu *et al* (309) who assessed the residual tumour cells in the periphery of 90 rabbit hepatic tumours after MWA with MBs, MWA plus US, MWA plus saline and MWA only. They reported higher apoptotic index, smaller tumour growth and

longer survival in the group that received MWA plus MBs when compared with the other groups ($p < 0.05$).

The small sample size in my project limits the generalizability of the results beyond the lesion size and ablation power that I have used. Increasing ablation power leads to increased lesion size and the width of the TZ on histology and parallel increase in apoptosis. My findings also confirm that TZ is better assessed by histology but this is an invasive diagnostic modality.

Future directions of this project:

An interesting and unifying theory by Jaeschke, *et al* (7) propounds a continuum of necrosis and apoptosis ('necroptosis') based on the concept of ATP depletion. This offers the tantalising prospect of identifying potential therapeutic targets in the putative pathway, provided it can be fully elucidated. My work provides a tool for that research and for other perfusion studies on the liver in health and disease.

One possible use of this tool is to be found in the work by Bahadir, *et al* (310) who evaluated the protective effect of quercetin in hepatic ischaemia-reperfusion injury. Quercetin is a liposome found in fruits and vegetables and has been shown to have antioxidant, anticarcinogenic, antiaggregatory and anti-inflammatory effects (310). They performed laparotomies on 24 rats after dividing them into three groups (group A: laparotomies only, group B laparotomies with hepatic ischaemia by clamping the hepatic pedicle, group C were given intraperitoneal quercetin injection prior to clamping the hepatic pedicle). The total oxidant status, total antioxidant status levels and apoptotic index were measured. On comparing the three groups, there were significantly less vacuolization and sinusoidal dilatation and more apoptosis in group C. Although the conclusion was that quercetin might have a protective effect against ischaemia-reperfusion injury, the authors did not mention the ischaemia time in their experiments which can bias their results. In my project, I did demonstrate that the apoptotic index increased in a time-dependant manner. Therefore, their study paves the way for further research to fully evaluate the role of quercetin in similar cases with the emphasis on ischaemia time.

Another future direction that can be explored is modulating ablation power to achieve complete tumour ablation and reduce the procarcinogenic effect caused by various inflammatory markers such as interleukin-1b, IL-6, and HSP 70. These markers are expressed in the periablation rim. Their expression differs with the applied thermal dose and its duration. Liu, *et al* (218) have already showed that the expression of HSP70, for example, is increased when MBs are combined with US. HSP-70 has also been shown to have a protective effect against apoptosis (311). The question here is how to reduce HSP-70 expression and increase the apoptotic response in the TZ at the same time to achieve complete ablation?

A promising answer has come from a study by Duan, *et al* (311). They investigated the role of quercetin in enhancing the effect of MWA on hepatic parenchyma destruction. In their study, Duan, *et al* (311) divided 48 rabbits into three groups (group A received quercetin only, group B underwent MWA of the livers and group C were given Quercetin prior to hepatic MWA. The three groups were compared with regard to the expression of HSP-70 and apoptosis among other parameters in the ablated tissues. They reported that HSP-70 was less expressed in group C compared with group B. They also found that the expression of apoptosis was higher in group C when compared with group B. This means that controlling the expression of HSP-70 by quercetin can enhance apoptosis which is required to kill all cancer cells in the TZ. In that study, the researchers used 30W to ablate the livers for 40 seconds. The obvious question here is what power and duration are required to achieve maximum enhancement of apoptosis in the TZ.

Velez, *et al* (312) compared two MWA powers and durations (5W x 2 minutes, and 20W x 15 seconds) in 12 rats (6 rats for each power and time). At day 7 posthepatic MWA, HSP-70 expression in the TZ was lower with 20W power and the short duration compared with the low power and long duration concluding that high power and faster heating protocols may potentially mitigate the undesired procarcinogenic effects caused by HSP-70.

In my project, I used three different powers (50W, 70W and 90W) and I ablated the livers for two minutes. My results showed that the expression of apoptosis was higher with 90W when compared with 50W for the same dwell time. However, I used CEUS to enhance the ablated areas, and MBs do cause apoptosis too. Therefore, further studies should investigate the expression of apoptosis using similar powers with CEUS and US only to control for the contribution of the MBs to the apoptosis.

References:

1. Correias JM, Bridal L, Lesavre A, Mejean A, Claudon M, Helenon O. Ultrasound contrast agents: properties, principles of action, tolerance, and artifacts. *Eur Radiol* 2001;11:1316-1328.
2. Harvey CJ, Blomley MJ, Eckersley RJ, Cosgrove DO. Developments in ultrasound contrast media. *Eur Radiol* 2001;11:675-689.
3. Kaya M, Gregory TSt, Dayton PA. Changes in lipid-encapsulated microbubble population during continuous infusion and methods to maintain consistency. *Ultrasound Med Biol* 2009;35:1748-1755.
4. Rychak JJ, Lindner JR, Ley K, Klivanov AL. Deformable gas-filled microbubbles targeted to P-selectin. *J Control Release* 2006;114:288-299.
5. Lindner JR, Song J, Xu F, Klivanov AL, Singbartl K, Ley K, Kaul S. Noninvasive ultrasound imaging of inflammation using microbubbles targeted to activated leukocytes. *Circulation* 2000;102:2745-2750.
6. Catalano O, Lobianco R, Raso MM, Siani A. Blunt hepatic trauma: evaluation with contrast-enhanced sonography: sonographic findings and clinical application. *J Ultrasound Med* 2005;24:299-310.
7. Jaeschke H, Lemasters JJ. Apoptosis versus oncotic necrosis in hepatic ischemia/reperfusion injury. *Gastroenterology* 2003;125:1246-1257.
8. Wang XH, Qin Y, Hu MH, Xie Y. Dendritic cells pulsed with hsp70-peptide complexes derived from human hepatocellular carcinoma induce specific anti-tumor immune responses. *World J Gastroenterol* 2005;11:5614-5620.
9. Neuman MG. Apoptosis in liver disease. *Rom J Gastroenterol* 2002;11:3-7.
10. Ghobrial IM, Witzig TE, Adjei AA. Targeting apoptosis pathways in cancer therapy. *CA Cancer J Clin* 2005;55:178-194.
11. Honda H, Zhao QL, Kondo T. Effects of dissolved gases and an echo contrast agent on apoptosis induced by ultrasound and its mechanism via the mitochondria-caspase pathway. *Ultrasound Med Biol* 2002;28:673-682.
12. Furusawa Y, Zhao QL, Hassan MA, Tabuchi Y, Takasaki I, Wada S, Kondo T. Ultrasound-induced apoptosis in the presence of Sonazoid and associated alterations in gene expression levels: a possible therapeutic application. *Cancer Lett* 2010;288:107-115.
13. Luo W, Zhou X, Zhang J, Qian Y, Zheng M, Yu M, Gong X. Analysis of apoptosis and cell proliferation after high intensity-focused ultrasound ablation combined with microbubbles in rabbit livers. *Eur J Gastroenterol Hepatol* 2007;19:962-968.
14. Feril LB, Jr., Kondo T, Zhao QL, Ogawa R, Tachibana K, Kudo N, Fujimoto S, et al. Enhancement of ultrasound-induced apoptosis and cell lysis by echo-contrast agents. *Ultrasound Med Biol* 2003;29:331-337.
15. Yu T, Xiong S, Mason TJ, Wang Z. The use of a micro-bubble agent to enhance rabbit liver destruction using high intensity focused ultrasound. *Ultrason Sonochem* 2006;13:143-149.
16. Alzaraa A, Gravante G, Chung WY, Al-Leswas D, Bruno M, Dennison AR, Lloyd DM. Targeted microbubbles in the experimental and clinical setting. *Am J Surg* 2012;204:355-366.
17. Wilson SR, Burns PN. An algorithm for the diagnosis of focal liver masses using microbubble contrast-enhanced pulse-inversion sonography. *AJR Am J Roentgenol* 2006;186:1401-1412.

18. Martin RC, 2nd, Reuter NP, Woodall C. Intra-operative contrast-enhanced ultrasound improves image enhancement in the evaluation of liver tumors. *J Surg Oncol* 2010;101:370-375.
19. Minami Y, Kudo M, Hatanaka K, Kitai S, Inoue T, Hagiwara S, Chung H, et al. Radiofrequency ablation guided by contrast harmonic sonography using perfluorocarbon microbubbles (Sonazoid) for hepatic malignancies: an initial experience. *Liver Int* 2010;30:759-764.
20. Boutros C, Somasundar P, Garrean S, Saied A, Espat NJ. Microwave coagulation therapy for hepatic tumors: review of the literature and critical analysis. *Surg Oncol* 2010;19:e22-32.
21. Bartolotta TV, Taibbi A, Midiri M, De Maria M. Hepatocellular cancer response to radiofrequency tumor ablation: contrast-enhanced ultrasound. *Abdom Imaging* 2008;33:501-511.
22. Ohno T, Kawano K, Sasaki A, Aramaki M, Yoshida T, Kitano S. Expansion of an ablated site and induction of apoptosis after microwave coagulation therapy in rat liver. *J Hepatobiliary Pancreat Surg* 2001;8:360-366.
23. Bhardwaj N, Dormer J, Ahmad F, Strickland AD, Gravante G, West K, Dennison AR, et al. Microwave ablation of the liver: a description of lesion evolution over time and an investigation of the heat sink effect. *Pathology* 2011;43:725-731.
24. Nakamoto Y, Kaneko S, Fan H, Momoi T, Tsutsui H, Nakanishi K, Kobayashi K, et al. Prevention of hepatocellular carcinoma development associated with chronic hepatitis by anti-fas ligand antibody therapy. *J Exp Med* 2002;196:1105-1111.
25. Pierce RH, Vail ME, Ralph L, Campbell JS, Fausto N. Bcl-2 expression inhibits liver carcinogenesis and delays the development of proliferating foci. *Am J Pathol* 2002;160:1555-1560.
26. Vick B, Weber A, Urbanik T, Maass T, Teufel A, Krammer PH, Opferman JT, et al. Knockout of myeloid cell leukemia-1 induces liver damage and increases apoptosis susceptibility of murine hepatocytes. *Hepatology* 2009;49:627-636.
27. Jensen JA. Medical ultrasound imaging. *Prog Biophys Mol Biol* 2007;93:153-165.
28. Fischetti AJ, Scott RC. Basic ultrasound beam formation and instrumentation. *Clin Tech Small Anim Pract* 2007;22:90-92.
29. Postema M, Gilja OH. Contrast-enhanced and targeted ultrasound. *World J Gastroenterol* 2011;17:28-41.
30. Coltrera MD. Ultrasound physics in a nutshell. *Otolaryngol Clin North Am* 2010;43:1149-1159, v.
31. Ihnatsenka B, Boezaart AP. Ultrasound: Basic understanding and learning the language. *Int J Shoulder Surg* 2010;4:55-62.
32. D'Onofrio M, Vecchiato F, Cantisani V, Barbi E, Passamonti M, Ricci P, Malago R, et al. Intrahepatic peripheral cholangiocarcinoma (IPCC): comparison between perfusion ultrasound and CT imaging. *Radiol Med* 2008;113:76-86.
33. Hann LE, Bach AM, Cramer LD, Siegel D, Yoo HH, Garcia R. Hepatic sonography: comparison of tissue harmonic and standard sonography techniques. *AJR Am J Roentgenol* 1999;173:201-206.
34. Averkiou M, Powers J, Skyba D, Bruce M, Jensen S. Ultrasound contrast imaging research. *Ultrasound Q* 2003;19:27-37.
35. Aldrich JE. Basic physics of ultrasound imaging. *Crit Care Med* 2007;35:S131-137.
36. Minami Y, Kudo M, Chung H, Kawasaki T, Yagyu Y, Shimono T, Shiozaki H. Contrast harmonic sonography-guided radiofrequency ablation therapy versus B-mode sonography in hepatocellular carcinoma: prospective randomized controlled trial. *AJR Am J Roentgenol* 2007;188:489-494.

37. Shen CC, Yang YC, Chen WS. Optimal transmit phasing for harmonic-background suppression with bipolar square-wave pulser. *Ultrason Imaging* 2010;32:33-47.
38. Simon CJ, Dupuy DE, Mayo-Smith WW. Microwave ablation: principles and applications. *Radiographics* 2005;25 Suppl 1:S69-83.
39. Byrd JF, Agee N, McKillop IH, Sindram D, Martinie JB, Iannitti DA. Colour doppler ultrasonography provides real-time microwave field visualisation in an ex vivo porcine model. *HPB (Oxford)* 2011;13:400-403.
40. Lubner MG, Brace CL, Hinshaw JL, Lee FT, Jr. Microwave tumor ablation: mechanism of action, clinical results, and devices. *J Vasc Interv Radiol* 2010;21:S192-203.
41. Umehara H, Seki T, Inokuchi R, Tamai T, Kawamura R, Asayama T, Ikeda K, et al. Microwave coagulation using a perfusion microwave electrode: Preliminary experimental study using ex vivo and in vivo liver. *Exp Ther Med* 2012;3:214-220.
42. Swift B, Strickland A, West K, Clegg P, Cronin N, Lloyd D. The histological features of microwave coagulation therapy: an assessment of a new applicator design. *Int J Exp Pathol* 2003;84:17-30.
43. Jones RP, Kitteringham NR, Terlizzo M, Hancock C, Dunne D, Fenwick SW, Poston GJ, et al. Microwave ablation of ex vivo human liver and colorectal liver metastases with a novel 14.5 GHz generator. *Int J Hyperthermia* 2012;28:43-54.
44. Vogt FM, Antoch G, Veit P, Freudenberg LS, Blehschmid N, Diersch O, Bockisch A, et al. Morphologic and functional changes in nontumorous liver tissue after radiofrequency ablation in an in vivo model: comparison of 18F-FDG PET/CT, MRI, ultrasound, and CT. *J Nucl Med* 2007;48:1836-1844.
45. Meloni MF, Andreano A, Franza E, Passamonti M, Lazzaroni S. Contrast enhanced ultrasound: Should it play a role in immediate evaluation of liver tumors following thermal ablation? *Eur J Radiol* 2012;81:e897-902.
46. Andreano A, Meneghel E, Bovo G, Ippolito D, Salvioni A, Filice C, Sironi S, et al. Contrast-enhanced ultrasound in planning thermal ablation of liver metastases: Should the hypervascular halo be included in the ablation volume?(). *J Ultrasound* 2010;13:158-163.
47. Marin HL, Furth EE, Olthoff K, Shaked A, Soulen MC. Histopathologic outcome of neoadjuvant image-guided therapy of hepatocellular carcinoma. *J Gastrointestin Liver Dis* 2009;18:169-176.
48. Sparchez Z, Radu P, Anton O, Socaciu M, Badea R. Contrast enhanced ultrasound in assessing therapeutic response in ablative treatments of hepatocellular carcinoma. *J Gastrointestin Liver Dis* 2009;18:243-248.
49. Brace CL. Microwave ablation technology: what every user should know. *Curr Probl Diagn Radiol* 2009;38:61-67.
50. Bertram JM, Yang D, Converse MC, Webster JG, Mahvi DM. Antenna design for microwave hepatic ablation using an axisymmetric electromagnetic model. *Biomed Eng Online* 2006;5:15.
51. Wemyss-Holden SA, Dennison AR, Berry DP, Maddern GJ. Local ablation for unresectable liver tumors: is thermal best? *J Hepatobiliary Pancreat Surg* 2004;11:97-106.
52. Iannaccone R, Federle MP, Brancatelli G, Matsui O, Fishman EK, Narra VR, Grazioli L, et al. Peliosis hepatis: spectrum of imaging findings. *AJR Am J Roentgenol* 2006;187:W43-52.
53. Gannon CJ, Curley SA. The role of focal liver ablation in the treatment of unresectable primary and secondary malignant liver tumors. *Semin Radiat Oncol* 2005;15:265-272.
54. Dromain C, de Baere T, Elias D, Kuoch V, Ducreux M, Boige V, Petrow P, et al. Hepatic tumors treated with percutaneous radio-frequency ablation: CT and MR imaging follow-up. *Radiology* 2002;223:255-262.

55. Gravante G, Ong SL, Metcalfe MS, Strickland A, Dennison AR, Lloyd DM. Hepatic microwave ablation: a review of the histological changes following thermal damage. *Liver Int* 2008;28:911-921.
56. Dietrich CF. Characterisation of focal liver lesions with contrast enhanced ultrasonography. *Eur J Radiol* 2004;51 Suppl:S9-17.
57. Lam VW, Ng KK, Chok KS, Cheung TT, Yuen J, Tung H, Tso WK, et al. Risk factors and prognostic factors of local recurrence after radiofrequency ablation of hepatocellular carcinoma. *J Am Coll Surg* 2008;207:20-29.
58. Ng KK, Poon RT, Lo CM, Yuen J, Tso WK, Fan ST. Analysis of recurrence pattern and its influence on survival outcome after radiofrequency ablation of hepatocellular carcinoma. *J Gastrointest Surg* 2008;12:183-191.
59. Catalano O, Nunziata A, Lobianco R, Siani A. Real-time harmonic contrast material-specific US of focal liver lesions. *Radiographics* 2005;25:333-349.
60. Wagner JS, Adson MA, Van Heerden JA, Adson MH, Ilstrup DM. The natural history of hepatic metastases from colorectal cancer. A comparison with resective treatment. *Ann Surg* 1984;199:502-508.
61. Simmonds PC, Primrose JN, Colquitt JL, Garden OJ, Poston GJ, Rees M. Surgical resection of hepatic metastases from colorectal cancer: a systematic review of published studies. *Br J Cancer* 2006;94:982-999.
62. Scheele J, Stang R, Altendorf-Hofmann A, Paul M. Resection of colorectal liver metastases. *World J Surg* 1995;19:59-71.
63. Hohmann J, Albrecht T, Oldenburg A, Skrok J, Wolf KJ. Liver metastases in cancer: detection with contrast-enhanced ultrasonography. *Abdom Imaging* 2004;29:669-681.
64. Quaia E. Microbubble ultrasound contrast agents: an update. *Eur Radiol* 2007;17:1995-2008.
65. Morin SH, Lim AK, Cobbold JF, Taylor-Robinson SD. Use of second generation contrast-enhanced ultrasound in the assessment of focal liver lesions. *World J Gastroenterol* 2007;13:5963-5970.
66. Albrecht T, Blomley MJ, Burns PN, Wilson S, Harvey CJ, Leen E, Claudon M, et al. Improved detection of hepatic metastases with pulse-inversion US during the liver-specific phase of SHU 508A: multicenter study. *Radiology* 2003;227:361-370.
67. Yu JS, Rofsky NM. Hepatic metastases: perilesional enhancement on dynamic MRI. *AJR Am J Roentgenol* 2006;186:1051-1058.
68. Gravante G, Ong SL, Metcalfe MS, Bhardwaj N, Lloyd DM, Dennison AR. The effects of radiofrequency ablation on the hepatic parenchyma: histological bases for tumor recurrences. *Surg Oncol* 2011;20:237-245.
69. Wu H, Patel RB, Zheng Y, Solorio L, Krupka TM, Ziats NP, Haaga JR, et al. Differentiation of benign periablational enhancement from residual tumor following radiofrequency ablation using contrast-enhanced ultrasonography in a rat subcutaneous colon cancer model. *Ultrasound Med Biol* 2012;38:443-453.
70. Sandulescu L, Saftoiu A, Dumitrescu D, Ciurea T. The role of real-time contrast-enhanced and real-time virtual sonography in the assessment of malignant liver lesions. *J Gastrointest Liver Dis* 2009;18:103-108.
71. Strobel D, Krodel U, Martus P, Hahn EG, Becker D. Clinical evaluation of contrast-enhanced color Doppler sonography in the differential diagnosis of liver tumors. *J Clin Ultrasound* 2000;28:1-13.
72. Maruyama H, Takahashi M, Ishibashi H, Yoshikawa M, Yokosuka O. Contrast-enhanced ultrasound for characterisation of hepatic lesions appearing non-hypervascular on CT in chronic liver diseases. *Br J Radiol* 2012;85:351-357.

73. Nanashima A, Tobinaga S, Abo T, Kunizaki M, Takeshita H, Hidaka S, Taura N, et al. Usefulness of sonazoid-ultrasonography during hepatectomy in patients with liver tumors: A preliminary study. *J Surg Oncol* 2011;103:152-157.
74. Arita J, Hasegawa K, Takahashi M, Hata S, Shindoh J, Sugawara Y, Kokudo N. Correlation between contrast-enhanced intraoperative ultrasound using Sonazoid and histologic grade of resected hepatocellular carcinoma. *AJR Am J Roentgenol* 2011;196:1314-1321.
75. Dietrich CF, Schuessler G, Trojan J, Fellbaum C, Ignee A. Differentiation of focal nodular hyperplasia and hepatocellular adenoma by contrast-enhanced ultrasound. *Br J Radiol* 2005;78:704-707.
76. Gorur Y, Coibion C, Magotteaux P. [Contrast-enhanced ultrasound in hepatic focal nodular hyperplasia]. *Rev Med Liege* 2012;67:113-117.
77. Hatanaka K, Kudo M, Minami Y, Ueda T, Tatsumi C, Kitai S, Takahashi S, et al. Differential diagnosis of hepatic tumors: value of contrast-enhanced harmonic sonography using the newly developed contrast agent, Sonazoid. *Intervirol* 2008;51 Suppl 1:61-69.
78. Numata K, Isozaki T, Morimoto M, Sugimori K, Kunisaki R, Morizane T, Tanaka K. Prospective study of differential diagnosis of hepatic tumors by pattern-based classification of contrast-enhanced sonography. *World J Gastroenterol* 2006;12:6290-6298.
79. Bolondi L, Correas JM, Lencioni R, Weskott HP, Piscaglia F. New perspectives for the use of contrast-enhanced liver ultrasound in clinical practice. *Dig Liver Dis* 2007;39:187-195.
80. Cosgrove D, Blomley M. Liver tumors: evaluation with contrast-enhanced ultrasound. *Abdom Imaging* 2004;29:446-454.
81. Luo W, Numata K, Morimoto M, Kondo M, Takebayashi S, Okada M, Morita S, et al. Focal liver tumors: characterization with 3D perflubutane microbubble contrast agent-enhanced US versus 3D contrast-enhanced multidetector CT. *Radiology* 2009;251:287-295.
82. Chung YE, Kim MJ, Park YN, Choi JY, Pyo JY, Kim YC, Cho HJ, et al. Varying appearances of cholangiocarcinoma: radiologic-pathologic correlation. *Radiographics* 2009;29:683-700.
83. Elsayes KM, Menias CO, Willatt JM, Pandya A, Wiggins M, Platt J. Primary hepatic lymphoma: imaging findings. *J Med Imaging Radiat Oncol* 2009;53:373-379.
84. Hosten N, Puls R, Lemke AJ, Steger W, Zendel W, Zwicker C, Felix R. Contrast-enhanced power Doppler sonography: improved detection of characteristic flow patterns in focal liver lesions. *J Clin Ultrasound* 1999;27:107-115.
85. Kim EA, Yoon KH, Lee YH, Kim HW, Juhng SK, Won JJ. Focal hepatic lesions: contrast-enhancement patterns at pulse-inversion harmonic US using a microbubble contrast agent. *Korean J Radiol* 2003;4:224-233.
86. Quaia E, Bartolotta TV, Midiri M, Cernic S, Belgrano M, Cova M. Analysis of different contrast enhancement patterns after microbubble-based contrast agent injection in liver hemangiomas with atypical appearance on baseline scan. *Abdom Imaging* 2006;31:59-64.
87. Bleuzen A, Huang C, Olar M, Tchienbou J, Tranquart F. Diagnostic accuracy of contrast-enhanced ultrasound in focal lesions of the liver using cadence contrast pulse sequencing. *Ultraschall Med* 2006;27:40-48.
88. Quaia E, D'Onofrio M, Palumbo A, Rossi S, Bruni S, Cova M. Comparison of contrast-enhanced ultrasonography versus baseline ultrasound and contrast-enhanced computed tomography in metastatic disease of the liver: diagnostic performance and confidence. *Eur Radiol* 2006;16:1599-1609.

89. Vilana R, Bianchi L, Varela M, Nicolau C, Sanchez M, Ayuso C, Garcia M, et al. Is microbubble-enhanced ultrasonography sufficient for assessment of response to percutaneous treatment in patients with early hepatocellular carcinoma? *Eur Radiol* 2006;16:2454-2462.
90. Celli N, Gaiani S, Piscaglia F, Zironi G, Camaggi V, Leoni S, Righini R, et al. Characterization of liver lesions by real-time contrast-enhanced ultrasonography. *Eur J Gastroenterol Hepatol* 2007;19:3-14.
91. Soye JA, Mullan CP, Porter S, Beattie H, Barltrop AH, Nelson WM. The use of contrast-enhanced ultrasound in the characterisation of focal liver lesions. *Ulster Med J* 2007;76:22-25.
92. Dai Y, Chen MH, Yin SS, Yan K, Fan ZH, Wu W, Wang YB, et al. Focal liver lesions: can SonoVue-enhanced ultrasound be used to differentiate malignant from benign lesions? *Invest Radiol* 2007;42:596-603.
93. Wang Y, Yu X, Tang J, Li H, Liu L, Gao Y. Solitary necrotic nodule of the liver: contrast-enhanced sonography. *J Clin Ultrasound* 2007;35:177-181.
94. Wang ZL, Tang J, Weskott HP, Li JL, Wang W, Luo YK, An LC, et al. Undetermined focal liver lesions on gray-scale ultrasound in patients with fatty liver: characterization with contrast-enhanced ultrasound. *J Gastroenterol Hepatol* 2008;23:1511-1519.
95. D'Onofrio M, Faccioli N, Zamboni G, Malago R, Caffarri S, Fattovich G, Mucelli RP. Focal liver lesions in cirrhosis: value of contrast-enhanced ultrasonography compared with Doppler ultrasound and alpha-fetoprotein levels. *Radiol Med* 2008;113:978-991.
96. Xu HX, Xie XY, Lu MD, Liu GJ, Xu ZF, Zheng YL, Liang JY, et al. Contrast-enhanced sonography in the diagnosis of small hepatocellular carcinoma ≤ 2 cm. *J Clin Ultrasound* 2008;36:257-266.
97. Xia Y, Kudo M, Minami Y, Hatanaka K, Ueshima K, Chung H, Hagiwara S, et al. Response evaluation of transcatheter arterial chemoembolization in hepatocellular carcinomas: the usefulness of sonazoid-enhanced harmonic sonography. *Oncology* 2008;75 Suppl 1:99-105.
98. Lu Q, Luo Y, Yuan CX, Zeng Y, Wu H, Lei Z, Zhong Y, et al. Value of contrast-enhanced intraoperative ultrasound for cirrhotic patients with hepatocellular carcinoma: a report of 20 cases. *World J Gastroenterol* 2008;14:4005-4010.
99. Moriyasu F, Itoh K. Efficacy of perflubutane microbubble-enhanced ultrasound in the characterization and detection of focal liver lesions: phase 3 multicenter clinical trial. *AJR Am J Roentgenol* 2009;193:86-95.
100. Korenaga K, Korenaga M, Furukawa M, Yamasaki T, Sakaida I. Usefulness of Sonazoid contrast-enhanced ultrasonography for hepatocellular carcinoma: comparison with pathological diagnosis and superparamagnetic iron oxide magnetic resonance images. *J Gastroenterol* 2009;44:733-741.
101. Bartolotta TV, Sandonato L, Taibbi A, Latteri S, Soresi M, Lombardo G, Genova C, et al. [Focal liver lesions: clinical usefulness of contrast-enhanced ultrasound in the selection of surgical patients]. *Chir Ital* 2009;61:295-307.
102. Hatanaka K, Chung H, Kudo M, Haji S, Minami Y, Maekawa K, Hayaishi S, et al. Usefulness of the post-vascular phase of contrast-enhanced ultrasonography with sonazoid in the evaluation of gross types of hepatocellular carcinoma. *Oncology* 2010;78 Suppl 1:53-59.
103. Beaton C, Cochlin D, Kumar N. Contrast enhanced ultrasound should be the initial radiological investigation to characterise focal liver lesions. *Eur J Surg Oncol* 2010;36:43-46.
104. Bartolotta TV, Taibbi A, Midiri M, La Grutta L, De Maria M, Lagalla R. Characterisation of focal liver lesions undetermined at grey-scale US: contrast-enhanced US versus 64-row MDCT and MRI with liver-specific contrast agent. *Radiol Med* 2010;115:714-731.

105. Ooi CC, Low SC, Schneider-Kolsky M, Lombardo P, Lim SY, Abu Bakar R, Lo RH. Diagnostic accuracy of contrast-enhanced ultrasound in differentiating benign and malignant focal liver lesions: a retrospective study. *J Med Imaging Radiat Oncol* 2010;54:421-430.
106. Laghi F, Catalano O, Maresca M, Sandomenico F, Siani A. Indeterminate, subcentimetric focal liver lesions in cancer patients: additional role of contrast-enhanced ultrasound. *Ultraschall Med* 2010;31:283-288.
107. Morana G, Cugini C, Mucelli RP. Small liver lesions in oncologic patients: characterization with CT, MRI and contrast-enhanced US. *Cancer Imaging* 2008;8 Spec No A:S132-135.
108. Numata K, Luo W, Morimoto M, Kondo M, Kunishi Y, Sasaki T, Nozaki A, et al. Contrast enhanced ultrasound of hepatocellular carcinoma. *World J Radiol* 2010;2:68-82.
109. Takahashi M, Maruyama H, Ishibashi H, Yoshikawa M, Yokosuka O. Contrast-enhanced ultrasound with perflubutane microbubble agent: evaluation of differentiation of hepatocellular carcinoma. *AJR Am J Roentgenol* 2011;196:W123-131.
110. Li C, Wang W, Ding H, Huang B, Cao J, Mao F, Ji Z. Value of contrast-enhanced sonography in the diagnosis of peripheral intrahepatic cholangiocarcinoma. *J Clin Ultrasound* 2011;39:447-453.
111. Konopke R, Bunk A, Kersting S. The role of contrast-enhanced ultrasound for focal liver lesion detection: an overview. *Ultrasound Med Biol* 2007;33:1515-1526.
112. Jung EM, Ross CJ, Rennert J, Scherer MN, Farkas S, von Breitenbuch P, Schnitzbauer AA, et al. Characterization of microvascularization of liver tumor lesions with high resolution linear ultrasound and contrast enhanced ultrasound (CEUS) during surgery: First results. *Clin Hemorheol Microcirc* 2010;46:89-99.
113. Rutherford AE, Hynan LS, Borges CB, Forcione DG, Blackard JT, Lin W, Gorman AR, et al. Serum apoptosis markers in acute liver failure: a pilot study. *Clin Gastroenterol Hepatol* 2007;5:1477-1483.
114. Alaboudy A, Inoue T, Hatanaka K, Chung H, Hyodo T, Kumano S, Murakami T, et al. Usefulness of combination of imaging modalities in the diagnosis of hepatocellular carcinoma using Sonazoid(R)-enhanced ultrasound, gadolinium diethylene-triamine-pentaacetic acid-enhanced magnetic resonance imaging, and contrast-enhanced computed tomography. *Oncology* 2011;81 Suppl 1:66-72.
115. Delorme S, Krix M. Contrast-enhanced ultrasound for examining tumor biology. *Cancer Imaging* 2006;6:148-152.
116. Yanagisawa K, Moriyasu F, Miyahara T, Yuki M, Iijima H. Phagocytosis of ultrasound contrast agent microbubbles by Kupffer cells. *Ultrasound Med Biol* 2007;33:318-325.
117. Schneider M. Characteristics of SonoVue trade mark. *Echocardiography* 1999;16:743-746.
118. Numata K, Morimoto M, Ogura T, Sugimori K, Takebayashi S, Okada M, Tanaka K. Ablation therapy guided by contrast-enhanced sonography with Sonazoid for hepatocellular carcinoma lesions not detected by conventional sonography. *J Ultrasound Med* 2008;27:395-406.
119. Monaghan MJ. Echo contrast enhancement of the left ventricle--imaging technology and micro-spheres, is the marriage critical? *Eur J Echocardiogr* 2001;2:143-144.
120. Du WH, Yang WX, Wang X, Xiong XQ, Zhou Y, Li T. Assessment of hepatic VX2 tumors of rabbits with second harmonic imaging under high and low acoustic pressures. *World J Gastroenterol* 2003;9:1679-1682.
121. Bartolozzi C, Lencioni R. Contrast-specific ultrasound imaging of focal liver lesions. Prologue to a promising future. *Eur Radiol* 2001;11 Suppl 3:E13-14.

122. Lencioni R, Cioni D, Bartolozzi C. Tissue harmonic and contrast-specific imaging: back to gray scale in ultrasound. *Eur Radiol* 2002;12:151-165.
123. Yamamoto K, Shiraki K, Nakanishi S, Fuke H, Nakano T, Hashimoto A, Shimizu A, et al. 1.5 Harmonic Imaging Sonography with microbubble contrast agent improves characterization of hepatocellular carcinoma. *World J Gastroenterol* 2005;11:5607-5613.
124. Arita J, Takahashi M, Hata S, Shindoh J, Beck Y, Sugawara Y, Hasegawa K, et al. Usefulness of contrast-enhanced intraoperative ultrasound using Sonazoid in patients with hepatocellular carcinoma. *Ann Surg* 2011;254:992-999.
125. Torzilli G, Palmisano A, Del Fabbro D, Marconi M, Donadon M, Spinelli A, Bianchi PP, et al. Contrast-enhanced intraoperative ultrasonography during surgery for hepatocellular carcinoma in liver cirrhosis: is it useful or useless? A prospective cohort study of our experience. *Ann Surg Oncol* 2007;14:1347-1355.
126. Minami Y, Kudo M. Review of dynamic contrast-enhanced ultrasound guidance in ablation therapy for hepatocellular carcinoma. *World J Gastroenterol* 2011;17:4952-4959.
127. Solbiati L, Ierace T, Tonolini M, Cova L. Guidance and monitoring of radiofrequency liver tumor ablation with contrast-enhanced ultrasound. *Eur J Radiol* 2004;51 Suppl:S19-23.
128. Nouse K, Shiraga K, Uematsu S, Okamoto R, Harada R, Takayama S, Kawai W, et al. Prediction of the ablated area by the spread of microbubbles during radiofrequency ablation of hepatocellular carcinoma. *Liver Int* 2005;25:967-972.
129. Schumann PA, Christiansen JP, Quigley RM, McCreery TP, Sweitzer RH, Unger EC, Lindner JR, et al. Targeted-microbubble binding selectively to GPIIb IIIa receptors of platelet thrombi. *Invest Radiol* 2002;37:587-593.
130. Dayton PA, Pearson D, Clark J, Simon S, Schumann PA, Zutshi R, Matsunaga TO, et al. Ultrasonic analysis of peptide- and antibody-targeted microbubble contrast agents for molecular imaging of alphavbeta3-expressing cells. *Mol Imaging* 2004;3:125-134.
131. Schneider M. Molecular imaging and ultrasound-assisted drug delivery. *J Endourol* 2008;22:795-802.
132. Lindner JR. Microbubbles in medical imaging: current applications and future directions. *Nat Rev Drug Discov* 2004;3:527-532.
133. Postema M, Schmitz G. Bubble dynamics involved in ultrasonic imaging. *Expert Rev Mol Diagn* 2006;6:493-502.
134. Feinstein SB. The powerful microbubble: from bench to bedside, from intravascular indicator to therapeutic delivery system, and beyond. *Am J Physiol Heart Circ Physiol* 2004;287:H450-457.
135. Farook U, Stride E, Edirisinghe MJ. Preparation of suspensions of phospholipid-coated microbubbles by coaxial electrohydrodynamic atomization. *J R Soc Interface* 2009;6:271-277.
136. Sirsi S, Feshitan J, Kwan J, Homma S, Borden M. Effect of microbubble size on fundamental mode high frequency ultrasound imaging in mice. *Ultrasound Med Biol* 2010;36:935-948.
137. Kheir JN, Scharp LA, Borden MA, Swanson EJ, Loxley A, Reese JH, Black KJ, et al. Oxygen gas-filled microparticles provide intravenous oxygen delivery. *Sci Transl Med* 2012;4:140ra188.
138. Kim TK, Jang HJ, Wilson SR. Benign liver masses: imaging with microbubble contrast agents. *Ultrasound Q* 2006;22:31-39.
139. Burns PN, Wilson SR. Microbubble contrast for radiological imaging: 1. Principles. *Ultrasound Q* 2006;22:5-13.
140. Cosgrove D, Harvey C. Clinical uses of microbubbles in diagnosis and treatment. *Med Biol Eng Comput* 2009;47:813-826.

141. Stride E, Saffari N. Microbubble ultrasound contrast agents: a review. *Proc Inst Mech Eng H* 2003;217:429-447.
142. Sirsi S, Borden M. Microbubble Compositions, Properties and Biomedical Applications. *Bubble Sci Eng Technol* 2009;1:3-17.
143. Sirsi SR, Borden MA. Advances in ultrasound mediated gene therapy using microbubble contrast agents. *Theranostics* 2012;2:1208-1222.
144. Cakmakci H, Gulcu A, Zenger MN. Mirror-image artifact mimicking epidural hematoma: usefulness of power Doppler sonography. *J Clin Ultrasound* 2003;31:437-439.
145. Klivanov AL. Microbubble contrast agents: targeted ultrasound imaging and ultrasound-assisted drug-delivery applications. *Invest Radiol* 2006;41:354-362.
146. O'Brien WD, Jr. Ultrasound-biophysics mechanisms. *Prog Biophys Mol Biol* 2007;93:212-255.
147. Senior R, Kaul S, Soman P, Lahiri A. Power doppler harmonic imaging: a feasibility study of a new technique for the assessment of myocardial perfusion. *Am Heart J* 2000;139:245-251.
148. Metoki R, Moriyasu F, Kamiyama N, Sugimoto K, Iijima H, Xu HX, Aoki T, et al. Quantification of hepatic parenchymal blood flow by contrast ultrasonography with flash-replenishment imaging. *Ultrasound Med Biol* 2006;32:1459-1466.
149. Stride E, Porter C, Prieto AG, Pankhurst Q. Enhancement of microbubble mediated gene delivery by simultaneous exposure to ultrasonic and magnetic fields. *Ultrasound Med Biol* 2009;35:861-868.
150. Leong-Poi H, Christiansen J, Klivanov AL, Kaul S, Lindner JR. Noninvasive assessment of angiogenesis by ultrasound and microbubbles targeted to alpha(v)-integrins. *Circulation* 2003;107:455-460.
151. Wilson SR, Kim TK, Jang HJ, Burns PN. Enhancement patterns of focal liver masses: discordance between contrast-enhanced sonography and contrast-enhanced CT and MRI. *AJR Am J Roentgenol* 2007;189:W7-W12.
152. T K. Microbubble contrast agents for ultrasound imaging-Safety and Efficacy in Abdominal and Vascular Imaging. *Liver imaging* 2008:54-57.
153. Nicolaj Grønæk Laugesen¹ CPN, Jacob Rosenberg³. Clinical Applications of Contrast-Enhanced Ultrasound in the Pediatric Work-Up of Focal Liver Lesions and Blunt Abdominal Trauma: A Systematic Review. *Ultrasound Int Open* 2017;3:E2-E7.
154. Piscaglia F, Nolsoe C, Dietrich CF, Cosgrove DO, Gilja OH, Bachmann Nielsen M, Albrecht T, et al. The EFSUMB Guidelines and Recommendations on the Clinical Practice of Contrast Enhanced Ultrasound (CEUS): update 2011 on non-hepatic applications. *Ultraschall Med* 2012;33:33-59.
155. C C. Transcutaneous contrast-enhanced sonography of pleuralbased pulmonary lesions. . *Eur J Radiol* 2007;64:213–221.
156. Cantisani V, Grazhdani H, Fioravanti C, Rosignuolo M, Calliada F, Messineo D, Bernieri MG, et al. Liver metastases: Contrast-enhanced ultrasound compared with computed tomography and magnetic resonance. *World J Gastroenterol* 2014;20:9998-10007.
157. Seitz K, Strobel D, Bernatik T, Blank W, Friedrich-Rust M, Herbay A, Dietrich CF, et al. Contrast-Enhanced Ultrasound (CEUS) for the characterization of focal liver lesions - prospective comparison in clinical practice: CEUS vs. CT (DEGUM multicenter trial). Parts of this manuscript were presented at the Ultrasound Dreiländertreffen 2008, Davos. *Ultraschall Med* 2009;30:383-389.
158. Mulvagh SL, Rakowski H, Vannan MA, Abdelmoneim SS, Becher H, Bierig SM, Burns PN, et al. American Society of Echocardiography Consensus Statement on the Clinical Applications of Ultrasonic Contrast Agents in Echocardiography. *J Am Soc Echocardiogr* 2008;21:1179-1201; quiz 1281.

159. Arend F, L. Schinkel MK, Daniel Staub. Contrast-enhanced ultrasound: clinical applications in patients with atherosclerosis. *Int J Cardiovasc Imaging* 2016;32:35–48.
160. Thanigaraj S, SK, Perez JE Improved echocardiographic delineation of left ventricular thrombus with the use of intravenous second-generation contrast image enhancement. *J Am Soc Echocardiogr* 1999;12:1022–1026.
161. Rafailidis V, Partovi S, Dikkes A, Nakamoto DA, Azar N, Staub D. Evolving clinical applications of contrast-enhanced ultrasound (CEUS) in the abdominal aorta. *Cardiovasc Diagn Ther* 2018;8:S118-S130.
162. Partovi S, LM, Aschwanden M, Baldi T, Jaeger KA, Feinstein SB, Staub D Contrast-enhanced ultrasound for assessing carotid atherosclerotic plaque lesions. *AJR Am J Roentgenol* 2012;198:W13–W19.
163. van den Oord SC, tKG, Sijbrands EJ, van der Steen AF, Schinkel AF Effect of carotid plaque screening using contrast-enhanced ultrasound on cardiovascular risk stratification. *Am J Cardiol* 2013;111:754–775.
164. Clevert DA, SW, Helck A, Reiser M. Duplex and contrast enhanced ultrasound (CEUS) in evaluation of in-stent restenosis after carotid stenting. *Clin Hemorheol Microcirc* 2011;48:199–208.
165. Clevert DA, SM, Flach P, et al. Contrast-enhanced ultrasound in detection and follow-up of an infrarenal abdominal aortic aneurysm with aorto-caval fistula and endovascular treatment. *Cardiovasc Intervent Radiol* 2007;30:480-484.
166. Shah A, SS. Imaging Surveillance following Endovascular Aneurysm Repair. *Semin Intervent Radiol* 26:10-16.
167. Dill-Macky MJ, WS, Sternbach Y, et al. Detecting Endoleaks in Aortic Endografts Using Contrast-Enhanced Sonography. *Am J Roentgenol* 2007;188:W262-268.
168. Yang X, CY, Zhang B, et al. Contrast-enhanced Ultrasound in Detecting Endoleaks with Failed Computed Tomography Angiography Diagnosis after Endovascular Abdominal Aortic Aneurysm Repair. *Chin Med J (Engl)* 2015;128:2491-2497.
169. Clevert DA, MN, Weckbach S, et al. Color duplex ultrasound and contrast-enhanced ultrasound in comparison to MS-CT in the detection of endoleak following endovascular aneurysm repair. *Clin Hemorheol Microcirc* 2008;39:121-132.
170. Clevert DA, HA, Kopp R, et al. Imaging of endoleaks after endovascular aneurysm repair (EVAR) with contrast-enhanced ultrasound (CEUS). *Radiologe* 2009;49:1033-1039.
171. Clevert DA, WS, Kopp R, et al. Imaging of aortic lesions with color coded duplex sonography and contrast-enhanced ultrasound versus multislice computed tomography (MS-CT) angiography. *Clin Hemorheol Microcirc* 2008;40:267-279.
172. Clevert DA, SM, Johnson T, et al. Imaging of aortic abnormalities with contrast-enhanced ultrasound. A pictorial comparison with CT. *Eur Radiol* 2007;17:2991-3000.
173. Magnoni M, DL, Coli S, et al. Assessment of Takayasu arteritis activity by carotid contrast-enhanced ultrasound. *Circ Cardiovasc Imaging* 2011;4:1-1.
174. Tafuto S, CO, Barba G et al. Real-time contrast-enhanced specific ultrasound in staging and follow-up of splenic lymphomas. *Front Biosci* 2006;11:2224–2229.
175. Caruso G, SG, Campisi A et al. Bladder tumor staging: comparison of contrast-enhanced and gray-scale ultrasound. *Am J Roentgenol* 2010;194:151–156.
176. Moschouris H, SK, Lampropoulou E et al. Imaging of the acute scrotum: is there a place for contrast-enhanced ultrasonography? *Int Braz J Uro* 2009;35:692–702.
177. Miller DL, Dou C. Induction of apoptosis in sonoporation and ultrasonic gene transfer. *Ultrasound Med Biol* 2009;35:144-154.

178. Kooiman K, Foppen-Harteveld M, de Jong N. Ultrasound-mediated targeted microbubble sonoporation of endothelial cells. *J Control Release* 2010;148:e62-63.
179. Ando H, Feril LB, Jr., Kondo T, Tabuchi Y, Ogawa R, Zhao QL, Cui ZG, et al. An echo-contrast agent, Levovist, lowers the ultrasound intensity required to induce apoptosis of human leukemia cells. *Cancer Lett* 2006;242:37-45.
180. ter Haar GR. Ultrasonic contrast agents: safety considerations reviewed. *Eur J Radiol* 2002;41:217-221.
181. Stride EP, Coussios CC. Cavitation and contrast: the use of bubbles in ultrasound imaging and therapy. *Proc Inst Mech Eng H* 2010;224:171-191.
182. Collis J, Manasseh R, Liovic P, Tho P, Ooi A, Petkovic-Duran K, Zhu Y. Cavitation microstreaming and stress fields created by microbubbles. *Ultrasonics* 2010;50:273-279.
183. Suslick KS. Sonochemistry. *Science* 1990;247:1439-1445.
184. Saraste A, Nekolla SG, Schwaiger M. Cardiovascular molecular imaging: an overview. *Cardiovasc Res* 2009;83:643-652.
185. Riess JG, Cornelus C, Follana R, Krafft MP, Mahe AM, Postel M, Zarif L. Novel fluorocarbon-based injectable oxygen-carrying formulations with long-term room-temperature storage stability. *Adv Exp Med Biol* 1994;345:227-234.
186. Takalkar AM, Klibanov AL, Rychak JJ, Lindner JR, Ley K. Binding and detachment dynamics of microbubbles targeted to P-selectin under controlled shear flow. *J Control Release* 2004;96:473-482.
187. Dittmar KM, Xie J, Hunter F, Trimble C, Bur M, Frenkel V, Li KC. Pulsed high-intensity focused ultrasound enhances systemic administration of naked DNA in squamous cell carcinoma model: initial experience. *Radiology* 2005;235:541-546.
188. Lum AF, Borden MA, Dayton PA, Kruse DE, Simon SI, Ferrara KW. Ultrasound radiation force enables targeted deposition of model drug carriers loaded on microbubbles. *J Control Release* 2006;111:128-134.
189. Klibanov AL, Rychak JJ, Yang WC, Alikhani S, Li B, Acton S, Lindner JR, et al. Targeted ultrasound contrast agent for molecular imaging of inflammation in high-shear flow. *Contrast Media Mol Imaging* 2006;1:259-266.
190. Yasu T, Greener Y, Jablonski E, Killam AL, Fukuda S, Suematsu M, Tojo SJ, et al. Activated leukocytes and endothelial cells enhance retention of ultrasound contrast microspheres containing perfluoropropane in inflamed venules. *Int J Cardiol* 2005;98:245-252.
191. Lindner JR, Song J, Christiansen J, Klibanov AL, Xu F, Ley K. Ultrasound assessment of inflammation and renal tissue injury with microbubbles targeted to P-selectin. *Circulation* 2001;104:2107-2112.
192. Yang J, Galipeau J, Kozak CA, Furie BC, Furie B. Mouse P-selectin glycoprotein ligand-1: molecular cloning, chromosomal localization, and expression of a functional P-selectin receptor. *Blood* 1996;87:4176-4186.
193. Rychak JJ, Klibanov AL, Ley KF, Hossack JA. Enhanced targeting of ultrasound contrast agents using acoustic radiation force. *Ultrasound Med Biol* 2007;33:1132-1139.
194. Ellegala DB, Leong-Poi H, Carpenter JE, Klibanov AL, Kaul S, Shaffrey ME, Sklenar J, et al. Imaging tumor angiogenesis with contrast ultrasound and microbubbles targeted to alpha(v)beta3. *Circulation* 2003;108:336-341.
195. Korpanty G, Carbon JG, Grayburn PA, Fleming JB, Brekken RA. Monitoring response to anticancer therapy by targeting microbubbles to tumor vasculature. *Clin Cancer Res* 2007;13:323-330.
196. Willmann JK, Lutz AM, Paulmurugan R, Patel MR, Chu P, Rosenberg J, Gambhir SS. Dual-targeted contrast agent for US assessment of tumor angiogenesis in vivo. *Radiology* 2008;248:936-944.

197. Culp WC, Porter TR, Lowery J, Xie F, Roberson PK, Marky L. Intracranial clot lysis with intravenous microbubbles and transcranial ultrasound in swine. *Stroke* 2004;35:2407-2411.
198. Alonso A, Dempfle CE, Della Martina A, Stroick M, Fatar M, Zohsel K, Allemann E, et al. In vivo clot lysis of human thrombus with intravenous abciximab immunobubbles and ultrasound. *Thromb Res* 2009;124:70-74.
199. Martin MJ, Chung EM, Goodall AH, Della Martina A, Ramnarine KV, Fan L, Hainsworth SV, et al. Enhanced detection of thromboemboli with the use of targeted microbubbles. *Stroke* 2007;38:2726-2732.
200. Xie F, Lof J, Matsunaga T, Zutshi R, Porter TR. Diagnostic ultrasound combined with glycoprotein IIb/IIIa-targeted microbubbles improves microvascular recovery after acute coronary thrombotic occlusions. *Circulation* 2009;119:1378-1385.
201. Birnbaum Y, Luo H, Nagai T, Fishbein MC, Peterson TM, Li S, Kricsfeld D, et al. Noninvasive in vivo clot dissolution without a thrombolytic drug: recanalization of thrombosed iliofemoral arteries by transcutaneous ultrasound combined with intravenous infusion of microbubbles. *Circulation* 1998;97:130-134.
202. Tachibana K, Tachibana S. Albumin microbubble echo-contrast material as an enhancer for ultrasound accelerated thrombolysis. *Circulation* 1995;92:1148-1150.
203. Shohet RV, Chen S, Zhou YT, Wang Z, Meidell RS, Unger RH, Grayburn PA. Echocardiographic destruction of albumin microbubbles directs gene delivery to the myocardium. *Circulation* 2000;101:2554-2556.
204. Ogawa R, Kondo T, Honda H, Zhao QL, Fukuda S, Riesz P. Effects of dissolved gases and an echo contrast agent on ultrasound mediated in vitro gene transfection. *Ultrason Sonochem* 2002;9:197-203.
205. Wang X, Liang HD, Dong B, Lu QL, Blomley MJ. Gene transfer with microbubble ultrasound and plasmid DNA into skeletal muscle of mice: comparison between commercially available microbubble contrast agents. *Radiology* 2005;237:224-229.
206. Manome Y, Nakayama N, Nakayama K, Furuhashi H. Insonation facilitates plasmid DNA transfection into the central nervous system and microbubbles enhance the effect. *Ultrasound Med Biol* 2005;31:693-702.
207. Tsunoda S, Mazda O, Oda Y, Iida Y, Akabame S, Kishida T, Shin-Ya M, et al. Sonoporation using microbubble BR14 promotes pDNA/siRNA transduction to murine heart. *Biochem Biophys Res Commun* 2005;336:118-127.
208. Kodama T, Tomita Y, Koshiyama K, Blomley MJ. Transfection effect of microbubbles on cells in superposed ultrasound waves and behavior of cavitation bubble. *Ultrasound Med Biol* 2006;32:905-914.
209. Yamashita T, Sonoda S, Suzuki R, Arimura N, Tachibana K, Maruyama K, Sakamoto T. A novel bubble liposome and ultrasound-mediated gene transfer to ocular surface: RC-1 cells in vitro and conjunctiva in vivo. *Exp Eye Res* 2007;85:741-748.
210. Wang JF, Wang JB, Chen H, Zhang CM, Liu L, Pan SH, Wu CJ. Ultrasound-mediated microbubble destruction enhances gene transfection in pancreatic cancer cells. *Adv Ther* 2008;25:412-421.
211. Christiansen JP, French BA, Klivanov AL, Kaul S, Lindner JR. Targeted tissue transfection with ultrasound destruction of plasmid-bearing cationic microbubbles. *Ultrasound Med Biol* 2003;29:1759-1767.
212. Bekeredjian R, Kroll RD, Fein E, Tinkov S, Coester C, Winter G, Katus HA, et al. Ultrasound targeted microbubble destruction increases capillary permeability in hepatomas. *Ultrasound Med Biol* 2007;33:1592-1598.

213. Watanabe A, Otake R, Nozaki T, Morii A, Ogawa R, Fujimoto S, Nakamura S, et al. Effects of microbubbles on ultrasound-mediated gene transfer in human prostate cancer PC3 cells: comparison among Levovist, YM454, and MRX-815H. *Cancer Lett* 2008;265:107-112.
214. Iwanaga K, Tominaga K, Yamamoto K, Habu M, Maeda H, Akifusa S, Tsujisawa T, et al. Local delivery system of cytotoxic agents to tumors by focused sonoporation. *Cancer Gene Ther* 2007;14:354-363.
215. Chapuis JC, Schmaltz RM, Tsosie KS, Belohlavek M, Hecht SM. Carbohydrate dependent targeting of cancer cells by bleomycin-microbubble conjugates. *J Am Chem Soc* 2009;131:2438-2439.
216. Maeda H, Tominaga K, Iwanaga K, Nagao F, Habu M, Tsujisawa T, Seta Y, et al. Targeted drug delivery system for oral cancer therapy using sonoporation. *J Oral Pathol Med* 2009;38:572-579.
217. Xing W, Gang WZ, Yong Z, Yi ZY, Shan XC, Tao RH. Treatment of xenografted ovarian carcinoma using paclitaxel-loaded ultrasound microbubbles. *Acad Radiol* 2008;15:1574-1579.
218. Liu GJ, Moriyasu F, Hirokawa T, Rexiati M, Yamada M, Imai Y. Expression of heat shock protein 70 in rabbit liver after contrast-enhanced ultrasound and radiofrequency ablation. *Ultrasound Med Biol* 2010;36:78-85.
219. Sato Y. Update on endogenous inhibitors of angiogenesis. *Endothelium* 2006;13:147-155.
220. Soldi R, Mitola S, Strasly M, Defilippi P, Tarone G, Bussolino F. Role of alphavbeta3 integrin in the activation of vascular endothelial growth factor receptor-2. *EMBO J* 1999;18:882-892.
221. Santulli G, Basilicata MF, De Simone M, Del Giudice C, Anastasio A, Sorriento D, Saviano M, et al. Evaluation of the anti-angiogenic properties of the new selective alphaVbeta3 integrin antagonist RGDechiHCit. *J Transl Med* 2011;9:7.
222. Alonso A, Della Martina A, Stroick M, Fatar M, Griebel M, Pochon S, Schneider M, et al. Molecular imaging of human thrombus with novel abciximab immunobubbles and ultrasound. *Stroke* 2007;38:1508-1514.
223. Ueland T, Aukrust P, Omdal TR, Damas JK, Endresen K, Ren F, Hysing J. Effect of eptifibatid on platelet-mediated inflammation in acute coronary syndromes. *Int J Cardiol* 2011;151:385-387.
224. Lin CR, Chen KH, Yang CH, Cheng JT, Sheen-Chen SM, Wu CH, Sy WD, et al. Sonoporation-mediated gene transfer into adult rat dorsal root ganglion cells. *J Biomed Sci* 2010;17:44.
225. Hernot S, Klibanov AL. Microbubbles in ultrasound-triggered drug and gene delivery. *Adv Drug Deliv Rev* 2008;60:1153-1166.
226. Hallow DM, Mahajan AD, Prausnitz MR. Ultrasonically targeted delivery into endothelial and smooth muscle cells in ex vivo arteries. *J Control Release* 2007;118:285-293.
227. Unger EC, Porter T, Culp W, Labell R, Matsunaga T, Zutshi R. Therapeutic applications of lipid-coated microbubbles. *Adv Drug Deliv Rev* 2004;56:1291-1314.
228. Ferrara KW, Borden MA, Zhang H. Lipid-shelled vehicles: engineering for ultrasound molecular imaging and drug delivery. *Acc Chem Res* 2009;42:881-892.
229. Qin S, Caskey CF, Ferrara KW. Ultrasound contrast microbubbles in imaging and therapy: physical principles and engineering. *Phys Med Biol* 2009;54:R27-57.
230. Lindner JR. Evolving applications for contrast ultrasound. *Am J Cardiol* 2002;90:72J-80J.
231. Waldmann TA. Immunotherapy: past, present and future. *Nat Med* 2003;9:269-277.

232. Rai R, Richardson C, Flecknell P, Robertson H, Burt A, Manas DM. Study of apoptosis and heat shock protein (HSP) expression in hepatocytes following radiofrequency ablation (RFA). *J Surg Res* 2005;129:147-151.
233. Nikfarjam M, Muralidharan V, Su K, Malcontenti-Wilson C, Christophi C. Patterns of heat shock protein (HSP70) expression and Kupffer cell activity following thermal ablation of liver and colorectal liver metastases. *Int J Hyperthermia* 2005;21:319-332.
234. Wang HH, Mao CY, Teng LS, Cao J. Recent advances in heat shock protein-based cancer vaccines. *Hepatobiliary Pancreat Dis Int* 2006;5:22-27.
235. Feril LB, Jr., Kondo T. Biological effects of low intensity ultrasound: the mechanism involved, and its implications on therapy and on biosafety of ultrasound. *J Radiat Res* 2004;45:479-489.
236. Sasaki H, Matsuno T, Tanaka N, Orita K. Activation of apoptosis during the reperfusion phase after rat liver ischemia. *Transplant Proc* 1996;28:1908-1909.
237. Yang M, Antoine DJ, Weemhoff JL, Jenkins RE, Farhood A, Park BK, Jaeschke H. Biomarkers distinguish apoptotic and necrotic cell death during hepatic ischemia/reperfusion injury in mice. *Liver Transpl* 2014;20:1372-1382.
238. Zapletal C, Jahnke C, Mehrabi A, Hess T, Mihm D, Angelescu M, Stegen P, et al. Quantification of liver perfusion by dynamic magnetic resonance imaging: experimental evaluation and clinical pilot study. *Liver Transpl* 2009;15:693-700.
239. Schroeder T, Malago M, Debatin JF, Goyen M, Nadalin S, Ruehm SG. "All-in-one" imaging protocols for the evaluation of potential living liver donors: comparison of magnetic resonance imaging and multidetector computed tomography. *Liver Transpl* 2005;11:776-787.
240. Tian JL, Zhang JS. Hepatic perfusion disorders: etiopathogenesis and related diseases. *World J Gastroenterol* 2006;12:3265-3270.
241. Pandharipande PV, Krinsky GA, Rusinek H, Lee VS. Perfusion imaging of the liver: current challenges and future goals. *Radiology* 2005;234:661-673.
242. Susa M, Iyer AK, Ryu K, Hornicek FJ, Mankin H, Amiji MM, Duan Z. Doxorubicin loaded Polymeric Nanoparticulate Delivery System to overcome drug resistance in osteosarcoma. *BMC Cancer* 2009;9:399.
243. Wang B, Zang WJ, Wang M, Ai H, Wang YW, Li YP, He GS, et al. Prolonging the ultrasound signal enhancement from thrombi using targeted microbubbles based on sulfur-hexafluoride-filled gas. *Acad Radiol* 2006;13:428-433.
244. Ong SL, Gravante G, Metcalfe MS, Dennison AR. History, ethics, advantages and limitations of experimental models for hepatic ablation. *World J Gastroenterol* 2013;19:147-154.
245. Aggarwal S, Obrist W, Yonas H, Kramer D, Kang Y, Scott V, Planinsic R. Cerebral hemodynamic and metabolic profiles in fulminant hepatic failure: relationship to outcome. *Liver Transpl* 2005;11:1353-1360.
246. Clevert DA, Stickel M, Minaifar N, Lohe F, Graeb C, Jauch KW, Reiser M. Contrast-enhanced ultrasound in liver transplant: first results and potential for complications in the postoperative period. *Clin Hemorheol Microcirc* 2009;43:83-94.
247. Ren J, Lu MD, Zheng RQ, Lu MQ, Liao M, Mao YJ, Zheng ZJ, et al. Evaluation of the microcirculatory disturbance of biliary ischemia after liver transplantation with contrast-enhanced ultrasound: preliminary experience. *Liver Transpl* 2009;15:1703-1708.
248. Chung WY, Gravante G, Al-Leswas D, Alzarraa A, Sorge R, Ong SL, Pollard C, et al. Addition of a kidney to the normothermic ex vivo perfused porcine liver model does not increase cytokine response. *J Artif Organs* 2012;15:290-294.
249. P G. Ischaemia- reperfusion injury. *British Journal of Surgery* 1994: 637-647.
250. Carden DL, and D. Neil Granger. Pathophysiology of ischaemia-reperfusion injury. *The Journal of pathology* 2000:255-266.

251. Datta G, Fuller BJ, Davidson BR. Molecular mechanisms of liver ischemia reperfusion injury: insights from transgenic knockout models. *World J Gastroenterol* 2013;19:1683-1698.
252. Peter ME, Krammer PH. Mechanisms of CD95 (APO-1/Fas)-mediated apoptosis. *Curr Opin Immunol* 1998;10:545-551.
253. Scaffidi C, Fulda S, Srinivasan A, Friesen C, Li F, Tomaselli KJ, Debatin KM, et al. Two CD95 (APO-1/Fas) signaling pathways. *EMBO J* 1998;17:1675-1687.
254. Yin XM. Bid, a critical mediator for apoptosis induced by the activation of Fas/TNF-R1 death receptors in hepatocytes. *J Mol Med (Berl)* 2000;78:203-211.
255. Cursio R. Caspase inhibition in liver transplantation: from basic research to clinical studies. *HPB (Oxford)* 2010;12:1-3.
256. Igney FH, Krammer PH. Death and anti-death: tumour resistance to apoptosis. *Nat Rev Cancer* 2002;2:277-288.
257. Elmore S. Apoptosis: a review of programmed cell death. *Toxicol Pathol* 2007;35:495-516.
258. Lowe SW, Lin AW. Apoptosis in cancer. *Carcinogenesis* 2000;21:485-495.
259. Wen J, Duan Y, Zou Y, Nie Z, Feng H, Lugnani F, Baust JG. Cryoablation induces necrosis and apoptosis in lung adenocarcinoma in mice. *Technol Cancer Res Treat* 2007;6:635-640.
260. Yang E, Korsmeyer SJ. Molecular thanatopsis: a discourse on the BCL2 family and cell death. *Blood* 1996;88:386-401.
261. Zamzami N, Brenner C, Marzo I, Susin SA, Kroemer G. Subcellular and submitochondrial mode of action of Bcl-2-like oncoproteins. *Oncogene* 1998;16:2265-2282.
262. Reed JC. Bcl-2 and the regulation of programmed cell death. *J Cell Biol* 1994;124:1-6.
263. Hockenbery DM. bcl-2 in cancer, development and apoptosis. *J Cell Sci Suppl* 1994;18:51-55.
264. Grassi A, Susca M, Ferri S, Gabusi E, D'Errico A, Farina G, Maccariello S, et al. Detection of the M30 neoepitope as a new tool to quantify liver apoptosis: timing and patterns of positivity on frozen and paraffin-embedded sections. *Am J Clin Pathol* 2004;121:211-219.
265. Topaloglu S, Abbasoglu O, Ayhan A, Sokmensuer C, Kilinc K. Antiapoptotic and protective effects of roscovitine on ischemia-reperfusion injury of the rat liver. *Liver Int* 2003;23:300-307.
266. Malhi H, Gores GJ. Cellular and molecular mechanisms of liver injury. *Gastroenterology* 2008;134:1641-1654.
267. R. MV. Ischemia/Reperfusion, Does Temperature Matter? Laboratory Perspective. *Liver Transplantation* 2015;21:S1-S5.
268. Nayak A, Raikar A, Kotrashetti V, Nayak R, Shree S, Kambali S. Histochemical detection and comparison of apoptotic cells in the gingival epithelium using hematoxylin and eosin and methyl green-pyronin: A pilot study. *J Indian Soc Periodontol* 2016;20:294-298.
269. Sun K, Liu ZS, Sun Q. Role of mitochondria in cell apoptosis during hepatic ischemia-reperfusion injury and protective effect of ischemic postconditioning. *World J Gastroenterol* 2004;10:1934-1938.
270. Tsung A, Sahai R, Tanaka H, Nakao A, Fink MP, Lotze MT, Yang H, et al. The nuclear factor HMGB1 mediates hepatic injury after murine liver ischemia-reperfusion. *J Exp Med* 2005;201:1135-1143.
271. Shining Y ea. Histopathological Evaluation of Apoptosis in Cancer. *AJP* 1998;153(4):1041-1053.

272. Maione F1 GN, Lazzaro S2,et al. . Porcine Isolated Liver Perfusion for the Study of Ischemia Reperfusion Injury: a Systematic Review. . Transplantation.
273. Lubner MG, Hinshaw JL, Andreano A, Sampson L, Lee FT, Jr., Brace CL. High-powered microwave ablation with a small-gauge, gas-cooled antenna: initial ex vivo and in vivo results. *J Vasc Interv Radiol* 2012;23:405-411.
274. Zhou W, Liang M, Pan H, Liu X, Jiang Y, Wang Y, Ling L, et al. Comparison of ablation zones among different tissues using 2450-MHz cooled-shaft microwave antenna: results in ex vivo porcine models. *PLoS One* 2013;8:e71873.
275. Awad MM, Devgan L, Kamel IR, Torbensen M, Choti MA. Microwave ablation in a hepatic porcine model: correlation of CT and histopathologic findings. *HPB (Oxford)* 2007;9:357-362.
276. Matsukawa T, Yamashita Y, Arakawa A, Nishiharu T, Urata J, Murakami R, Takahashi M, et al. Percutaneous microwave coagulation therapy in liver tumors. A 3-year experience. *Acta Radiol* 1997;38:410-415.
277. Kato T, Suto Y, Hamazoe R. Effects of microwave tissue coagulation on the livers of normal rabbits: a comparison of findings of image analysis and histopathological examination. *Br J Radiol* 1996;69:515-521.
278. Hyodoh H, Furuse M, Kawamoto C, Isoda N, Ido K, Saito K. Microwave coagulation therapy: ex vivo comparison of MR imaging and histopathology. *J Magn Reson Imaging* 2000;11:168-173.
279. Strickland AD, Clegg PJ, Cronin NJ, Swift B, Festing M, West KP, Robertson GS, et al. Experimental study of large-volume microwave ablation in the liver. *Br J Surg* 2002;89:1003-1007.
280. Shah AJ, Callaway M, Thomas MG, Finch-Jones MD. Contrast-enhanced intraoperative ultrasound improves detection of liver metastases during surgery for primary colorectal cancer. *HPB (Oxford)* 2010;12:181-187.
281. Jagad RB, Koshariya M, Kawamoto J, Papastratis P, Kefalourous H, Patris V, Porfiris T, et al. Laparoscopic microwave ablation of liver tumors: our experience. *Hepatogastroenterology* 2008;55:27-32.
282. Brace CL, Hinshaw JL, Lubner MG. Thermal ablation for the treatment of abdominal tumors. *J Vis Exp* 2011.
283. Liang P, Yu J, Lu MD, Dong BW, Yu XL, Zhou XD, Hu B, et al. Practice guidelines for ultrasound-guided percutaneous microwave ablation for hepatic malignancy. *World J Gastroenterol* 2013;19:5430-5438.
284. van Meer S, de Man RA, Siersema PD, van Erpecum KJ. Surveillance for hepatocellular carcinoma in chronic liver disease: evidence and controversies. *World J Gastroenterol* 2013;19:6744-6756.
285. Meloni MF, Goldberg SN, Livraghi T, Calliada F, Ricci P, Rossi M, Pallavicini D, et al. Hepatocellular carcinoma treated with radiofrequency ablation: comparison of pulse inversion contrast-enhanced harmonic sonography, contrast-enhanced power Doppler sonography, and helical CT. *AJR Am J Roentgenol* 2001;177:375-380.
286. Claudon M, Dietrich CF, Choi BI, Cosgrove DO, Kudo M, Nolsoe CP, Piscaglia F, et al. Guidelines and good clinical practice recommendations for Contrast Enhanced Ultrasound (CEUS) in the liver - update 2012: A WFUMB-EFSUMB initiative in cooperation with representatives of AFSUMB, AIUM, ASUM, FLAUS and ICUS. *Ultrasound Med Biol* 2013;39:187-210.
287. McCarley JR, Soulen MC. Percutaneous ablation of hepatic tumors. *Semin Intervent Radiol* 2010;27:255-260.
288. Chouker A, Lizak M, Schimel D, Helmberger T, Ward JM, Despres D, Kaufmann I, et al. Comparison of Fenestra VC Contrast-enhanced computed tomography imaging with

- gadopentetate dimeglumine and ferucarbotran magnetic resonance imaging for the in vivo evaluation of murine liver damage after ischemia and reperfusion. *Invest Radiol* 2008;43:77-91.
289. Alzaraa A, Gravante G, Chung WY, Al-Leswas D, Morgan B, Dennison A, Lloyd D. Contrast-enhanced ultrasound in the preoperative, intraoperative and postoperative assessment of liver lesions. *Hepatol Res* 2013;43:809-819.
290. Wei Z, Ye X, Yang X, Zheng A, Huang G, Li W, Ni X, et al. Microwave ablation in combination with chemotherapy for the treatment of advanced non-small cell lung cancer. *Cardiovasc Intervent Radiol* 2015;38:135-142.
291. Lee EW, Chen C, Prieto VE, Dry SM, Loh CT, Kee ST. Advanced hepatic ablation technique for creating complete cell death: irreversible electroporation. *Radiology* 2010;255:426-433.
292. Chu KF, Dupuy DE. Thermal ablation of tumours: biological mechanisms and advances in therapy. *Nat Rev Cancer* 2014;14:199-208.
293. Paulet E, Aube C, Pessaux P, Lebigot J, Lhermitte E, Oberti F, Ponthieux A, et al. Factors limiting complete tumor ablation by radiofrequency ablation. *Cardiovasc Intervent Radiol* 2008;31:107-115.
294. Kwan KG, Matsumoto ED. Radiofrequency ablation and cryoablation of renal tumours. *Curr Oncol* 2007;14:34-38.
295. Haen SP, Pereira PL, Salih HR, Rammensee HG, Gouttefangeas C. More than just tumor destruction: immunomodulation by thermal ablation of cancer. *Clin Dev Immunol* 2011;2011:160250.
296. Davalos RV, Mir IL, Rubinsky B. Tissue ablation with irreversible electroporation. *Ann Biomed Eng* 2005;33:223-231.
297. Sanchez-Ortiz RF, Tannir N, Ahrar K, Wood CG. Spontaneous regression of pulmonary metastases from renal cell carcinoma after radio frequency ablation of primary tumor: an in situ tumor vaccine? *J Urol* 2003;170:178-179.
298. Mehta A, Oklu R, Sheth RA. Thermal Ablative Therapies and Immune Checkpoint Modulation: Can Locoregional Approaches Effect a Systemic Response? *Gastroenterol Res Pract* 2016;2016:9251375.
299. Lu DS, Raman SS, Vodopich DJ, Wang M, Sayre J, Lassman C. Effect of vessel size on creation of hepatic radiofrequency lesions in pigs: assessment of the "heat sink" effect. *AJR Am J Roentgenol* 2002;178:47-51.
300. Lu DS, Raman SS, Limanond P, Aziz D, Economou J, Busuttil R, Sayre J. Influence of large peritumoral vessels on outcome of radiofrequency ablation of liver tumors. *J Vasc Interv Radiol* 2003;14:1267-1274.
301. Potten CS. What is an apoptotic index measuring? A commentary. *Br J Cancer* 1996;74:1743-1748.
302. Shinohara T, Ohshima K, Murayama H, Kikuchi M, Yamashita Y, Shirakusa T. Apoptosis and proliferation in gastric carcinoma: the association with histological type. *Histopathology* 1996;29:123-129.
303. Soini Y, Paakko P, Lehto VP. Histopathological evaluation of apoptosis in cancer. *Am J Pathol* 1998;153:1041-1053.
304. Alzaraa A MM, Zayyan K, Morgan B, West K. Enhanced role for apoptosis in a hepatic ischaemia-reperfusion injury model. *Journal of Integrative Gastroenterology and Hepatology* 2018;1:48-53.
305. Rübenthaler J PK, Hameister E, et al. Diagnostic accuracy of contrast-enhanced ultrasound (CEUS) in monitoring vascular complications in patients after liver transplantation - diagnostic performance compared with histopathological results. *Clin Hemorheol Microcirc*. 2017;66:311-316.

306. Li H, Lu J, Zhou X, Pan D, Guo D, Ling H, Yang H, et al. Quantitative Analysis of Hepatic Microcirculation in Rabbits After Liver Ischemia-Reperfusion Injury Using Contrast-Enhanced Ultrasound. *Ultrasound Med Biol* 2017;43:2469-2476.
307. Francica G M, Riccardi, de Sio, Terracciano, Caturelli, Iadevaia, Amoroso, et al. Ablation treatment of primary and secondary liver tumors under contrast-enhanced ultrasound guidance in field practice of interventional ultrasound centers. A multicenter study. *Eur J Radiol*. 2018;105:96-10.
308. WuLi-Lia C-X, LiKaia, et al. Potential application of ultrasound-guided thermal ablation in rare liver tumors. *Hepatobiliary & Pancreatic Diseases International* 2018.
309. Xu EJ1 LS, Li K1, Long YL1, Zeng QJ1, Su ZZ1, Zheng RQ1. Immediate evaluation and guidance of liver cancer thermal ablation by three-dimensional ultrasound/contrast-enhanced ultrasound fusion imaging. *Int J Hyperthermia* 2018;34:870-876.
310. Halil Mert Bahadır TS, Ömer Topuz , et al. Protective effects of quercetin on hepatic ischemia reperfusion injury. *İstanbul Med J* 2017;18.
311. Xuhua Duan PC, Xinwei Han, et al. The influence of liposomal quercetin on liver damage induced by microwave ablation. *Scientific Reports* 2017;7:16063.
312. Erik Velez SNG, Gaurav Kumar, et al. Hepatic Thermal Ablation: Effect of Device and Heating Parameters on Local Tissue Reactions and Distant Tumor Growth. *Radiology* 2016;281:782-792.

Published articles:

Ahmed Alzaraa, Fergus McKeagney, Charalampos Seretis¹, Kassim Zayyan, Kevin West, Bruno Morgan. Apoptosis Post Microwave Ablation of the Liver: Does it Change with Power?. *Clinical Journal of Surgery*. 2018; 1(1): 1-6.

Alzaraa A, Megson M, Zayyan K, Morgan B, West K. Enhanced role for apoptosis in a hepatic ischaemia-reperfusion injury model. *Journal of Integrative Gastroenterology and Hepatology*, 2018; 1(1): 48-53.

Ahmed Alzaraa, Wen Yuan Chung, Bruno Morgan, Kevin West and David Lloyd. Contrast-enhanced Ultrasound in the Assessment of the Transitional Zone of Microwave Ablations in an Ex vivo Perfused Liver Model; is It a Useful Tool?. *British Journal of Medicine & Medical Research*, 2015; 8(4): 298-312.

Alzaraa A, Al-Leswas D, Chung WY, Gravante G, Bruno M, West K, Dennison A, Lloyd D. Contrast-enhanced ultrasound detects perfusion defects in an ex vivo porcine liver model: a useful tool for the study of hepatic reperfusion. *J Artif Organ*, 2013;16(4):475-82

Alzaraa A, Gravante G, Chung WY, Al-Leswas D, Morgan B, Dennison A, Lloyd D. Contrast-enhanced ultrasound in the preoperative, intraoperative and postoperative assessment of liver lesions. *Hepatol Res*, 2013;43(8):809-19.

Alzaraa A, Gravante G, Chung WY, Al-Leswas D, Bruno M, Dennison AR, Lloyd DM. Targeted microbubbles in the experimental and clinical setting. *Am J Surg*, 2012; 204 (3):355-66.

Meetings and conferences

Presentations (oral):

A Alzaraa, *et al.*

Does contrast-enhanced ultrasound provide better assessment of microwave ablations in an ex vivo porcine liver model. *East Midlands Surgical Society meeting, 2014, Nottingham, UK.*

A Alzaraa, *et al.*

Detection of ischaemia-reperfusion injury in a porcine liver model by contrast-enhanced ultrasound. *East Midlands Surgical Society meeting, Sheffield, 2011.*

Presentations (poster):

A Alzaraa, *et al.*

Detection of ischaemia-reperfusion injury in a porcine liver model by contrast-enhanced ultrasound. *The joint international congress of ILTS, ELITA & LICAGE, 22-25/06/2011, Valencia, Spain.*

